Chapter 5
Flight Transceiver

Hamid Hemmati, Gerardo G. Ortiz, William T. Roberts,
Malcolm W. Wright, and Shinhak Lee

5.1 Optomechanical Subsystem

Hamid Hemmati

The flight transceiver's major subsystems include opto-mechanical; laser transmitter; and acquisition, tracking and pointing. Flight qualification is a major aspect of a flight transceiver. Subchapters 5.1 through 5.4 provide a description of each of these areas.

5.1.1 Introduction

The flight transceiver terminal optical train is typically comprised of an afocal fore-optics accommodating transmit, receive, align (calibration), and beacon reference channels for acquisition, tracking and pointing. The optical system assembly typically consists of a front aperture, reflection or refraction type telescope, with or without a solar rejection filter, aft optics (including lenses, mirrors, beam-splitters, and filters), fine-pointing mirror(s), and array detector(s) (quadrant or larger area array). The optical system assembly also includes the mechanical support to provide a rigid, low-thermal-expansion structure for the optical system, baffling to reject stray light, and a thermal control assembly to control the temperature of the laser head module.

Figure 5-1 details the optical approach for the system that the Jet Propulsion Laboratory (JPL) has developed for communications to planets within our Solar System. This system is more complex than communication systems for Earth orbit due to requirements for better isolation of transmit and

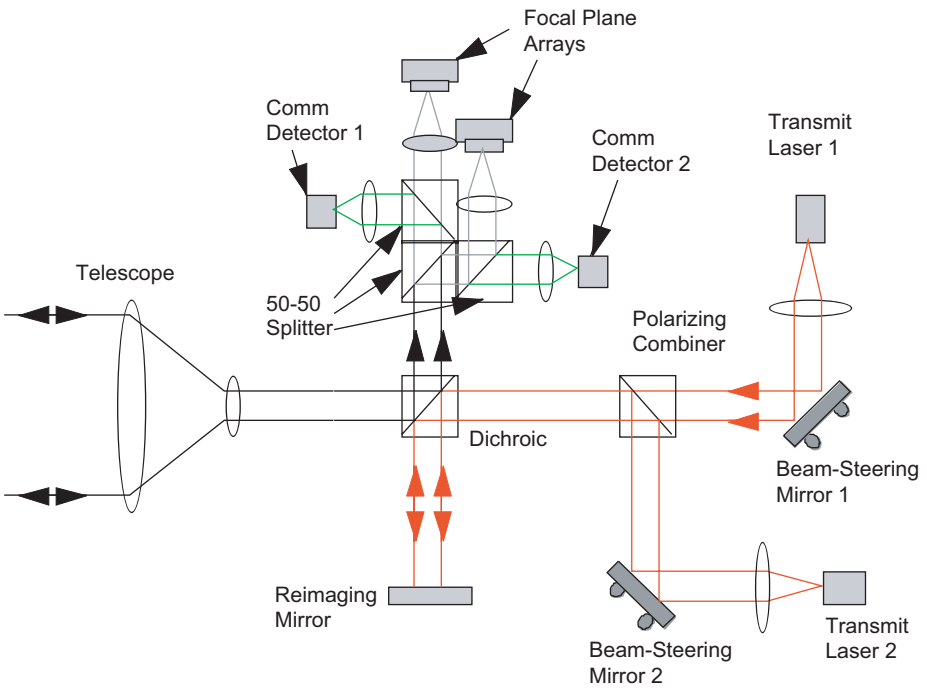

Fig. 5-1. Block diagram of the optical communications transceiver, including redundant channels.

receive channels; stringent demands on acquisition, tracking and pointing (imposed by the greater communication range); and the need to attenuate a larger amount of out-of-field radiation [1]. The out-of-field radiation is due primarily to operating conditions that periodically require the Sun to be near the field of view (within as little as 1 deg).

5.1.2 Optical Beam Paths

In addition to transmitting the optical data, the optical system receives the beacon signal, which is used for acquisition and tracking and to uplink command data from Earth or from another spacecraft. The beacon signal has a narrow spectral band, such as a laser signal from a cooperative target. Pointing may also be assisted by offset from wider band references, such as celestial reference signals from stars or from the Sun-illuminated Earth or Moon.

The transmit and receive channels may consist of separate or common apertures. Use of a single aperture, for both transmit and receive, minimizes coordinate transfer errors between the tracking and the transmit channels. It also minimizes size. In this case though, transmit and receive isolation may become challenging.

Fig. 5-2. A picture of JPL's Optical Communication Demonstrator optical assembly.

Figure 5-2 illustrates the Optical Communication Demonstrator (OCD) developed at JPL [2,3]. This optical system includes four channels and utilizes a single aperture for both transmitting and receiving signals. The telescope is a two-mirror system in a Cassegrain configuration. The telescope and the aft optics can be designed to provide a high degree of stray-light rejection. This may be achieved by the incorporation of field stop(s) and a Lyot stop(s). The field stop is located at the focus of the two-mirror telescope and limits out-of-field scattering into the rest of the optical system. The Lyot stop is located at a conjugate pupil plane near the imager lenses at a location behind the insertion point for the transmit laser. The Lyot stop eliminates diffracted spider and aperture radiation at the focal plane from bright out-of-field sources like the Sun. The location of the Lyot stop assures that it will not be backside-illuminated by the transmit laser.

Utilization of separate focal planes for the celestial and the transmit reference channel may be necessary. This is driven by a large difference in signal level between the two channels. Optimization through use of different sensor types for each channel may also be accomplished with this approach [4].

The transmit channel consists of an optical path extending from the output of the laser transmitter to the exit aperture of the optics. A design-driving requirement may be inclusion of a fine-pointing mirror at the rear pupil. The fine-pointing mirror module controls the downlink over the entire system field-of-view while maintaining good beam quality. A high wavefront quality on the order of 0.025 wave root mean square (RMS) or better is desired for this channel. The transmit optics in front of the laser are essentially a laser beam expander that matches the diameter of the laser beam to the rest of the optical train.

The receive channel's function is to accept light emerging from the fore-optics, and direct it to a circular detector. It is a light-collecting channel; therefore, a high wavefront quality is not important for the receive path as long

as there is not excessive spillover beyond the edges of the detector. In principle, the receiver could be either an imager or a pupil relay. Receiver photodetectors having small (<0.5 mm) active diameters pose many challenges for an efficient design that concentrates all received light onto the detector without overfilling it. As will be discussed later in this chapter an effectively larger active diameter may be formed by adding an immersed lens or a compound parabolic concentrator (CPC) to the photodetector. Narrow-band filtering is typically utilized in front of the concentrator to reduce the incident background radiation. This channel is expected to provide the field-of-view (FOV) required to cover the spacecraft deadband motion cycle. Also, it should provide the degree of optical isolation required to sufficiently minimize the effect of signal feedback from the transmit path.

The acquisition and tracking channel images part of the transmit laser signal onto a reference detector array. In the design of the OCD, the image formed by this optical path is purposely blurred while maintaining uniformity across the field. The receive optics may spread the tracking signal over two to three pixels. A good approach for blurring is to control the beam size with optics as opposed to introducing aberrations. However, the image must be void of coma and other non-symmetric aberration patterns. For OCD, a single array detector is used to receive both the beacon as well as the transmit reference signals. The instantaneous position of the downlink signal is measured in this channel. Over the large interplanetary distances expected, and particularly when Earth-image tracking is required, the dynamic range of the tracking signal can vary by 2 to 3 orders of magnitude. Readout of the beacon image position on the focal-plane-array detector relative to the reference location provided by the transmit signal and center of the array detector, provides the information for the fine pointing mirror to accurately point the transmit laser at the position of the beacon (e.g., the ground station). Due to the cross velocity between the spacecraft and the ground station, the transmit signal must be pointed ahead of (or behind) the apparent position of the ground station.

The reference (or align) channel is basically a simple lens that forms an image of a portion of the transmit light at the array detector without any high degree of image quality. Again, the image is purposely blurred to facilitate centroiding functions.

5.1.3 Optical Design Requirements, Design Drivers, and Challenges

The optical system typically consists of multiple channels including: (1) transmit channel accommodating a two-axis fine-pointing mirror and possibly a dedicated point-ahead mirror; (2) receive channel; (3) acquisition and tracking channel; (4) tracking reference channel, and (5) calibration channel. Some of the design drivers and design practices include:

Afocal fore-optics: A collimated beam behind the telescope provides design simplifications, for example, when accommodating a fine-pointing mirror within the terminal. Typically, for flight qualification reliability and onboard calibration difficulty reasons, a focusing mechanism for the telescope is not incorporated.

Short focal length primary mirror: The requirement for short telescope length limits the F/number of the telescope primary mirror to about F/1.0. A large secondary magnification is required to provide an adequately long overall focal length for the required FOV and spot size at the acquisition detector. This large magnification results in significant field curvature, which must be corrected by the auxiliary optics.

Field of view: The field-of-view (FOV) requirement of a fraction of a degree is relatively large for two-mirror telescope optical systems. Residual aberrations are curvature of field and off-axis astigmatism, which must be corrected by the auxiliary refractive optics. This makes the auxiliary optical design more complicated. The communication and acquisition FOVs are typically different, for example, 1 mrad (0.06 deg) for communications, and ±5 mrad for acquisition. Coincidence between the transmit laser and beacon beam within the communications FOV must be held to very tight tolerances.

Stability requirements: The optical system must provide, at all times, an adequate level of pointing stability between the transmit and the receive channels. The required stability is typically much less than 0.1 mrad. The distance between the telescope primary and secondary (or tertiary mirror, if applicable) should be held to very tight tolerances (typically on the order of a few microns) over lifetime of the mission.

Well-baffled telescope: Spurious (stray light) signals can cause significant radiometric and thermal problems for the laser communication terminal. Therefore, stray light rays that get past the baffles to anywhere inside the field-stop must be blocked off before they can go through the telescope aft optics. Typically, referenced to the internal telescope pupil, the maximum solar stray-light levels should be held to less than 1 μW/nm-sr.

Field-stop: A field-stop can effectively block the light from bright objects (like the Sun) near the edge of the FOV in the telescope. Due to diffuse scattering from the telescope mirror surfaces, ideally only a maximum of two mirror surfaces are allocated before the field stop. This means that astigmatism and field curvature will not be corrected in the telescope and must instead be corrected by the auxiliary optics.

Lyot stop: The Lyot stop can largely eliminate diffracted energy from bright out-of-field objects. The Lyot stop is designed so that no baffle, spider vane, or optical element edges ahead of the telescope focal plane can be seen at any of the detectors. The Lyot stop is a conjugate near-field point image of the entrance aperture of the optical system. Two conjugate intermediate images are required. One is at the fine-pointing mirror to assure that there will be no beam

walk at the primary mirror when the fine-pointing mirror is moved for fast pointing purposes. The other near field image is selectively masked with a Lyot stop at some point in the optical system so that it blocks out-of-field radiation that is diffracted into the FOV by the edges of the two telescope mirrors, the baffles, the spider vanes, etc. Providing a second near-field point for a Lyot stop will add size and mass due to the need for additional imaging and collimating optical elements.

Polarization state: For direct detection, polarization state of the beam typically is not of concern unless the design requires it. However, for coherent transmission systems, a well-defined polarization state (linear and circular) is a prerequisite.

Spectral band-pass: When a broad spectral band (non-laser) source beacon is used, it is often difficult to accommodate both the beacon and the transmit wavelengths without significant use of reflective optics. All-refractive designs are generally much more difficult to produce while maintaining a small transceiver volume.

Multiple redundant optical channels: Multiple and redundant optical channels may be formed using refractive optics (Fig. 5-1). However, beam-spread away from an intermediate point due to the FOV drives the size of these optical elements up. The larger acquisition FOV, along with the numerous beam-splitters required, makes the auxiliary optical path length long, increasing the overall volume.

Radiation environment: For certain missions, such as Jupiter and its moons, the radiation environments become a design consideration. This is an issue primarily for the refractive optics and some of the dielectric coatings within the system. Currently, only about a dozen radiation-hard optical glasses with suitable characteristics are commercially available.

5.1.4 Optical Design Drivers and Approaches

The optical design is driven by a need to minimize size and mass of the optical system. Reflective type telescopes provide the best performance versus size and mass for spacecraft use when the telescope aperture is greater than about 7-cm in diameter. Catadioptric, obscured reflective, unobscured reflective configurations, and variations of the Cassegrain telescope design, such as Richey-Chretien (RC), offer good matches to optical communication requirements. Off-axis telescopes are free of a secondary mirror obscuration at the cost of higher alignment tolerance. Off-axis telescopes are larger than on-axis designs of the same aperture. For RC-based or other on-axis Cassegrain transceivers, volume can be reduced and baffling of the telescope optics can be simpler than for most off-axis designs. Restriction on the overall size of the transceiver results in requirements for a relatively fast primary mirror for the telescope. Length of the acquisition and tracking receive channel optical system

can be kept short by using a secondary mirror having a relatively high telephoto ratio of about five to one. Use of all-spherical optics results in lower manufacturing cost compared to the hyperbolic primary and secondary mirrors of an RC telescope, but additional optics are needed to correct spherical aberrations.

An afocal characteristic (i.e., formation of a pupil behind the telescope) is desirable when a fine pointing mirror or Lyot stop is used. Fore-optic configurations with an afocal characteristic include: catadioptric, obscured reflective, unobscured reflective, and slightly off-axis reflective. For larger FOVs (on the order of 20 mrad), a two-mirror afocal system lacks the degrees of freedom to produce diffraction-limited wavefront error over the entire field at a convenient exit pupil location. Additional complexity (i.e., either a third mirror or a refractive collimating group) is needed. A Cassegrain-type design produces negative Petzval curvature (inward curving field). A concave mirror behind the Cassegrain focus can collimate the light. Its Petzval curvature is convex toward the collimator so it can match the Cassegrain Petzval. This is the on-axis version of the configuration which, when used in an unobscured manner is called the Three-mirror Anastigmat (TMA). The TMA and the above three-mirror Cassegrain, match most of the requirements set for the fore-optics. A partially (bent) off-axis primary mirror design in a three-mirror telescope may allow use of spherical mirrors. Folding of the optical path behind the telescope poses its own challenges. The requirements are minimal obscuration and the need to get the components out of each other's path. Good solutions that meet the requirements are available [3,4]. The lowest overall obscuration that can be achieved is on the order of 10 to 15 percent of the diameter.

5.1.5 Transmit–Receive–Isolation

Isolation is required to prevent system failure. The transmit powers are typically ten orders of magnitude larger than the receiver sensitivity levels. For a given transceiver that must point near the Sun, as much as 150 dB isolation of the receive channel from the transmit channel may be required. Specular backscatter from flat transmitting surfaces that are normal to the incident beam could cause actual ghost images of the transmit laser that are concentrated over just a few pixels of the detector array. Tilting of the flat transmitting surfaces alleviates the possibility of ghost images falling inside the detector array field-of-view. Backscattered energy from curved surfaces is often much fainter and less defined. Some of most likely sources of unwanted radiation falling on the various focal planes, and methods to mitigate them are as follows:

1) Scattered sunlight from optical surfaces due to surface roughness and contamination. This effect may be minimized by keeping the optical surfaces as clean as possible and by making them very smooth (on the order of 1 nm RMS) and relatively free of flaws. It is reasonable to expect that

the total integrated scatter due to surface roughness and contamination at each surface is 3×10^{-4} or less. This topic is described in more detail in later in this chapter under Stray Light Control (5.1.6).

2) Diffracted and scattered sunlight from mechanical surfaces such as baffles, aperture edges, and spider vanes. Some may include high order diffraction. Proper baffle design along with a field-stop and Lyot-stop will minimize these effects. The Lyot stop and the field-stop together will assure that no radiation from outside the FOV can be imaged or diffracted into the FOV of any detectors.

Different isolation schemes that can be implemented include:

Spatial isolation uses separate transmit and receive apertures to keep the outgoing transmit beam from back scattering off of common optical elements. This technique is only used for short range links with large beam divergences, which can allow for large transmit-to-receive beam misalignments associated with separate transmit and receive optical systems.

Spectral isolation uses separate transmit and receive wavelengths to isolate transmit and receive beams. This method allows common use of optical elements in the system (including the same aperture), and it can achieve isolation greater than 120 dB. Spectral isolation is applicable to long-range links where narrow beams and co-alignment are required.

Temporal isolation in which the receiver is effectively turned off to eliminate the chance of interference. Temporal isolation can only be used in systems where the data rates are favorable for these timing constraints. Temporal isolation is used in long-range links that require narrow beams and co-alignment, but where only a single wavelength is available.

Polarization isolation in which the transmit light and the receive light are linearly polarized, and then circularized (right hand or left hand) in different polarizations for isolation. This is accomplished with polarization-sensitive optical elements, and is good to about 6 to 8 orders of magnitude.

Aperture sharing in which the optical paths share the same aperture, but do not go through the same exact path. This scheme often requires larger diameter optics than what would otherwise be needed.

Coding utilizes codes with extreme depth of interleave.

Combined isolation where greater degree of isolation is achieved by combining any of the above techniques.

It is expected that the above approaches will result in less than 1×10^{-15} of the incident stray radiation on the telescope falling on any single detector pixel. This is an adequate level of isolation, and for a given optical system it needs to be verified by stray light analysis and actual scatter measurements.

Chopping of the beacon laser light used for acquisition and tracking (e.g. on the order of 5 to 10 kHz, followed by lock-in detection) is an effective means of isolating the incoming beacon light.

5.1.6 Stray-Light Control

Any undesired light reaching the focal spot or a focal plane of the transceiver constitutes stray light. Some of the pathways through which spurious photons may arrive at the focal spot include: scattering from mirror imperfections, contaminants and baffles, or diffraction from contaminants or edges of the secondary mirror obstruction and its supporting structure. Scattering from optical surfaces, a major contributor to stray light, has a strong wavelength dependence that varies as $1/\lambda^4$ [5,6,7,8]. When the transceiver communicates with Earth, the Sun is the primary contributor to stray light since it is one billion times brighter than the Sun-illuminated Earth. Therefore, even a miniscule fraction of the sunlight scattered from the front aperture optomechanical elements will amount to a significant scattered light level at the focus. At the small (<2 deg) Sun-Probe-Earth (SPE) angles typically encountered in deep-space missions, the spacecraft's tracking and pointing focal plane will see increased background noise. This can lead to an increase in pointing error and can cause difficulty in detecting the Earth image or uplink beacon signal. Thus, the required Sun angle has a major effect on the amount of stray light that may be expected within the terminal. Therefore, a design having adequate levels of stray-light rejection is essential to improve the tracking performance at low SPE angle. Here, we concentrate our discussion mainly on the primary mirror since it will likely be the dominating factor in the overall stray-light performance of most deep-space flight terminal optical systems.

The scattering probability density (that is, the probability that a photon with a given direction of polarization incident on a surface at a certain wavelength will be scattered into a particular direction and with a particular polarization) is related to bi-directional reflectance distribution function (BRDF). BRDF is the fraction of power scattered per unit solid angle and has units of sr^{-1} (1/steradian). BRDF may be predicted analytically by modeling of a given optical surface topology and represents the average scattering from the entire surface area. The integral of BRDF overall scattering angles is hemispherical reflectance. Clearly, low BRDF values are desired. Major contributors to BRDF are surface roughness, particulates, and reflective coatings materials and processes.

5.1.6.1 Operation at Small Sun Angles. In a mission to Mars, for example, it is periodically required that the flight terminal operate with the Sun near the FOV. At these times, the Sun-Probe (spacecraft)-Earth (SPE) angles are small ($\leq$2 deg). Under these conditions, it is crucial to prevent the sunlight from entering the telescope. Several preventive schemes are available. These include: (1) windows at the entrance aperture of the telescope and (2) narrow-bandpass filter with effective filtering of the out-of-band wavelengths. Baffles external to the telescope, such as a honeycomb shape structure whose internal surfaces are

coated with a highly absorbing black material do not work as well as expected. In the case of laser beacon tracking, the transmit and receive wavelengths are close to each other. Therefore, it is possible to use a narrow-bandpass filter as the front window of the telescope. In the case of star tracking with broadband wavelengths, the star-trackers utilize separate optical systems that are not co-aligned with the laser-communication transceiver. Therefore it is feasible to utilize a narrow-band filter, centered at the transmit laser wavelength, in conjunction with the flight telescope.

For stray light rejection, several telescope designs (e.g., a Gregorian telescope, with a Lyot stop) offer viable solutions. Given a well-defined set of optical and optomechanical designs, commercial software programs (such as ASAP, TRACEPRO, ZEMAX and GUERAP) can provide an estimate of the stray light magnitude (good to a factor of 2–10). A more precise estimate of the system performance requires laboratory measurements.

5.1.6.2 Surface Cleanliness Requirements. Contamination of an optical surface, by the particulates in the environment, greatly enhances surface scattering. Contamination may be avoided by special handling of the transceiver during integration, assembly with the spacecraft, and at launch [9]. A Class-100 clean room should be adequate for this purpose. Federal and military standards for surface cleanliness are defined in Federal Standard document 209D and 1246B, respectively [10,11]. With distribution and using the Mie scattering theory, one can determine the BRDF associated with a certain level of surface cleanliness level as defined in Military Standard 1246B. Surface contamination, in contrast with surface scattering, has very little wavelength dependence.

The statistical distribution of the size of dust particles in a clean room is reported in Federal Standard 209D. Using this distribution and the Mie scattering theory, it is possible to state the BRDF that would arise from a certain surface cleanliness level as defined in Military Standard 1246B [11]. Very low BRDF values can, in principal, be achieved if the surface is sufficiently clean. However, in any realistic environment, the surface cleanliness level will be an increasing function of time as the surface accumulates more particulate matter from the atmosphere. It is possible to relate, at least on an order-of-magnitude scale, the surface cleanliness level to the amount of time the surface spends in a clean room of a given class.

5.1.7 Transmission, Alignment, and Wavefront Quality Budgets

Any given design is optimized for maximum transmission through the telescope and to each of the focal planes. The design needs to be toleranced for decentering and misalignment of the secondary or tertiary mirrors relative to the primary mirror. These mirrors may be placed on a slow, thermally focusable

mount that once in a while focuses or otherwise adjusts the telescope in flight to remove significant misalignment error. The telescope wavefront quality affects the Strehl ratio that directly influences the telescope's antenna gain value.

5.1.8 Efficient Coupling of Lasers to Obscured Telescopes

A strong peak in the middle of the Gaussian distribution characterizes lasers with TEM_{00} spatial output beam quality. A TEM_{00} mode beam is typically used for free-space optical communications. Reflecting telescopes with on-axis secondary mirrors that obscure the primary mirror are also commonly used in laser-communication system. Significant central vignetting loss of the laser beam, as much as 50 percent or more may occur. For example, making certain assumptions for the optical system, a secondary mirror and baffle blocking of approximately 8.4 percent of the beam area, result in nearly 30 percent loss of the laser energy. While, an obscuration on the order of 25 percent may result in nearly 65 percent loss of the laser energy. Several different schemes have been devised for efficient coupling of lasers to obscured telescopes and are described below briefly [12]

5.1.8.1 Axicon Optical Element. Axicons are both afocal refractive and reflective optical elements with a flat front surface and conical rear surface, and can turn the incident beam inside out. The rays near the edge of the beam entering the axicon get located at the inside edge of the annular beam when exiting. Likewise, the rays at the center of the incident beam get located around the edge of the annular beam when exiting. The axicon must be designed specifically to match the resulting donut-shaped intensity re-distribution across the beam to that of the telescope obscuration, to avoid the coupling losses. Use of axicons for efficient coupling to telescopes was analyzed and experimentally evaluated in detail [13,14]. Difficulties in fabrication of the precise conical axicon devices, and the tight alignment requirements have so far limited the usefulness of these devices. Axicon insertion losses in reflectance and transmittance can be kept small by the proper choice of coatings. The far field pattern is Gaussian in appearance with normal diffraction point spread function (PSF). Diffraction rings can be observed, but are mostly suppressed.

5.1.8.2 Sub-Aperture Illumination. In this scheme, the transmit beam is coupled to the telescope for sub-aperture illumination, missing, and offset at the secondary mirror. This is the simplest arrangement that can be used to avoid the secondary mirror obstruction. In this approach, the far-field pattern is the same as the source. Divergence of the transmitted beam would be greater than if we were to use the full aperture.

5.1.8.3 Prism Beam Slicer. A prism device with afocal refractive and reflective optical elements behaves similarly to axicons. The difference between the axicon and the prism slicer is the use of multiple flat surfaces for the rear side of the slicer. Prism beam slicers, in effect, slice the incident beam into two or more pie-shaped beams that are then arranged in a circular pattern around the telescope aperture (Figs. 5-3 and 5-4). Each beam is sub-aperture in size and can pass through the Cassegrain telescope without any additional vignetting from the telescope secondary mirror and baffle. Because each beam is pie shaped, the far-field pattern for a single beam is not symmetrical (Fig. 5-5). However, the combined far-field pattern for the four beams will be nearly symmetrical.

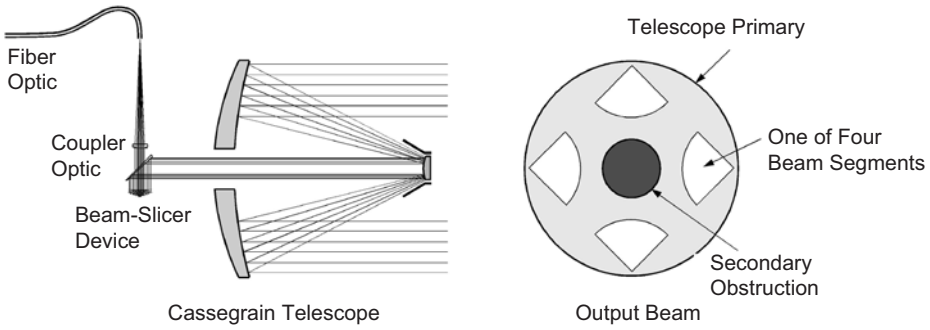

Fig. 5-3. Layout of the beam-splitter device.

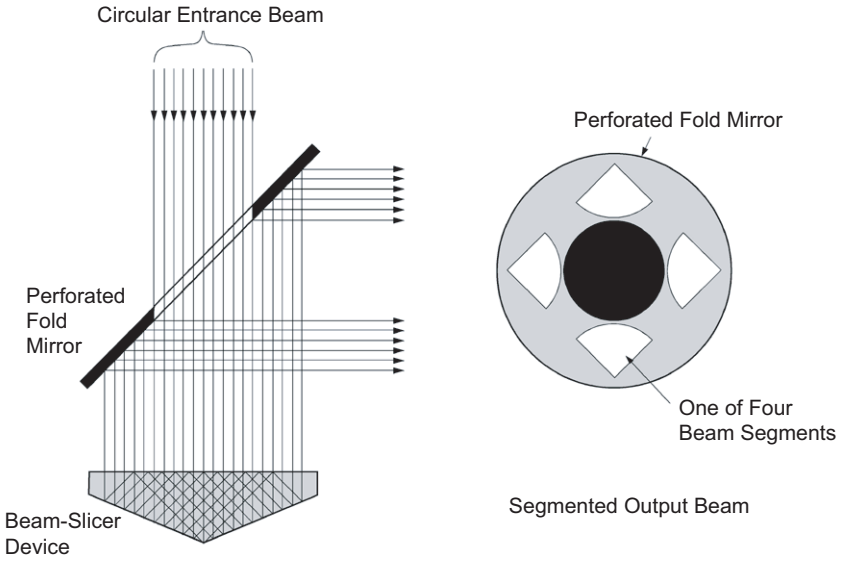

Fig. 5-4. Details of the prism beam-slicer function.

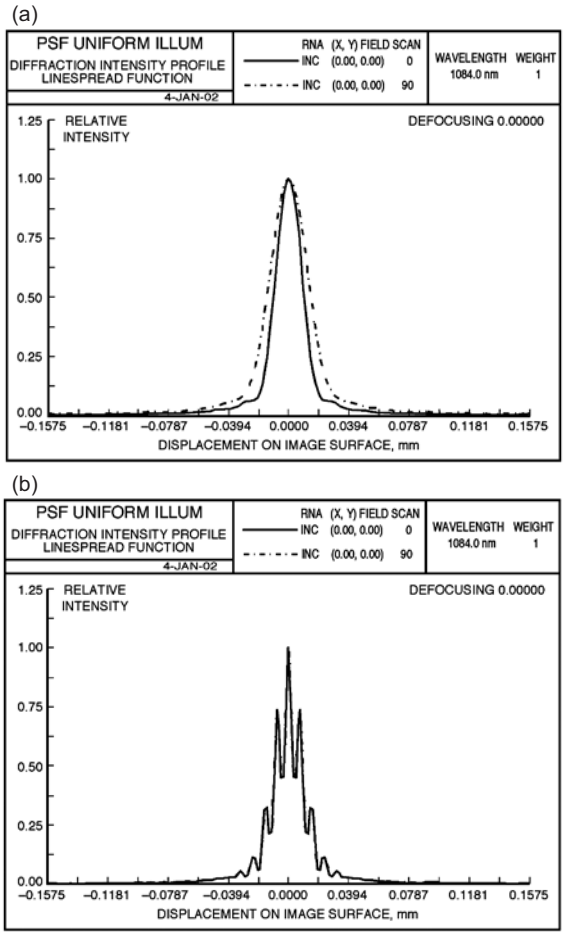

Fig. 5-5. Far-field pattern (a) for a single prism slicer beam and (b) for four prism slicer beams that are phased.

5.1.8.4 Beam Splitter/Combiner. The beam splitter/combiner is a variation of the sub-aperture approach, and one of its applications is beam combining. This configuration produces multiple beams equally spaced in a circle at the telescope aperture. The far-field pattern for each beam is the same as the source. When the multiple beams are combined in the far field, the beam pattern is the same as one of the sources. Because the source for each beam is a separate laser source, each beam is incoherent with the other beams. This approach also offers some degree of redundancy.

5.1.9 Structure, Materials, and Structural Analysis

On average, in an optical communication terminal, the optical bench and the structure that supports the optical components, together account for 25 to 50 percent of the total mass of the terminal. Minimizing this will clearly reduce the overall mass. The requirements for a generic optical communication telescope material are mirror surface figure of better than 1/12 of a wave (peak-to-peak), minimum weight, low scatter surface, high thermal stability, high fundamental resonance frequency, and ease of fabrication (low material fabrication cost). It is crucial to prevent any temperature gradients across the bench that holds the optics. A critical high structural stability requirement is that of the primary mirror and secondary (or even tertiary) mirror separation under temperature variations. It is possible to incorporate a slow (thermal) one-axis (piston for focus) or multi-dimensional actuator with the secondary or tertiary mirrors to actively align the telescope in flight.

Ultra-low expansion (ULE), titanium silicate glass, and Zerodur glass ceramic have excellent thermal properties, but they are heavy. Zerodur substrates with hollowed regions have been developed, but the cost is high. Silicon carbide (SiC) and SiC matrixes (e.g., standard metal oxide (SXA)) and some other composite materials to one degree or other satisfy all of the above requirements. Beryllium (Be) is a very lightweight telescope material, with a density that is comparable to aluminum, but with significantly higher thermal coefficient of expansion than the materials mentioned earlier. Be satisfies most of the above requirements, but it is difficult and expensive to fabricate due to the material safety hazards. Also, Be mirrors are not stable over temperature cycles. Primary and secondary mirrors made of this material should be of very high temperature stability and very high tolerance to ionizing radiation.

SiC is one of the best telescope (structure, primary and secondary mirrors) materials. Some of the outstanding features of SiC use in space are: (1) high specific stiffness and low mass; (2) very low thermal expansion coefficient (on the order of 1 part per million per kelvin (ppm/K)); (3) high thermal conductivity; (4) very high bending strength (400 megapascals (MPa)) and low built-in stress (<0.1 MPa); (5) capability for withstanding low and high temperatures without any loss of properties; (6) high resistance to fatigue; (7) very high immunity to radiation; and (8) it can be ground and polished without significant distortions. However, the surface quality achievable with large (>30 cm) primary mirrors is not yet ideal. Except for very low mass, current technologies are developed enough to satisfy the above requirements. Material characteristics of foremost importance to a laser communication terminal include the following.

Optical performance: Ease of fabricating a high quality surface figure in a spherical or aspheric shape and coating for high reflectance and low scattering and with lowest number of defects is of prime interest.

Structural integrity: Fundamental resonance frequency, dynamic response, specific stiffness, and fracture threshold are major characteristics that affect the structural integrity of the material. Most of these properties influence the terminal's weight [15]. For example, a certain weight is required to achieve a particular natural frequency or dynamic response to maintain integrity over a particular vibration frequency. The greater the specific stiffness for a material, the lower its weight is.

Thermal stability: Both soaked (e.g., relatively small gradient) and gradient temperature variations may be encountered. The main concern is temperature gradients that might change the surface figure of the optical system. Of major interest is avoiding a mismatch between the thermal expansion of the optics and the structure supporting the optics. For example, metering rods with a specific thermal coefficient of expansion are used to connect the secondary mirror to the primary mirror of the telescope in order to offset any bi-metallic bending effects that may arise. SiC is one of the most thermally stable materials, and it may be used for both optics and optical structure (Fig. 5-6).

Temporal stability: Inherent dimensional stability and micro-yield strength are major constituents of this property. Due to the temporal nature of this property, it is one of the more difficult parameters of a material to measure. In general, a material with low rate of creep and relaxation is desired.

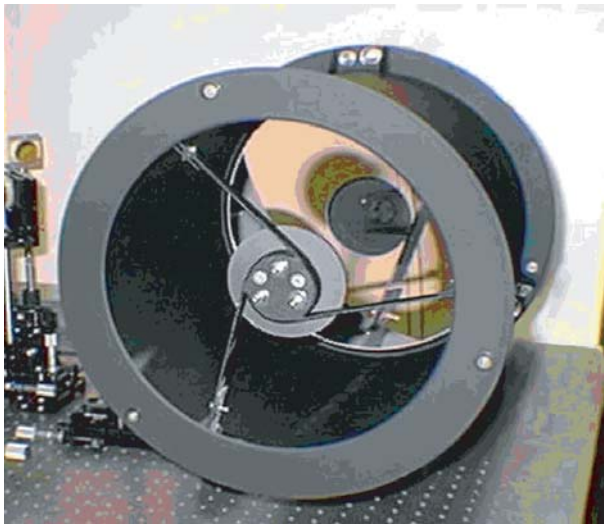

Fig. 5-6. An all (mirrors and structure) silicon carbide telescope with a 30-cm spherical mirror diameter built by SSG Inc. This telescope showed good performance over a ±50 deg C temperature range. This telescope weighs about 6 kg. A 4-kg version is feasible with additional work.

Packaging: To minimize the overall size of the transceiver, the aft-optics path may be folded such that the sensors and the laser head are mounted in one or (at the most) two planes behind the telescope. The telescope and optical structure material need to have very low thermal expansion, high thermal conductivity, and low weight [16,17,18]. Due to the thermal management difficulties and the heat generated by the laser, it is prudent to separate the laser from the optical head (telescope and aft optics) assembly. Fiber-optic-fed lasers work the best; however, with high peak power pulsed lasers, it is not always possible to use fiber optics.

5.1.10 Use of Fiber Optics

Free-space optical communication systems can greatly benefit from the wealth of development in fiber-optics technology [19] Use of fiber optics in the laser communication system can afford multiple degrees of freedom while reducing mechanical stability requirements, easing thermal management requirements, and potentially reducing system mass and volume. Fiber-optic systems may be applied to both non-coherent and coherent systems with polarized or unpolarized beams. In the transmitter subsystem, with the aid of fiber optics, the heat-generating laser transmitter may be located remotely from the heat-sensitive optical system. High-power continuous-wave lasers and pulsed-laser transmitters up to peak power levels that are below the nonlinear or damage threshold to the fiber may be applied. The received signal may also be coupled into a fiber or a fiber bundle to a remotely located senor. Conical scanning of the fiber's signal input end is another means of maximizing signal delivery and at the same time inferring tracking information.

5.1.11 Star-Tracker Optics for Acquisition and Tracking

With laser beacon tracking where the beacon emanates from the Earth, or with Earth-image tracking, stray light and Sun-interference becomes a major challenge at small Sun-probe-Earth angles. This is a particularly difficult challenge at outer-planetary ranges. For example at Pluto, the Earth and the Sun are always within a 2-deg cone angle. Precision star tracking is a viable alternative to Earth-emanated beacons, since stars of interest are far from the Sun. Addition of one to two precision star-trackers looking at orthogonal or at 180-deg angles relative to the optical axis of the flight terminal, may provide a beaconless alternative freeing the terminal from full-time availability of sufficiently strong signal from Earth and from the small Sun-angle. These star trackers need to be an integral part of the optical system and have built-in sensors such that any drift between the optical systems will be known and can be accounted for. This may be achieved by bringing a very low-power probe laser onto the star-tracker imager. This laser is completely collinear with respect to the transmit laser, and thus the situation is functionally as if the

transmit laser light were placed onto the star tracker. The dedicated star trackers will have a smaller aperture than the optical communication terminal (about one third or less), but with much higher FOV (on the order of degrees). In this case, the star-trackers may be used as the spacecraft star trackers as well, in order to reduce mass and power consumption. The star tracker may also be designed as part of the laser flight optical-communications terminal, where the front telescope design accounts for the required star-tracker FOV. As an example, Fig. 5-7 shows a backward-looking star tracker along with drift-detection sensors implemented with the flight transceiver.

Figure 5-8 shows the schematic of a catadioptric star-tracker optical system designed for inclusion with the optical communications terminal.

5.1.12 Thermal Management

On a deep-space mission, temperature external to the insulation that covers the transceiver might vary between 50 deg C to –200 deg C. Therefore, a controlled heater will be required for the terminal to control the optical assembly to, for example, ±5 deg C since optical systems may be designed to be athermal over this (soaked) temperature change. The temperature of the electronics box is typically maintained to within 10 ±40 deg C. To dissipate the heat generated by the laser transmitter and electronics, a dedicated radiator or the spacecraft radiator may be used. Dedicated radiators are more efficient and more convenient to implement. These radiators do not have to be accurately controlled in temperature. Some of the active elements within the terminal, for example the laser oscillator in an oscillator/amplifier or the pump diode lasers for a diode-pumped solid-state laser (doped crystal or doped fiber) may need precise temperature control.

5.1.13 Optical System Design Example

Table 5-1 outlines the specifications for an example design of an optical communication system with 10-cm front aperture diameter with the capability for precision pointing.

5.1.13.1 Afocal Fore-Optics. For the specified field of view, a two-mirror afocal telescope lacks the degrees of freedom to produce diffraction-limited wavefront error and a convenient exit pupil location. Either a third mirror or a refractive collimating group, is needed. A three-mirror Cassegrain provides good wavefront, intermediate image for stray anastigmat. In this case, the RMS wavefront error was calculated less than 0.001 waves at a 600-nm wavelength.

5.1.13.2 Receiver Channel. The function of the receiver is to accept light emerging from the fore-optics and direct it to a circular detector. It is a light-

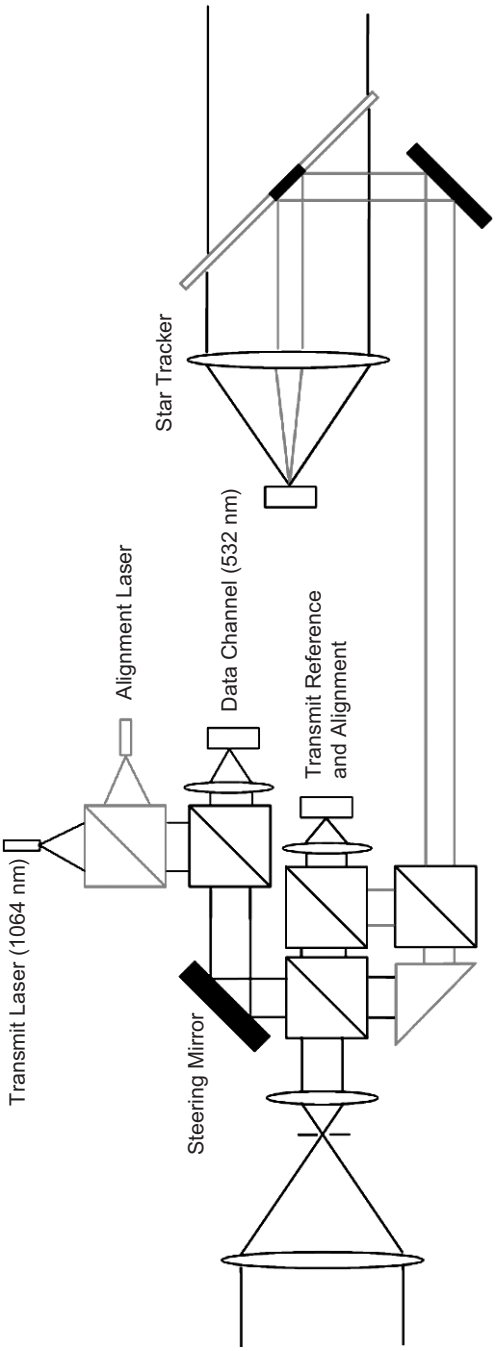

Fig. 5-7. Block diagram of the optical communication terminal, including a dedicated star tracker and a redundant transmit subsystem.

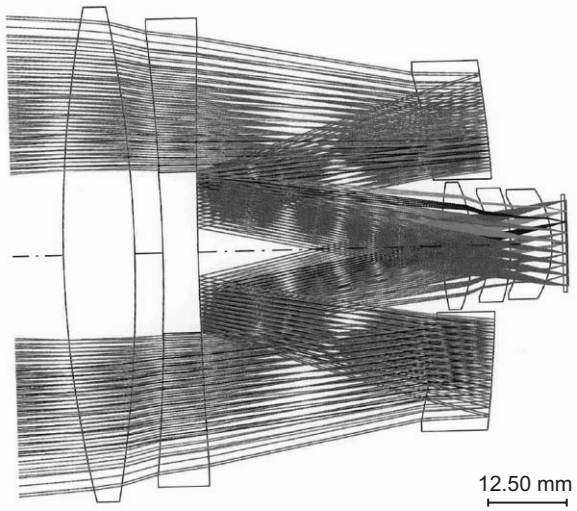

Fig. 5-8. The designed catadioptric star-tracker optical system.

collecting channel, and image quality is not important as long as there is not excessive spillover beyond the edges of the detector.

The receiver could be either an imager or a pupil relay. A pupil relay is preferred due to the need for inclusion of the scan mirror. The Lagrange invariant severely limits the achievable spot size at the focus. An alternative is to relax the specification on detector diameter to a larger value, e.g., 1.0 mm. To illustrate the difficulty of a design in air, Fig. 5-9 shows a receiver with a 0.5-mm detector in air. Due to high ray angles, the field coverage in the sky is only 8×8 mrad, versus 10×10 mrad, which is the goal. Pupil aberrations cause the beam footprint from off-axis field angles to overfill the circular detector (Fig. 5-10(a)). A higher-performance design uses an immersed detector, in contact with the final, plano-convex element. In that case, the beam prints across the field to fill the detector with little (a few percent) mismatch (Fig. 5-10(b)). To enhance collection efficiency with a pupil relay receiver channel, one may either use an immersion lens with a 0.5-mm diameter detector, or use a lens in air with a larger detector diameter, such as 1 mm.

It is possible to collect the light from the afocal section and concentrate it onto the detector using a compound parabolic concentrator (CPC). A CPC may be of a solid catadioptric design or be a hollow reflector. Each would provide different properties. Index matching cement between the CPC and the detector will be required to obtain the desired performance. For a solid catadioptric CPC, its length gets progressively shorter as the refractive index increases. However, it is useful to note that the semi-diagonal field leaving the afocal

Table 5-1. Requirements, specifications, and goals for a preliminary optical design of a laser communication transceiver.

Parameter	Requirements, Specifications, and Goals
Configuration	Space-qualified laser communication transceiver. Common afocal plus four channels: Transmit 1064 nm, receive 532 nm, alignment laser 980 nm (transmit), and stellar reference 550–900 nm (receive). Scan mirror for pointing transmitted laser beams. Minimal size, mass, and power.
General system specifications	
Entrance pupil diameter	100 mm
Vignetting (of area), maximum	
Secondary obscuration	10 percent
Off axis	10 percent
Thermal environment	
Operating	20 ±10 deg C
Survival	–40 to +45 deg C
Instrument package envelope	<5 × 5 × 6 in. (13 × 13 × 15 cm)
Size and mass	Minimize
Lyot stop	
In system	Required in transmit and align channels
Location	Near scan mirror before align/transmit optics
Radiation-hard glasses	Not needed
Scan mirror	
Function	Scan align and transmit lasers over the FOV in sky in reduced-beam space inside align/transmit channels
Location	
Scan range (in sky)	±5 mrad
Clear aperture	15 × 22 mm elliptical
Accessible internal focus	Needed for all channels
Cemented refractive elements	Avoid
Afocal fore-optics	
Purpose	Perform beam diameter reduction
Configuration	3-mirror centrally obscured; re-imaging to control pupil
Aperture stop	On secondary to minimize obscuration
Field of view in sky	±5 mrad (±0.29 deg)
Afocal magnification	Implied by scan mirror size specifications
Wavefront quality	Maximize (waves RMS, 600 nm)
Transmit channel	
Purpose	Expand and collimate laser beam
Transmit laser	
Profile	Gaussian TEM_{00}
Diameter	0.6 ±0.1 mm ($1/e^2$ assumed)
Divergence	1.5 ±0.3 mrad (reference)
Strehl ratio	0.90–0.91
Wavelength	1064 nm
Clear aperture over sizing	$2 \times 1/e^2$
Field of view	On axis

Table 5-1. Requirements, specifications, and goals for a preliminary optical design of a laser communication transceiver. (cont'd)

Parameter	Requirements, Specifications, and Goals
Diameter of beam emerging from transmit channel, before afocal fore-optics	15-mm ($2 \times 1/e^2$ diameter)
Focal length of transmit optics	afocal
Transmit optics Strehl ratio	≥0.95
Receive channel	
Function	Receives monochromatic radiation & relays pupil onto detector
Wavelength	532 nm
Receive channel FOV, total	10 × 10 mrad in sky
Detector	Single detector, ≥0.5 mm diameter
Image quality	Image the pupil onto the detector, with <5 percent area overfilling
Stellar reference channel	
Purpose	Receive and focus broad band radiation
Wavelength	Different star temperatures and uniform CCD response assumed
Focal length of stellar reference channel	Assumed this refers to full channel including afocal fore-optics
F-number	Derivable from 100-mm input beam diameter and 800-mm focal length
Detector	1024 × 1024 × 12 × μm Note, active image area is 8 × 8 mm, per specifications on effective focal length and sky FOV
Field of view in sky, total	10 × 10 mrad
Image quality	PSF spread over 30 μm to facilitate centroiding
Image centroid shift between stars at 2800 & 10,000 K	<±0.1 pixel (±1.2 μm) need <±0.02 pixel (±0.6 μm) goal
Telecentricity error	Up to 1.1 deg
Centroid shift with stellar temperature (10,000, 5800, & 2800 K).	Centroid shift with respect to 600-nm chief ray: 0.78 μm (2800 K) quantum efficiency (Q.E.) 0.61 μm (5800 K) Q.E
Alignment channel	
Purpose	Transmits laser beam
Wavelength	980 nm
Laser Type Waist, divergence	 Diode laser Model as point source, F/5 emerging from fiber
Field of view	On axis
Focal length of alignment channel	500 mm, derivable from F/5 and 100-mm entrance pupil diameter
Wavefront quality	Purposely blurred (e.g., spherical aberration), 0.14 waves RMS (42 μm 80 percent encircled energy diameter)

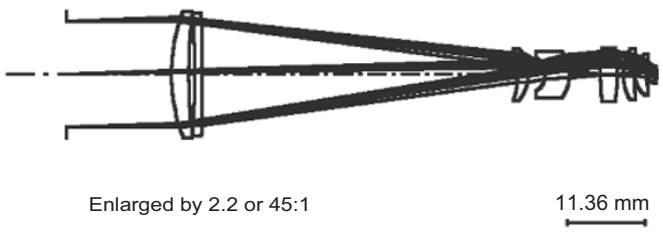

Fig. 5-9. Receiver with a 0.5-mm diameter detector in air (non-immersed).

fore-optics has a semi-diameter of 7.5 mm and a semi-diagonal field of view of 2.73 deg. The Brightness Theorem of radiative transfer demands that the quantity $n^2 dA \mathrm{Sin}^2\theta$ be conserved throughout the system. In this equation, n is the index of refraction, dA is an infinitesimal element of area along a light beam, and $\mathrm{Sin}^2\theta$ is related to the solid angle. The square root of this expression may be regarded as a generalization of the Lagrange invariant, the requirement for brightness to be conserved throughout the system. Measured at the exit pupil of the fore-optics, this quantity has a value of 0.357 mm. Since the detector has a semi-diameter of 0.25 mm and the maximum value of $\mathrm{Sin}\theta$ unity, it follows that a concentrator must have an index of at lease 0.357/0.250 = 1.43 in order to concentrate all the light from the exit pupil to the detector. The CPC gets progressively shorter as the refractive index increases. However, since it must also be cemented to the detector with index matching cement, lets limit ourselves to $n = 1.6$. The CPC disadvantages (1.8 times longer than the immersed pupil relay and is more difficult to fabricate) probably outweigh the advantages of athermal, alignment-free design. Figure 5-11(a) shows a solid glass CPC operating over the conditions described above, and Fig. 5-11(b) shows the associated footprint data. Use of the pupil imager with an immersed receiver will probably result in the most compact configuration.

5.1.13.3 Stellar Reference Channel. The stellar reference channel forms an image that is purposely blurred but uniform across the field. The 80-percent encircled energy diameters of the stellar reference optics alone (not including the afocal fore-optics) range from 28–30 μm.

5.1.13.4 Align and Transmit Channels. The optical elements of the alignment and receiver channels are common up to a beamsplitter. A design-driving requirement is that these channels must contain a scan mirror located at a pupil. In the concept discussed here, the pupil formed by the three-mirror afocal fore-optics is relayed to a remote location by a refractive 1 afocal relay (Fig. 5-12). The beam feeds both the alignment and receiver channels.

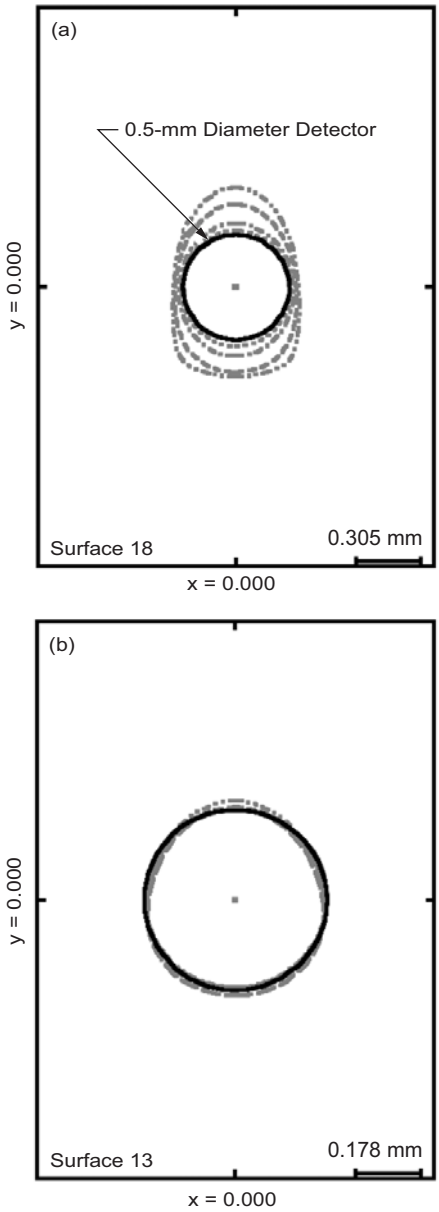

Fig. 5-10. Overfill of detector aperture due to off-axes field angles: (a) assuming a detector in air and (b) corrected for by use of an immersed detector.

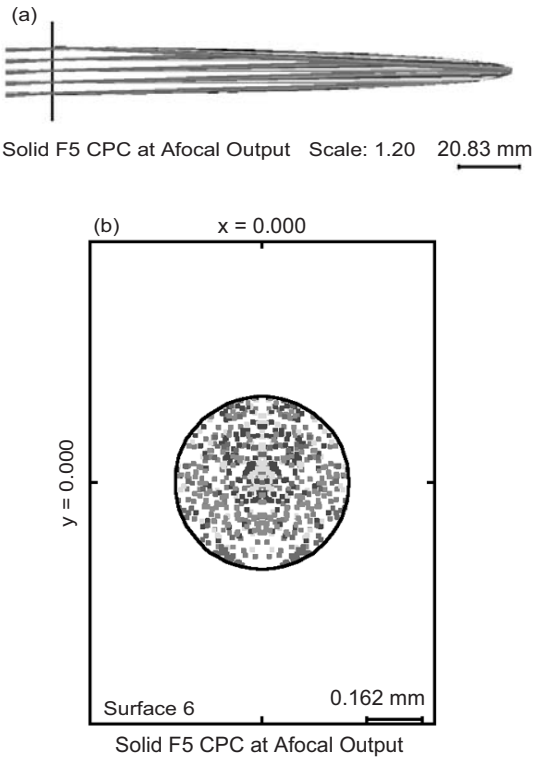

Fig. 5-11. The CPC: (a) a solid-glass CPC and (b) its associated beam footprint.

The transmit optics are essentially a laser beam expander, bringing a 1.2-mm laser beam (0.6 mm $1/e^2$ diameter with 2× over sizing) to the 15-mm expanded beam diameter. A three-element configuration achieves the beam expansion with sub-0.001 wave RMS wavefront error.

The align channel is a simple lens (e.g., singlet) that forms an image at a detector without a high degree of image quality, as per the specification. The image is purposely blurred with spherical aberration to facilitate centroiding. The design has an 80-percent encircled energy diameter of approximately 47 μm. The bending of the lens can be adjusted to create the desired level of spherical aberration. As mentioned earlier, another key section in these two channels is an afocal relay, to relay the exit pupil of the reflective fore-optics to the scan mirror location. The design shown below is a 1× relay, relaying one 15-mm diameter pupil to the other with about 0.025 waves RMS wavefront error at either 980 nm or 1064 nm (separately focused).

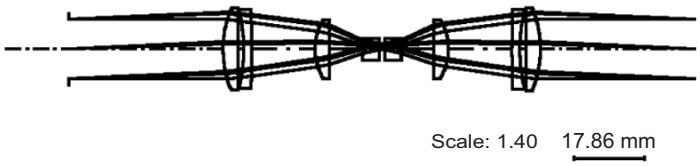

Fig. 5-12. A refractive 1x afocal relay design.

5.1.13.5 Folded Layouts. The system's optical path must be folded to minimize the envelope diameter and length (Fig. 5-13). There are different options for folding, and what is discussed is a plausible arrangement, but other arrangements could be also used. To fold the aft optics and to put the exit pupil in an accessible location, several fold methods may be applied, including, fold mirror at the Cassegrain focus, or a fold in collimated space. In principle, both of these fold concepts could have the same obscuration produced by the fold mirror or the opening in the fold mirror, i.e., about 12 percent in area. The first concept would need a way of holding the small fold mirror (e.g., by a mounting bar that would introduce as much as 15-percent additional obscuration, depending on the width of the mounting bars). The second concept is preferable in that there is better access to the internal focus for a field stop.

Figure 5-14 is a three-dimensional view of the folded aft optics. The goal is to fold the optics into one or at most two planes behind or around the primary mirror.

5.1.13.6 Tolerance Sensitivity Analysis. Tolerance sensitivity analysis must be performed on the high-performance imaging channels, namely the afocal fore-optics, the stellar reference channel, and the transmit optics. Sensitivity analysis is done with a basic defocus compensator, and in some cases with an additional compensator that counteracts asymmetric aberrations. In all cases, the performance criterion is RMS wavefront error. The following design improvements may be implemented: (1) perform tolerance analysis using more specific performance parameters as the criterion (e.g., diffracted 80-percent encircled energy diameter for the stellar reference channel) to achieve higher Strehl ration; (2) adjust the tolerances to produce a higher Strehl ratio; and (3) simulate the beneficial effects of re-spacing the elements using measured data for radius, thickness, and refractive index. This is a simple operation that can make a meaningful improvement to the as-built system performance. Table 5-2 summarizes the tolerance levels used in the sensitivity analysis.

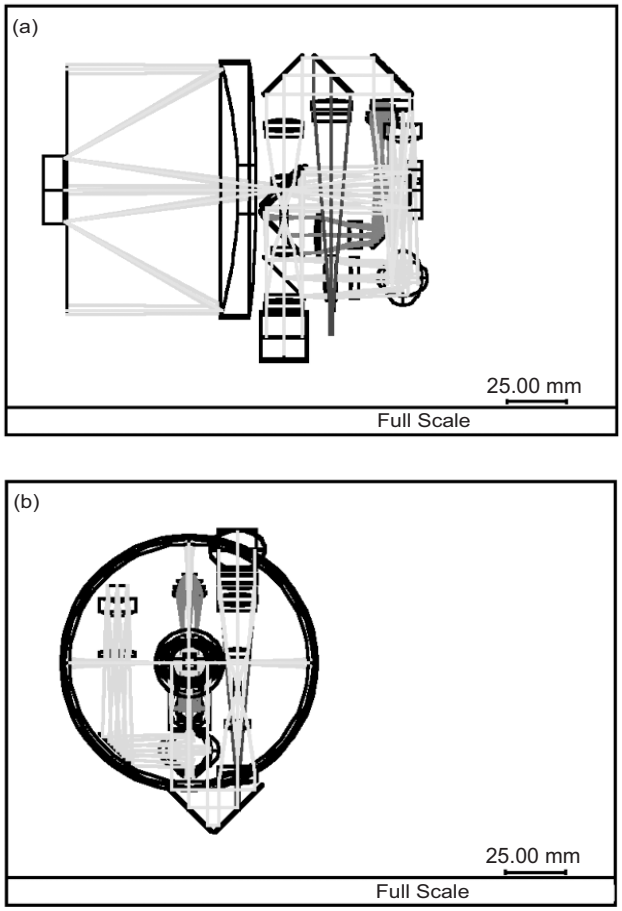

Fig. 5-13. Views of folded channels for an afocal design: (a) side view and (b) end view.

5.1.13.6.1 Afocal Fore-Optics. For the selected set of tolerance levels, the most sensitive tolerances in the fore-optics are the surface figure of the mirrors, and the tilt and decentration of the primary and secondary mirrors. A focus compensator is needed; axial adjustment of the secondary and tertiary give equivalent levels of focus compensation. De-centration of the secondary mirror is an effective compensator for asymmetric aberrations caused by mirror tilts and decentrations. Decentration of the tertiary is much less effective. The as-built RMS wavefront-error (WFE) is about 0.10 waves at 600 nm (a Strehl ratio 0.67 at 600 nm or 0.87 at 1000 nm) with the secondary decentration compensator, and 0.31 waves without it.

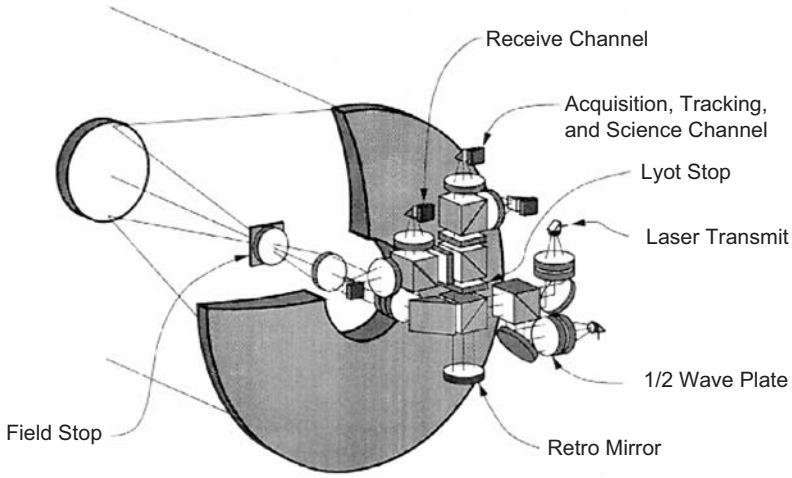

Fig. 5-14. Three-dimensional view of folded aft optics.

Table 5-2. Summary of the tolerance levels used in the sensitivity analysis.

Parameter	Tolerance value (±)
Radius	0.5 percent of design radius
Power/irregularity	1.0 / 0.25 fringe
Thickness or airspace	0.025 mm
Refractive index	0.001
Element wedge TIR*	0.01 mm
Element tilt	0.0003 radian
Element de-centration	0.025 mm

*Total internal reflection

5.1.13.6.2 Stellar Reference. The tolerance sensitivity analysis for the stellar reference channel is done with the aspheric phase plate in place, to enable us to quantify the as-built difference from ideal performance. The as-built RMS WFE is in the 0.06–0.08 range. A focus shift of the detector was assumed for the focus compensator. Performance limiting tolerances are irregularity, radius, and element wedge. Measuring each radius and re-spacing the fabricated design can reduce the effects of radius error.

5.1.13.6.3 Transmit Optics. With set of tolerance levels listed above, the as-built RMS WFE is about 0.025 waves. The focus compensator was the airspace between the front and rear groups. The surface irregularity tolerances limit the performance.

5.1.13.6.4 1× Afocal Relay. The as-built RMS wavefront error with the above tolerance set ranges from 0.09 to 0.17 waves across the field. This assumes that the final doublet will be axially adjusted to maintain best focus. Adding a decenter compensator only modestly improves performance to the 0.09 to 0.14 range. The performance is limited by radius errors, element decentrations, and element wedges. Of all the optical subsystems in the overall system, this is one of the inherently most sensitive elements because of the amount of 'work' being done in a relatively short path. Lengthening the path would likely reduce sensitivity, at the expense of a larger envelope. It is possible to lower the as-built wavefront error by desensitizing the afocal relay to tolerances, as well as simulating the effects of performing a re-space using measured data.

5.1.13.7 Thermal Soak Sensitivity Analysis. A thermal soak sensitivity analysis is made for the same three high-performance sections as for the tolerance sensitivity analysis, namely, the afocal fore-optics, stellar reference, transmit optics, and the 1× afocal pupil relay between the fore-optics and the transmit optics. The thermal soak was +10 deg C, relative to the design temperature of 20 deg C.

5.1.13.7.1 Afocal Fore-Optics. The afocal fore-optics section is potentially highly sensitive to the thermal soak. The performance is driven by the spacer material coefficient of thermal expansion (CTE). The substrate material is assumed to be fused silica (CTE 5.2×10^{-7}); not surprisingly, best performance is when the spacer CTE (invar nickel-iron alloy) nearly matches the substrate CTE, making the system nearly athermal, as if the entire assembly was made out of the same material. The trends of RMS WFE for different spacer and substrate assumptions are shown in Table 5-3.

We make the assumption of fused silica substrate because the wavelength, as low as 500 nm, may require grind-and-polish fabrication. However, if diamond turning can be done, then both the substrates and spacers can be aluminum, and the fore-optics will be athermal up to the homogeneity of the temperature and CTE within the parts.

5.1.13.7.2 Stellar Reference Channel. The stellar reference optics undergoes negligible focus shift for a 10-deg C thermal soak (i.e., 4 μm, well within its quarter-wave depth of focus).

5.1.13.7.3 Transmit Channel. The transmit optics (three-element beam expander) is more sensitive to a 10-deg C thermal soak. The performance is driven by the expansion coefficient of the material maintaining the 75-mm distance between front and rear groups. Table 5-4 shows the RMS WFE at elevated temperatures for different assumptions on the CTE of the spacer. It may also be possible to use a dual-metal spacer to passively athermalize the channel.

5.1.13.7.4 Afocal Relay. The afocal pupil relay optics, which relays the exit pupil of the fore-optics onto the entrance pupil of the transmit optics, was separately given a thermal soak analysis. Assuming aluminum spacers, the RMS WFE at elevated temperature is 0.13 waves, up from about 0.02 for the nominal design, averaged across the field. This is driven by the expansion coefficient of the spacer materials, as seen by Table 5-5.

5.1.13.8 Solid Model of System. Figures 5-15 and 5-16 show solid model renderings of the system, as constructed in LightTools. The first figure shows a side view of the full system. The different channels are color-coded and are labeled. The details of the fold arrangement in which an alignment beam is fed into the star tracker can be refined if needed.

Table 5-3. Trends of RMS WFE for different spacer and substrate assumptions.

CTE of Spacer Material	RMS WFE, Waves at 600 nm for ΔT = 10 deg C (not refocused)
236×10^{-7} (aluminum)	1.12
99×10^{-7} (stainless steel 416)	0.45
5.6×10^{-7} (invar 35)	0.002

Table 5-4. RMS WFE at elevated temperatures for different assumptions of the CTE of the spacer.

CTE of Material for 75-mm Airspace	RMS WFE, Waves at 1064 nm for ΔT = 10 deg C (not refocused)
236×10^{-7} (aluminum)	0.025
99×10^{-7} (stainless steel 416)	0.015
5.6×10^{-7} (invar 35)	0.008

Table 5-5. RMS WFE as a function of the spacer material used.

CTE of Material for Spacers	RMS WFE, Waves at 1064 nm for ΔT = 10 deg C (not refocused), Average Across Field
236×10^{-7} (aluminum)	0.128
99×10^{-7} (stainless steel 416)	0.076
5.6×10^{-7} (invar 35)	0.042

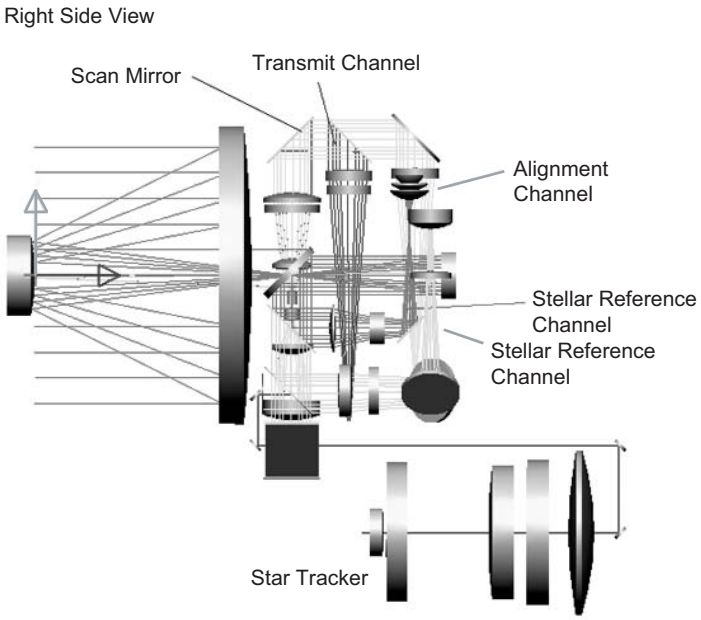

Fig. 5-15. A top view perspective of the layout.

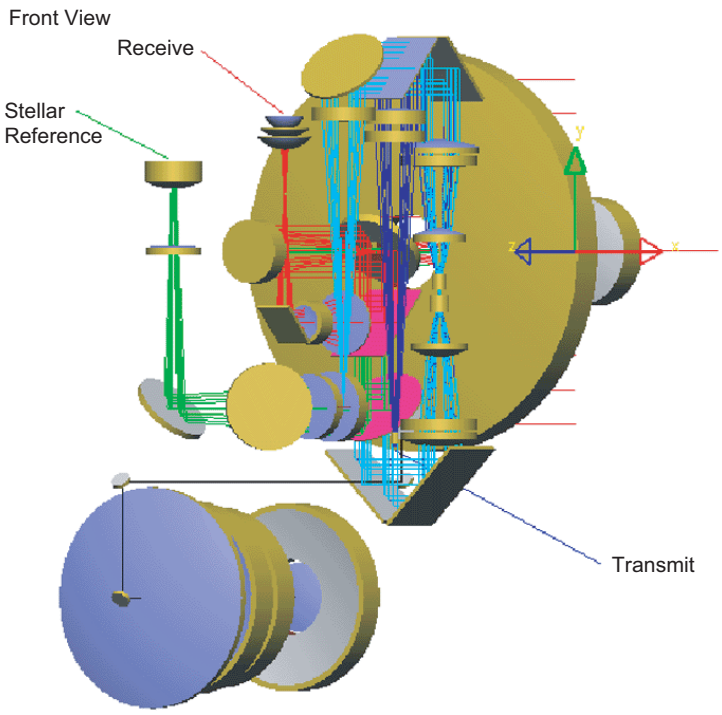

Fig. 5-16. Another perspective view shows the transmit laser, the receive channel detector, and the stellar reference channel detector.

5.2. Laser Transmitter

Hamid Hemmati

5.2.1. Introduction

Modulated laser beams carry the information that is transmitted from the laser-communication terminal. Generally, amplitude modulation is implemented for direct-detection, while amplitude or phase modulation is used for coherent communications. Applicability to onboard spacecraft use necessitates a compact, lightweight, and efficient laser transmitter. The large distances over which to communicate require a laser that is capable of high peak powers in a single-spatial mode beam. Sources for direct and coherent detection vary significantly and are discussed separately.

For deep-space direct-detection communications, pulsed lasers need to provide multiple watts of average power as well as kilowatts of peak power in sub-microsecond timeframes. Modulated continues wave (CW) lasers are inherently average power sources only and are more suited to the closer

distances of near-Earth environments. A modulation technique known as the pulse position modulation (PPM) enhances the signal-to-noise ratio (SNR) at the receiver. The benefits and details of PPM are described in Chapter 4 on Modulation Techniques. The PPM technique requires narrow pulses of moderately high (a few kilowatts) peak power that can be produced with varying repetition rates from the laser. Table 5-6 summarizes relevant parameters for a downlink from Mars for differing PPM orders. Assumptions are: range of 2.7 astronomical units (AU); data rate of 10 Mbps, a 5-m diameter ground receiver; a 30-cm diameter flight transmitter aperture with secondary obscuration, day-time reception (Sun angle of 3 deg); high quantum efficiency (≥35 percent) photon-counting indium gallium arsenide phosphite (InGaAsP) avalanche photo-diode (APD) for 1550-nm reception and silicon (Si) APD for 1064-nm reception; 0.1-MHz noise for InGaAs and 10-MHz noise for InGaAs detector; 2 dB of pointing budget allocation; 2 dB of atmospheric losses; 30 dB of transmitter modulation extinction ratio; and equivalent transmitter and receiver losses for both wavelengths.

Table 5-6 shows that pulsed lasers with moderate average power and high peak power are significantly more efficient for deep-space missions. Due to lack of peak power, the PPM alphabet implementation is limited to a maximum of about M = 4 for modulated CW sources. A well-behaved pulsed laser with adequate average power, or a low power oscillator amplified to the required power levels can satisfy laser power requirements, as shown in this table. Examples of such oscillators are semiconductor laser pumped solid-state lasers that are pulsed through several well-developed schemes (e.g., Q-switching and cavity-dumping), or pulsed oscillators amplified in a waveguide (fiber or bulk crystal). On the contrary, for near-Earth applications (spacecraft in low Earth Orbit [LEO], medium Earth orbit [MEO], or geosynchronous Earth orbit [GEO]) where just average power and significantly higher data-rates (on the order of Gbps) are required, modulated CW sources are the laser transmitter of choice.

Table 5-6. Comparison of the required input DC powers to obtain a 10-Mbps link for various laser modulation choices.

Link Characteristics	Parameter Set 1	Parameter Set 2
PPM format	4	256
Link margin (dB)	3	3
Channel capacity (Mb/s)	10	10
Required laser power (W)	70	10
Required electrical power for the laser* (W)	466.7	66.7

*assuming 15 percent overall efficiency

5.2.2 Requirements and Challenges

Some of the driving requirements for a given laser transmitter include average output power in conjunction with peak power per pulse, output beam quality, pulse-repetition-frequency (PRF), pulse-width and pulse generation time delay, pulse jitter, beam-pointing accuracy, overall efficiency, pulse extinction ratio, mass, volume, effect of ionizing radiation, thermal management requirements, and lifetime of active components. Descriptions of the critical parameters influencing the selection and design of the laser as well as some of the salient features of laser transmitters for space follow.

Pulse-repetition-frequency (PRF): The selected laser pulsing mechanism (e.g., Q-switching, cavity-dumping, or amplitude modulation of a seed laser followed by amplification) determines the laser's PRF. Q-switched lasers utilizing acousto-optic or electro-optic modulators are limited in PRF to less than 200 kHz. Cavity-dumped lasers are limited to PRFs on the order of tens of megahertz. Master-oscillator, power amplified lasers that start with a low power pulsed oscillator and are followed by several stages of amplification can potentially lead to repetition rates on the order of tens of gigahertz. In this case, the oscillator may be a diode laser that is either directly modulated or operated with an external modulator. The amplifier needs to have adequate saturated gain to sustain the repetition rate in conjunction with the hundreds to thousands of watts of peak power desired for deep-space communications. Figure 5-17 shows the behavior of laser's critical parameters as a function of the PRF.

Average output power: The laser should provide sufficient average power and the corresponding peak power to support a communication link with a sufficiently positive margin. For most telecommunication applications within the Solar System, today's diode-pumped solid-state lasers can provide power levels that are about an order of magnitude higher than those typically required. However, a communication transmitter also requires the ability to handle variable data-rates, provide nearly constant average power over different data-rates, and provide overall pulse-to-pulse power stability [20]. Reference [20] describes pulse widths, energies, and build-up time as a function of the initial inversion ratio. Efficient and short-pulse lasers operate with an inversion ratio of about 3 to 4 times threshold.

Peak power: Peak power is driven by energy per pulse and pulse-width. The PPM order utilized in the link and the required link margin that is based on a given bit error rate (BER) determine the required peak power. Solid-state lasers have demonstrated peak powers greater than 1 MW at low repetition rate but are generally limited to less than 100 kW at multi-kilohertz repetition rates. However, for a typical deep-space terminal, the anticipated maximum peak power is expected to be on the order of a few kilowatts due to spacecraft power limitations and heat dissipation issues. Fiber amplifiers have shown the capability to handle multi-kilowatt peak power in narrow (1-ns level) pulses.

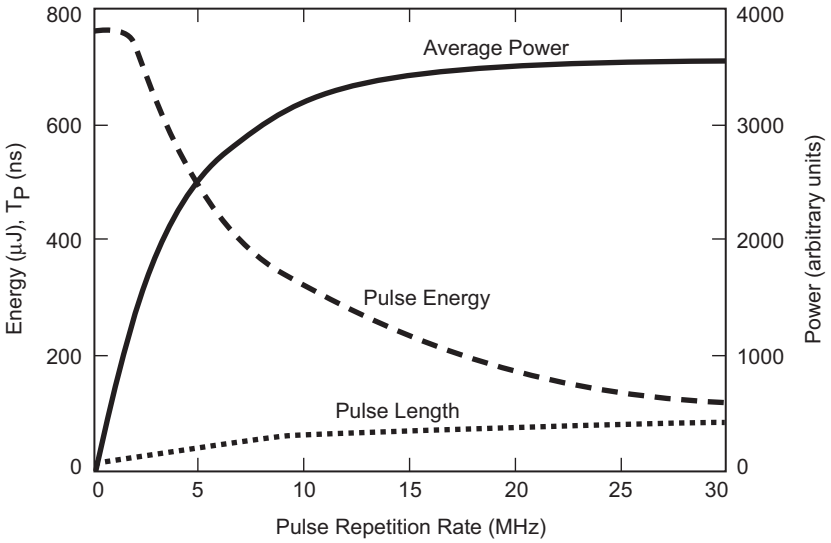

Fig. 5-17. A representative example of laser average output and peak power, and pulse width as a function of pulse-repetition frequency.

Pulse-width: Shorter pulse widths over the entire PRF range are desired since less background light is integrated in a narrow temporal slot. In optical communication systems that use the PPM scheme, the timing of the pulse carries the data in contrast to an on-off keyed modulation scheme used in near-Earth links where the pulse threshold is the determinant. The communication bit rate (R_b) is related to the PPM order (M) and the slot width (T_s) as: $R_b = (\log_2 M)/MT_s$. Therefore, the required pulse-width of the laser is inversely proportional to the magnitude of the PPM order. For example M = 8 may require a laser with a 2-ns pulse-width, while M = 256 requires only a 0.2-ns pulse width. Each of the above requirements dictates a specific type of laser that may employ a very different architecture relative to other lasers. A pulsed laser amplifier may be suitable for the low-order PPM in the above example. Whereas, a pulsed bulk crystal laser or amplified laser may be needed to satisfy the high order PPM requirements.

Pulse generation time delay: PPM requires accurate positioning of the pulses in the time domain. Laser pulse jitter results in positioning errors or the need to increase the temporal detection slot width to compensate for the jitter. In the latter case, more background light will be integrated during the increased slot width, raising the detector noise threshold at the receiver. Thus, to establish a low bit error rate communication link, the timing delay between the pulse trigger and the actual laser pulse emission must be nearly constant for all pulses. To avoid detection losses and to minimize the probability of error, the

laser transmitter's pulse jitter should be minimized to a fraction of the slot detection width. Otherwise, the effective pulse-width (temporal slot-width) becomes large, and pulse position uncertainties rise. Pulse jitter may be caused by three kinds of delays: electrical, switching, and/or build-up. Different schemes have been devised to mitigate pulse jitter effects.

Pulse extinction ratio: This is the ratio of the laser power in the on-mode to that of the off-mode. Laser emission, if not shut off completely, degrades the modulation extinction ratio, and this results in lower link margin. Solid-state lasers may have a modulation extinction ratio of 10^{-4} or better, while some directly modulated semiconductor lasers may have a relatively poor modulation extinction ratio of about 10^{-1}. Fiber lasers and amplifiers generally have an extinction ratio on the order of 10^{-3}, but, along with direct diode lasers, they are susceptible to amplified spontaneous emission if the amplifier gain is not completely saturated.

Output beam quality: To effectively transmit the beam from a spacecraft terminal with minimal losses, the laser's output beam should contain a single spatial mode or at least have no null in the center of the far-field pattern. Beams of high spatial quality may be generated through proper laser-resonator design through the use of single-mode fibers. A critical measurable parameter in this regard is the M^2 factor where an $M^2 = 1$ corresponds to a diffraction limited beam shape. An M^2 of 1.2 or lower will minimize transmission and coupling losses to an acceptable level and is generally achievable at the required output power levels. Depending on the optical design, beam ellipticity or divergence may be of concern as well. Feedback isolation of the laser from back-reflected beams is also required to avoid undesired oscillations either within the laser itself or the transmitter optical train.

Beam-pointing stability: Any given laser is subject to angular and positional uncertainties (jitter) in beam pointing stability. Resonator's spatial mode hopping and mechanical, thermal, or electro-optic effects within the laser may all contribute to jitter. Depending on the deep-space mission, in particular the spacecraft range and platform stability, the transmit laser beam will have to be pointed at the receiver with an accuracy on the order of one micro-radian or better. This requirement necessitates that pointing stability of the laser itself be maintained to a tolerance that is better than the pointing requirements for the mission. Judicious optomechanical and laser-resonator design should result in meeting these requirements. Fiber coupling the laser or using a single-mode fiber laser not only improves the beam quality but also allows more stable beam pointing by eliminating higher order modes.

Overall efficiency: The highest possible overall efficiency is desired to minimize the electrical power demand from the spacecraft. Power consumption drivers are the pump diode lasers, the thermal management of the diode lasers, and the pulsing mechanism. Improving laser efficiency poses many challenges. In pulsed lasers, laser emission efficiency is dominated by the product of

stimulated emission cross section and laser upper-state lifetime. As discussed later in this chapter, quantum defect mode matching, scatter, and other losses affect the overall efficiency as well.

Mass and volume: Clearly, because of enormous deep space mission launch costs, mass and volume of all subsystems should be minimized. The trend towards smaller and lighter-weight spacecraft necessitates the use of optomechanical designs for the laser resonator to minimize its dimensions and mass while maintaining thermal stability and radiation hardness. Diode-pumped solid-state lasers (including fiber laser) are inherently compact systems.

Lifetime of active components: The lifetime of the laser's active components (diode laser(s), modulators/pulsers and their drivers) should well exceed the expected operational lifetime of the mission. It is prudent to use redundant (block redundant or pump-laser redundant) lasers to increase the laser's lifetime. Data from diode laser manufacturers, for diodes with a few watts of continuous output power at 810 nm or 980 nm used as the optical pump sources, indicate lifetimes exceeding 50,000 hours (nearly 6 years). The higher the pump power, the lower the expected lifetime for the diode. Redundancy of the active elements, or block redundancy of the laser, is an effective means of extending the flight terminal's lifetime. Inclusion of linear arrays or grids of pump diodes also allows for de-rating the power level of an individual laser along with adding redundancy.

Radiation: Missions to the Earth's Van Allen belts, Jupiter, and Europa will encounter very challenging radiation environments. Most other mission destinations, for example, Mars and Pluto, have much more benign radiation environments and are not considered as challenging in terms of radiation hardness of components. Care should be taken to use radiation-tolerant diode lasers and optics (e.g., laser crystals, cavity mirrors, and intra-cavity pulsing devices). Typical diode lasers used as either pump or seed sources are based on GaAs material systems, which are fairly robust with respect to low-level radiation, induced defects compared to silicon-based electronics. Shielding can be an effective method of reducing the radiation tolerance requirements for laser components. Often, only a limited amount of data on the specific state-of-the-art component that is baselined is available in the existing literature. Therefore, additional testing and shielding is typically required. Section 5.4 provides more detailed explanation of radiation effects on lasers.

Thermal control and management: Current laser transmitters are only about 10 percent efficient. Therefore, about 90 percent of the input electrical power is converted to heat and optical losses. This heat has to be dissipated without affecting the optical alignment integrity of the terminal. The laser subsystem may be directly coupled to the terminal or may be located remotely, with its output beam piped in via optical fibers. The former is more efficient but can impart heat into the rest of the terminal, the latter is less efficient due to fiber-coupling losses, but affords much greater flexibility for thermal

management of the pump diodes, which are the primary source of heat generation in the optical terminal.

5.2.3 Candidate Laser Transmitter Sources

The above requirements on suitability for spacecraft use and the need for modulation to high data-rates, limit the pool of practical options, among those available now, to a class of lasers known as diode-pumped solid-state lasers. Included in this class are: (1) pulsed bulk crystal solid-state lasers, in the 914 nm to 1080 nm (e.g., neodymium: yttrium aluminum garnet [Nd:YAG] at 1064 nm), 965 nm to 1550 nm master oscillator power amplifiers (MOPAs); and (2) continuous-wave (CW) and pulsed fiber-amplifiers (such as erbium-doped fiber amplifiers (EDFAs) at 1550 nm and ytterbium-doped fiber amplifiers at 1064 nm). Lasers with wavelengths in the 2000-nm to 5000-nm region are also of interest due to their superior atmospheric transmission and reduced optical surface accuracy requirements for the transmitter telescope.

From an efficiency and technical maturity point-of-view, rare-earth-doped solid-state lasers and fiber amplifiers are the leading candidates for deep-space laser communications since they provide a combination of both high peak power and moderate average power. These lasers operate in the 1000-nm to over 2000-nm wavelength range. An alternate method is to use the second harmonic of this wavelength generated through nonlinear conversion. Table 5-7 compares the merits of five viable laser wavelengths. Assumptions are: a Mars mission of the range of 2.5 AU, 30-cm flight aperture diameter; a 5-m ground aperture diameter, hazy sky with 5-km visibility, cirrus clouds, and 70-deg zenith angle, PPM order of 128 and bit error rate of 1E–6. With today's detector technology and wavelength conversion efficiency, the 1064-nm laser appears to be the leading candidate.

The key requirements for a laser transmitter on a deep-space spacecraft include: (1) high electrical-to-optical efficiency and reasonable power consumption; (2) output power (average and peak); (3) excellent beam quality; (4) variable repetition rate; (5) reliability; and (6) low weight and small size.

The link parameters with significant wavelength dependence include laser output power; laser efficiency; atmospheric propagation; detector quantum efficiency and availability; background light (noise) at the receiver, and transmit/receive isolation.

Among the many types of lasers currently known, primarily diode-based MOPAs and diode-pumped solid-state (DPSS) lasers come close to satisfying all of the above requirements simultaneously. High power semiconductor lasers and bulk-crystal solid-state lasers, or doped fiber lasers and amplifiers that are amplitude modulated are useful in multi-gigabit links for near-Earth laser communications. However, these sources lack significant peak power and are more suitable for lower-order PPMs.

Table 5-7. Merits of five deep-space communication link wavelengths.

Wavelength (nm)	532	775	1064	1550	3100
Spacecraft's laser transmitter power (W)	14	10	20	20	14
Detector's detection efficiency (%)	90	50	35	35	30
Detector noise (megacount/s)	0.3	0.1	0.1	10	0.3
Transmit and receive optics losses. both ends (dB)	–7	–7	–7	–7	–7
Background light (W/cm^2 sr m) at 70-deg zenith angle (ZA)	0.186	0.144	0.0842	0.0325	7.00E-04
Atmosphere transmission at 70-deg ZA	0.3	0.47	0.55	0.6	0.3
Pointing loss (dB)	–2	–2	–2	–2	–2
Required peak power (W)	179	128	256	256	179
Channel capacity (megabits/second)	10	10	10	10	10
Code rate	0.05	0.05	0.05	0.05	0.05
Atmospheric coherence length (r_0, cm)	4.36	6.84	10	15.7	36.1
Seeing (μrad)	12.2	11.3	10.6	9.87	8.58
Link margin (dB)	–2.7	0.5	2.4	1.8	–0.43

5.2.3.1 Pulsed Laser Transmitters. Depending on the required average power, pulse width and data rate, either a single oscillator or an oscillator/amplifier will be required.

Single oscillators are typically limited in power to several watts. At higher power levels, control of the pulse width, laser power, pulse jitter, and pulse-to-pulse repeatability become more difficult. A MOPA scheme affords the amplification of a well-behaved oscillator through a suitable and efficient amplification medium. The oscillator and amplifier can then be individually tailored for high speed and high power, respectively.

The type of pulsed oscillator used will depend on the required data-rate. Examples are:

1) Amplitude modulated diode lasers provide modulation rates up to several GHz. However, peak power, pulse-to-pulse stability, and modulation extinction ratio of these sources are limited. For these lasers, peak power is typically just a few time above the average output power. Therefore, additional amplification stages would be required utilizing either a fiber, waveguide or bulk solid-state design [21]. These are detailed below.

2) Q-switched DPSS lasers can be pulsed to sub-megahertz levels, with the maximum data rate being limited by the available acousto-optic or electro-optic Q-switchers. These can provide pulses of one to a few ns with high modulation extinction ratio and high peak power. In a Q-switched laser, the population inversion is built-up by preventing feedback, and then it is switched to laser emission for a short period of time by improving the finesse or "Q" of the cavity to extract highly energetic pulses. The energy is stored in the gain material. This results in high peak power (on the order of 10 kW or more) and high average output power (watts) of the laser [22,23,24].
3) Cavity dumped DPSS lasers offer a high extinction ratio, high peak power, a short (a few nanoseconds) pulse width and pulse rates up to about 10 MHz. In cavity dumping, the intra-cavity field within the resonator stores the energy that is built-up by preventing laser emission; this field is then switched and dumped out of the cavity, by, for example, using polarization effects along with an electro-optical material. These lasers also provide moderate peak power and moderate average power [25]. Figure 5-18 shows a schematic of a version of a cavity-dumped laser.
4) Mode-locked lasers are capable of high peak power and modulation rates exceeding 1 GHz. However, the very short pulses involved add to data demodulation and encoding complexities [26].

For a uniform Gaussian or square wave pulse, the peak power (P_p) is related to energy per pulse (E) and pulse-width (pw) as $P_p = E / pw$. Also, the laser's average output power is related to energy per pulse and pulse-repetition frequency (PRF) as $P_a = E_p \times$ PRF. As shown in Fig. 5-19, maintaining a nominal value for average output power and pulse-width will result in steep reduction of the peak-power per pulse as the lasers' PRF increases.

Different amplifier media are available to boost the average power of the pulsed oscillator, up to 30 dB, while maintaining the output beam quality and the pulse-width, pulse-to-pulse jitter, and modulation extinction ratio of the oscillator. With all amplifiers, care has to be taken to avoid spontaneous lasing,

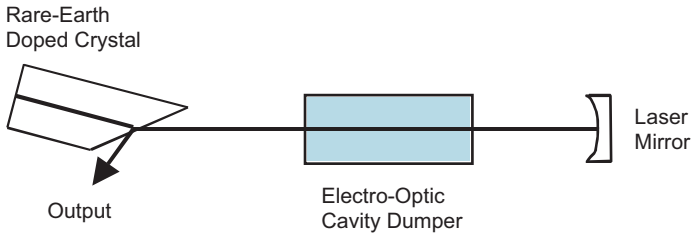

Fig. 5-18. Schematic of a high-power cavity-dumped oscillator.

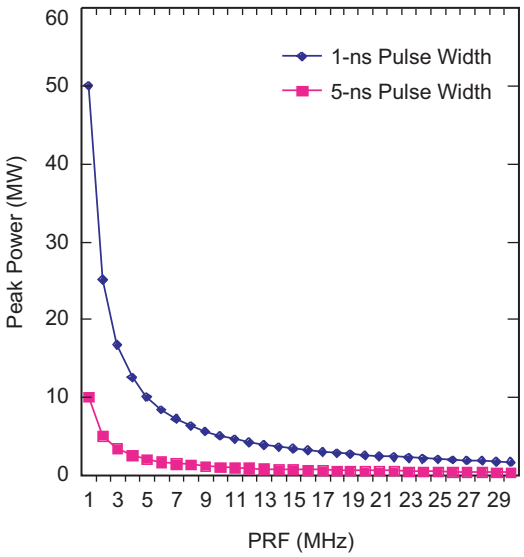

Fig. 5-19. Peak power as a function of pulse repetition frequency (PRF) for the case of fixed average power and pulse width (1 ns and 5 ns).

bulk damage, and parasitic nonlinear losses (such as Brillion scattering in fibers) [27]. Also, isolators may be required between the oscillator and the amplifier to avoid amplified spontaneous emission (ASE) and feedback to the oscillator. The amplification may be implemented in multiple stages. Examples of amplifier-based laser transmitters include: fiber waveguide, bulk crystal, and bulk-crystal waveguide. These are addressed separately below.

5.2.3.2 Fiber-Waveguide Amplifiers. Fiber-waveguide amplifiers use rare-earth-doped optical fibers for the amplification medium with optical pumping (excitation) provided by compact and efficient semiconductor diode lasers. Depending on the amplification architecture, fiber amplifiers (or lasers) can generate broadband or narrow linewidth output beams. These types of amplifiers, shown schematically in Fig. 5-20, provide a long amplification path (obviating the need for multi-passing), but have a lower threshold for damage than the bulk crystal counterparts. Single-mode fiber systems are limited in their peak power capability, but broadening of the fiber core while maintaining single-mode propagation is possible through a large mode area fiber design. Tens of kilowatts of peak power can then be propagated without being limited by fiber nonlinearities. Advantages of the fiber waveguide are ease of use, efficient coupling to fibers, and a relatively low noise floor. The challenges are nonlinear effects, excited state absorption, and cooperative upconversion. The

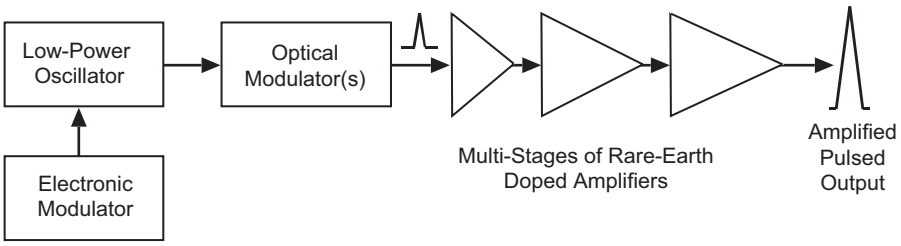

Fig. 5-20. Schematic representation of a pulsed fiber oscillator amplifier. As shown in the figure, the oscillator may be amplified directly or externally. The number of amplifying stages will depend on the output power characteristic requirements.

nonlinear effects include: stimulated Brillion scattering (SBS), stimulated Raman scattering, self-phase modulation, cross-phase modulation, and four-wave mixing. SBS is interaction of photons with acoustic phonons, resulting in lower SNR due to both signal reduction and introduction of additional noise [27].

In a fiber amplifier, a well-behaved oscillator beam is injected into a rare-earth-doped fiber amplifier that operates at the same wavelength as the oscillator. Common dopants for the fiber are: Nd, Yb, Er, or Yb/Er ions (co-doped) [28,29,30]. To generate amplification, the fiber oscillator is pumped with diode laser(s) operating at the absorption wavelength of the dopant. To generate high peak powers at the output of the amplifier, the oscillator is operated in the pulsed mode. The signal modulation (for communication) is imposed on the master oscillator by modulating and then amplifying the oscillator in one or more stages) [31,32,33].

A master-oscillator-power fiber-amplifier (MOPFA) source offers the following advantages:

1) Minimal requirement on structural integrity compared with the stringent resonator mirror alignment required for bulk crystal solid-state lasers.
2) Significant potential for higher overall efficiency relative to DPSS lasers, due to near 100-percent absorption of the pump beam in the medium (fiber), smaller quantum defect, and higher extraction efficiency.
3) Wider temperature tolerance for the pump laser wavelength shift (about 20 nm compared with about 1 nm for bulk crystal lasers).
4) Lower demand on tight control of the pump diode-laser temperature, resulting in significantly lower power consumption and higher overall efficiency.
5) Modulation extinction ratios on the order of 40 dB or more are feasible owing to a high degree of control on the master oscillator's performance. The fiber amplifiers do not alter input pulse characteristics from the master oscillator (MO) in a major way.

6) Shorter pulse-width and potentially higher pulse repetition frequency (PRF) due to simple control of the MO.
7) It is feasible to obtain narrow (sub-angstrom, <0.02 μm) linewidth with the use of Bragg gratings.

The peak power desired at a given data-rate drives the MOPA design due to possible nonlinear effects or damage to the fiber at higher peak powers.

Achievable gain and noise figure (NF) for fiber amplifier operation around 1000 nm is shown in Fig. 5-21 [34]. Selection of the transmitter wavelength depends on the specific mission requirements, efficiency, technological maturity, and compactness of the source at the time of selection. There is currently no general preference of one wavelength over the other since each offers certain advantages and suffers from some disadvantages with the benefits often outweighing the drawbacks.

5.2.3.3 Bulk-Crystal Amplifiers. Bulk-solid-state amplifiers are not peak power limited and also provide improved modulation extinction ratio. An example is an Nd:YAG amplifier that is optically pumped. Until the saturation limit is reached, generally the higher the number of passes through the amplifier, the higher the gain. A few different versions of these amplifiers have been reported [35].

Several different diode-pumped lasers have shown relatively high efficiency (~10 percent). The laser active elements (crystals) include: Nd:YAG, neodymium: yttrium vanadate (Nd:YVO_4), neodymium: yttrium lanthanum fluoride (Nd:YLF), and ytterbium:glass (Yb:glass), thulium: yttrium aluminum garnet (Tm:YAG), Tm, holmium yttrium lanthanum fluoride (Ho:YLF). In these crystals, the Nd, Yb, or Tm ions are trapped in a host crystal. The ions absorb light at a short wavelength and emit at a longer wavelength.

The fundamental wavelength of the Nd lasers is at about 1000 nm (for example, 1064 nm for Nd:YAG and Nd:VO_4). With a small nonlinear frequency-doubling crystal, it is possible to generate the second harmonic wavelength of these lasers at about 532 nm. Harmonic conversion efficiency is typically 30 to 50 percent, depending on the laser's peak power.

Tm and Ho ions emit laser light near 2000 nm. In terms of atmospheric propagation and background noise, this and longer wavelength ranges are superior to the 1000-nm wavelength range. However, these lasers are less efficient than 1000-nm lasers and operate best at low temperatures due to the three-level structure of the ions. Also, detectors at 2000 nm are significantly noisier than those for 1000 nm. Moreover, because of the very long upper-state lifetime of the ion (10 ms for Ho in YLF compared with 0.24 ms for Nd in YAG), the highest energy per pulse (or peak power) occurs at low repetition rates (near 200 Hz), making them unsuitable for significantly higher data rates. Lasers in the 3800- to 4200-nm range provide some of the best combinations of

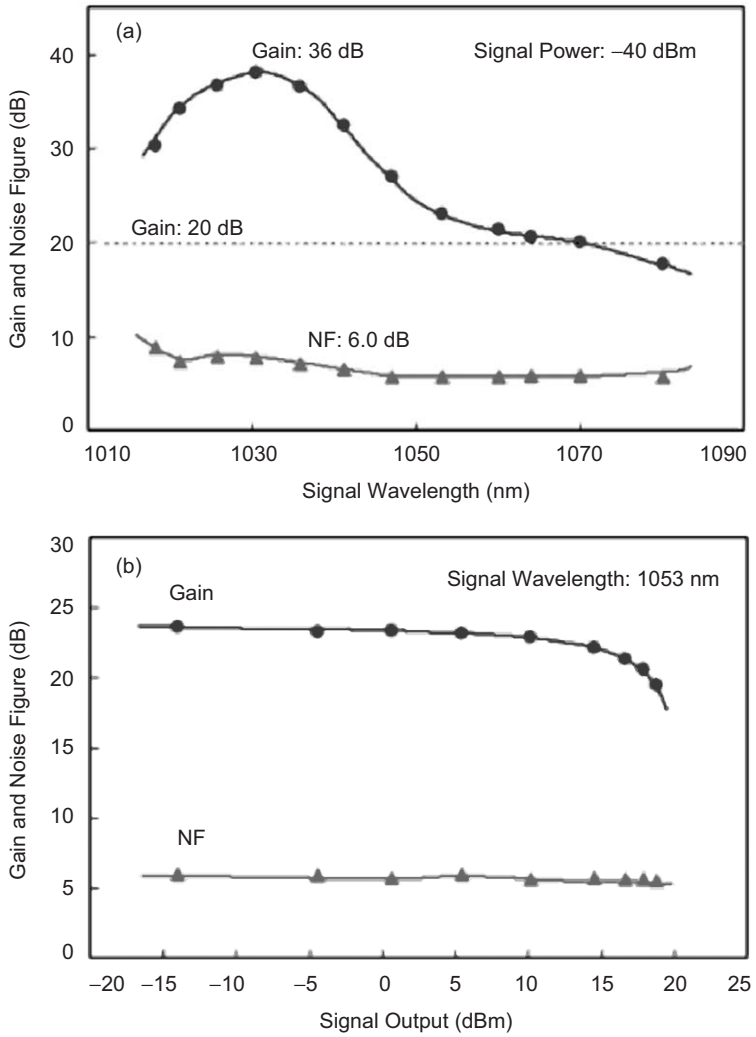

Fig. 5-21. Gain and noise figure (NF) characteristics of a ytterbium-doped fiber amplifier (YDFA) from 2003 catalog of Mitsubishi Cable America, Inc.: (a) signal wavelength and (b) signal output.

atmospheric transmission and lowest background light characteristics. However, efficient, compact, high power lasers are not readily available yet. Also, as discussed in Chapter 2, the space losses term increases quadratically with wavelength.

Energy per pulse (E_{pulse}) is given by equation: $E_{pulse} = P_{cw}T_s(1-e^{-1/T_s f})$, where P_{cw} is the continuous-wave power, T_s is the upper-

state lifetime of the active laser material, and f is the pulse-repetition frequency. Figure 5-22 shows a plot of the E_{pulse} as a function of PRF. For both Q-switched lasers in this example, the initial state inversion density saturates as the pumping time $(1/f)$ begins to be long compared to the respective upper-state lifetimes [36]. Assuming a CW power of 1 W, the saturation value for the pulse energy is (T_s X 1W); hence, for low pulse rates, the Ho:YLF laser pulses are 50 times larger than those for Nd:YAG. For high pulse rates, the pulse energies become asymptotically equal. For high pulse rates $f >> 1/T_s$, $E_{pulse} \simeq P_{cw}/f$, the laser's CW power is effectively collected over the pump time $1/f$ and emitted as a short pulse. For low pulse rates, the pulse energy saturates as

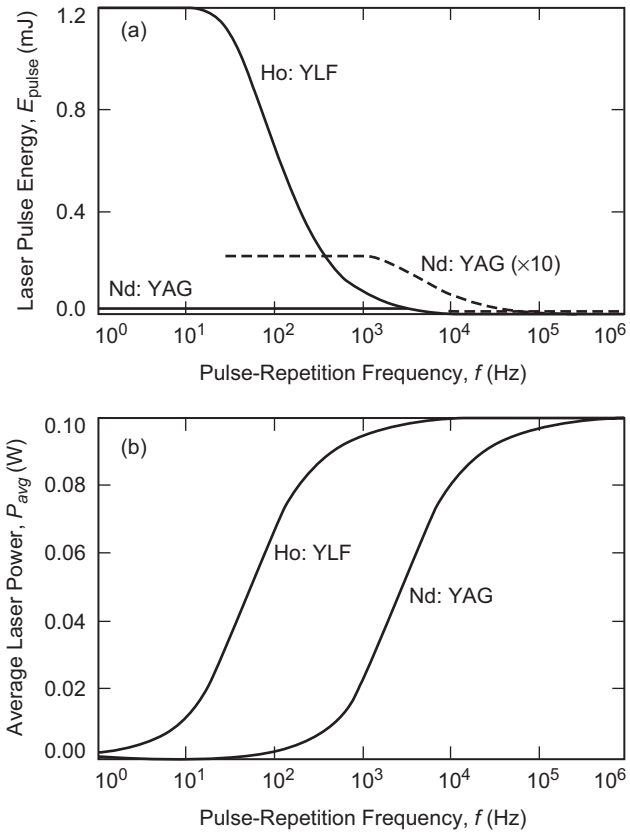

Fig. 5-22. Plots of the laser energy per pulse and average laser power as a function of pulse repetition frequency for Nd: YAG and Ho: YLF lasers: (a) output energy per pulse versus pulse-repetition frequency assuming continuous-wave output power of 1 W and (b) average output power versus pulse repetition frequency.

the pumping time becomes long compared to the "storage time" T_s. In the latter case, $E_{pulse} \simeq P_{cw} T_s$.

5.2.3.3.1 Bulk Crystal Waveguide Amplifiers. Multi-mode dielectric waveguides may be fabricated by bonding dissimilar crystals to an active amplifying medium and utilizing the self-imaging effect in the crystal. Circular, rectangular, tapered, and hollow waveguide geometries are possible with this scheme. This concept incorporates the waveguiding advantages of fiber-based designs with those of a bulk-solid-state crystal gain medium [37].

5.2.3.3.2 Pulsed-Diode Lasers. Pulsed-diode lasers or low (average power) pulsed DPSS laser (oscillators), amplified in fiber amplifiers, can generate the required peak power (kilowatt level), and moderate average power (watt level). Common fiber-amplifier media include: Nd:glass, Yb:glass, Er:glass, or a multiple doping of these ions in glass. Dual cladding, where a larger second clad region surrounds the core, allows the efficient coupling of the pump light from broad-area diode lasers though multi-pass absorption. The corresponding output wavelength varies in the range of 1030 to 1550 nm. Two factors may limit the usefulness of these types of MOPAs: (1) nonlinear effects in the fiber can cause a broadening of the spectral width of the laser (to about 2 nm); (2) the (glass) fibers darken when exposed to greater than about 0.1 Mrad of radiation. Glass is also inhomogeneously broadened, requiring broadband oscillator sources to get any efficiency.

5.2.3.4 Semiconductor Optical Amplifiers. Semiconductor optical amplifiers (SOAs) can provide linear amplification below their oscillating threshold. In an SOA, the population inversion of the atoms is reached by electrical pumping of the active semiconductor region and employing anti-reflection coating on the typical semiconductor laser mirrors. Benefits of SOAs are broadband (over 40 nm) amplification, high (~30 dB) net gain, compactness, and ease of integration with opto-electronic amplifiers. Their drawbacks are higher noise floor (compared with fiber amplifiers), highly nonlinear gain, and a low damage threshold for high-power pulses [38]. Various schemes have been developed to improve SOA performance, such as tapered gain regions and distributed feedback designs.

Depending on the power levels required, all of the above MOPA schemes may require a pre-amplifier prior to the primary amplification in order to obtain adequate saturated peak power levels. A pre-amplified DPSS laser is excited (optically pumped) with semiconductor diode laser(s). The diode laser itself is electrically more efficient than diode-pumped lasers and can be directly current modulated, but lacks significant peak power. Amplified diode lasers with moderate continuous-wave (CW) power and low peak output powers (in the watt class) are now available. Even the highest available semiconductor laser

powers do not support a link with adequate margin at deep space ranges greater than a fraction of an AU. High-power diodes also typically suffer from poor beam quality, and direct current modulation of the diode driver at high modulation rates results in poor efficiency. This is again due to the fact that for these lasers, the maximum achievable peak power is only a few times higher than its average power.

5.2.4 Lasers for Coherent Communications

Coherent communications require a frequency stable laser for the transmitter and at the receiver, and compatibility with the modulation schemes unique to optical communications. Critical aspects of coherent communications include frequency stability and laser linewidth. Diode-pumped solid-state (DPSS) lasers and amplified-frequency stable lasers can provide excellent frequency stabilities. DPSS lasers combine excellent spatial and longitudinal mode quality with high power and inherent redundancy. Mode stability requirements make these lasers more complex than those for direct-detection. Similar to the lasers discussed earlier, lasers for coherent detection are currently fairly inefficient, and lasers for coherent communication typically require an external modulator capable of handling high powers. Linear, ring, discrete-element, and monolithic resonator, as well as oscillator amplifier configurations of single frequency lasers have significantly matured. They each offer certain advantages and disadvantages, and their selection will be driven by the mission requirements. Methods to obtain single-mode operation include: intracavity etalon, ring resonators, mode-twisting techniques, and use of short cavities. Injection seeding is another scheme for enforcing single-mode operation in a high power laser. A variety of laser transmitter sources have been developed for coherent free-space communications [39,40,41].

5.2.5 Laser Modulators

Generally, two classes of amplitude modulators exist for laser transmitters. One class includes intra-cavity pulsers, such as Q-switchers or cavity-dumpers, that are used to generate pulses from solid-state lasers. The other class includes extra-cavity modulators, such as $LiNbO_3$ modulators, used in conjunction with the output of a semiconductor laser in a MOPA system. The advantage of the latter is that much higher repetition rates can be achieved. The modulators may operate in acousto-optic, electro-optic, or magneto-optic mode. Due to the excessive radio-frequency (RF) power needed for acousto-optic modulators, electro-optic modulators can be made more efficient than acousto-optic modulators by nearly an order of magnitude. However, driving most modulators simultaneously at high voltages (on the order of several hundred volts) and high modulation rates (above half a gigahertz) becomes challenging.

The pulse-width modulation method is a technique to optimize and control the output energy of the laser below the damage threshold of the crystal or fiber active medium. In this scheme, the pulse width is adjusted to maintain a desired output energy from the laser system. An output energy monitor operates as the feedback senor in a closed loop to pulse the pump diode lasers as the laser PRF and environmental conditions vary [42].

For coherent communications, modulation options include: an externally modulated laser; phase modulation; polarization modulation; and amplitude modulation. Every modulation scheme can be combined with homodyne or heterodyne detection. Phase-sensitive detection schemes are typically the most sensitive method, followed by polarization, and amplitude modulation. An electro-optic modulator may be integrated with the laser amplifier, or a bulk modulator may be utilized with the high-power laser. There is no clear advantage in terms of overall efficiency. Phase modulators are more efficient than polarization modulators, which are in turn more efficient than amplitude modulators.

5.2.6 Efficiency

Due to strict budgets for electrical power and mass on deep space missions, it is extremely important to maximize the laser transmitter efficiency. Higher overall efficiency translates directly into lowered mass for the flight terminal and reduced launch costs. The efficiency of a solid-state laser is determined by three key parameters: the pump semiconductor-laser diode electrical-to-optical conversion efficiency, η_D; the coupling or transfer efficiency of the pump light into the active medium, η_T; and the optical-to-optical conversion efficiency of the active-gain media, η_O These parameters can be further broken down to give the overall efficiency as [43–46]: $\eta = \eta_D \eta_T \eta_O = \eta_D \eta_T \eta_{abs} \eta_S \eta_Q \eta_B \eta_{ST} \eta_{ASE} \eta_E \eta_R$, where η_T is the optical efficiency of coupling the pump light, η_{abs} is the absorption efficiency of the gain media, η_S is the stokes efficiency or ratio of the output pump photon energy to input photon energy, η_Q is the quantum efficiency or fraction of pump photons reaching the upper laser level, η_B is the spatial beam overlap of the resonator modes with the upper state inversion, η_{ST} is the storage or depletion efficiency, η_{ASE} represents the loss due to amplified spontaneous emission which is the reciprocal of the depopulation rate of the upper laser level, η_E is the fraction of absorbed energy extracted and η_R is the resonator loss including reflective and scattering losses. Sometimes the efficiencies are grouped as the transfer efficiency, η_T, upper-state lifetime efficiency $\eta_U = \eta_S \eta_Q$ and extraction efficiency under Q-switched operation, $\eta_{eq} = \eta_{ST} \eta_{ASE} \eta_E$. Moreover, the wall-plug efficiency of a flight laser transmitter takes all the possible power requirements into account. These

include the thermal control of the laser components and electronics, auxiliary control electronics for monitor photodiodes, thermisters etc, power consumption for the Q-switcher or cavity-dumped and the DC-to-DC power conversion efficiency of all the drive electronics.

Table 5-8 summarizes wall-plug efficiency of some pulsed laser transmitters, for an example, with a few Watt of average output power. The optimized design assumes 50-percent (66 percent for fiber based) diode pump laser efficiency, where the theoretical analysis assumes 75-percent efficiency. The heat sink temperature determines the actual efficiency range.

5.2.7 Laser Timing Jitter Control

Several sources can contribute to the timing delay (or pulse jitter) of high repetition rate Q-switched and cavity-dumped diode-pumped solid-state lasers. These sources, which introduce either a fixed delay or in some other way effect the pulse build-up time in the laser cavity, include: electronics and switch-related jitter; longitudinal-mode build-up time jitter; and stored energy and build-up time jitter [47].

The first two sources are expected to contribute minimally or can be minimized; whereas, the last source makes up the bulk of the contributions to pulse jitter. The effect of each of the above contributors to jitter and the techniques proposed to alleviate them are described below. The pulse width of a pulsed laser optimized for high-efficiency energy extraction is typically about 1/3 of the build-up time, so maintaining the timing jitter to well under 10 percent of a pulse width requires that the laser energy and gain be controlled to within about 3 percent.

5.2.7.1 Jitter Control Options. Several schemes have been developed and tested for jitter control of diode-pumped solid-state lasers. These approaches, when implemented, should reduce the laser output pulse jitter to less than about 20 percent of the laser pulse width. Among them are:

Table 5-8. Comparison of overall efficiencies of solid-state lasers.

Pulsed Laser	Current Best Results (percent)	Estimated Optimal Efficiency (percent)
Nd:YAG or Nd:YVO4… 1064 nm		
With thermo-electric cooler	~10	22
With active loop heat pipe	~15	25
Yb-doped fiber amplifier, 1060 nm	~20	>30
Er-doped fiber amplifier, 1550 nm	~15	>30

5.2.7.1.1 Electronics and Switch-Related Jitter. Jitter from electrical and switching delays can be mitigated in a number of ways. Electrical delays are expected to be nearly constant from pulse to pulse and should contribute negligibly to timing jitter, or could be subtracted electronically. Jitter caused by electrical delays is constant and amounts to only about 10 percent of the pulse-width. Therefore, it may be accounted for and corrected.

5.2.7.1.2 Longitudinal-Mode Build-up Time Jitter. Random build-up of the laser power from noise will result in randomness of the modal composition of the laser's longitudinal mode, and that could result in timing jitter. Empirically, this (rms) timing jitter is about 10 percent of the pulse width (measured at full width at half maximum—FWHM) [48]. Injection seeding of the laser with an external source is a common method to alleviate this source of jitter.

5.2.7.1.3 Stored Energy and Build-up Time Jitter. The build-up time is affected by the repetition rate. Non-uniformity in the pumping time (such as, inter-pulse timing variations due to pulse repetition rate changes) and variations of the pump power cause variations in stored laser energy. Variations of the stored energy effect pulse build-up time, which in turn affect the output pulse timing and shows up as pulse jitter.

Possible techniques to mitigate the jitter due to stored energy include:

1) Time-variable (pulse) pumping. When the laser is continuously pumped for a non-uniform duration prior to each pulse, and the pulse is extracted with variable pulse-to-pulse timing (due to PPM), the stored energy is bound to vary. However, continuous pumping is not required, and the pump diodes may be pulsed (e.g., turned on and off in a controlled manner). If the pump diode is on for a period of time corresponding to the dead time (the inter-pulse period at maximum pulse repetition frequency) of a PPM pulse, the laser gain will always reach the same value. Subsequently, the pump diode power is lowered to a value that is just enough to sustain the gain. By this method, pulse jitter is reduced significantly since each pulse will have the same gain and build-up time.
2) Negative amplitude feedback with a constant offset provides stability and minimizes the timing jitter. In this case, varying the pulse-width of the output energy pulse while maintaining a current amplitude set point controls the laser output energy. By using a pulse-width-modulation-based control system, the current applied to the pump diodes is regulated at an efficient set point below the damage level, and the pulse-width is adjusted to maintain a desired output optical energy of the laser system.

5.2.7.1.4 Injection Seeding. One process that may eliminate electronics related pulse jitter is injection seeding. Synchronizing the RF oscillator with the pulse

trigger may also eliminate jitter caused by switching delays. In cavity dumping, for example, a mode-locked cavity-dumped laser minimizes timing jitter by taking advantage of the precision timing of its mode-locking effect.

5.2.8 Redundancy

Critical active components of the laser include the pump diode lasers, the driver electronics, and the control electronics. Critical passive components are the active laser element, the optical surfaces, and coatings on the optics. Aging, facet damage, and radiation effects are some of the potential failure mechanisms. Operation below the maximum rates safe current limits and operation at low temperature enhance the diode laser lifetime. Of all of the above-mentioned components, the diode laser lifetime is typically of highest concern. Multiple redundancy of the pump diodes, or block redundancy of the entire laser, is often a prudent approach to minimizing risk. The control loop and driver electronics are low-power, low-voltage devices and can be designed for an adequate level of redundancy. For passive elements, block redundancy may be applied.

5.2.9 Thermal Management

The thermal management of the laser transmitter is driven mainly by the need for thermal control of the pump lasers. The FWHM absorption bandwidth of most active bulk crystal laser mediums is narrow (approximately 1.5 nm for Nd:YAG and 9 nm for Nd: YVO_4). The pump laser diode wavelength varies with temperature on the approximate order of 0.3 nm/deg C. To pump rare-earth doped-crystals at the peak of absorption, therefore, the diode laser's temperature has to be controlled to within ±0.3 deg C and ±3 deg C for Nd;YAG and Nd:YVO_4 respectively.

For doped-fiber-based transmitters, the temperature-control requirement is much relaxed to approximately ±20 deg C, depending on the pump absorption band utilized. Yb doped glass lasers can be either pumped at around 980 nm or at the broader but weaker absorption peak at 915 nm. Active temperature control of the diode pump laser will thus be required. Options are thermo-electric coolers (TECs) and active-loop or passive-loop heat-pipes. TECs are typically inefficient. Conversely, heat pipes and radiators are more efficient but introduce additional mass.

Remote pumping of the laser (or amplifier) can significantly reduce the thermal management difficulties. In this case, the pump lasers are fiber-coupled and mounted in an area (e.g., a radiator) where their generated heat may be removed conveniently. The only drawback is the fiber-coupling loss that will be encountered. Remote location of the pump lasers (source of heat) will also simplify the optomechanical design for the laser-communication terminal.

A detailed finite element analysis (FEM) for the flight laser transmitter will help assess weaknesses in the optomechanical structure designed for the laser that might adversely affect the performance of the laser.

5.3 Deep-Space Acquisition, Tracking, and Pointing

Gerardo G. Ortiz and Shinhak Lee

5.3.1 Unique Challenges of Deep-Space Optical Beam Pointing

For optical communication links, mispointing of the transmit beam results in a variation of the downlink signal power. Because of the diffraction-limited transmit beamwidths used, the received signal power is extremely sensitive to the transmitter pointing error. A large transmitter off-point can lead to intolerable signal fades on the ground and significantly degraded system performance. This makes the spatial acquisition, tracking, and pointing (ATP) function critical to laser communication systems. This problem is compounded by the fact that the platform jitter present in the spacecraft due to dead-band cycle and random platform jitter are generally much larger than the transmit beamwidth. As a result, an ATP control subsystem is required to reduce the signal loss due to the pointing error. Such a subsystem must be capable of first acquiring a reference beacon source for absolute attitude determination in the presence of large attitude uncertainty. Then, it must accurately point the communication transmit beam to the Earth receiver in the presence of spacecraft orbital motion and microvibrations. To keep mispoint losses low (<2 dB), the required total pointing accuracy of the transmit signal is generally less than 40 percent of the diffraction-limited beamwidth, generally on the order of a microradian.

The two key issues for the ATP system are determining pointing knowledge of the Earth receiving station relative to the spacecraft (S/C), and then aiming the downlink beam to the receiving station. The pointing knowledge can be derived from acquiring and tracking on either an uplink ground based laser beacon or on passive celestial sources, such as the Earth, the Moon or stars. Due to its passive, non-cooperative nature, tracking on celestial sources has come to be known as beaconless tracking. Uplink beacon tracking can support pointing at short range and during opposition when the Earth image alone does not provide sufficient signal power for tracking. Uplink beacon tracking is an attractive alternative, although ground-based beacon uplink cannot provide the power required for high-rate pointing without needing additional inertial-sensors. Furthermore, at low Sun-Earth-spacecraft angles when the Earth image is brightest, the Earth background can cause a shift in the measured beacon centroid and interfere with beacon tracking. Finally, by requiring a clear path for uplink in addition to clear downlink path, a beacon-based system has a lower overall link availability.

For Mars- and Jupiter-range missions, the current baseline pointing and tracking approach is to perform Earth image tracking with occasional calibration using a laser beacon, Earth-Moon images, or Earth-star images. At high phase angles when the Earth image does not provide sufficient brightness for high rate tracking, inertial sensors (accelerometers) measurements are required to propagate pointing knowledge at a higher rate in between celestial reference updates. Control of a steering mirror is maintained by closed-loop control of a portion of the downlink reflected to a second detector.

Earth image tracking is desirable because of its high brightness (over most of the orbital period) and angular proximity of Earth intensity centroid to the receiver location. Among the challenges of Earth image tracking are the unknown Earth albedo variation due to cloud coverage and the solar stray light. The baseline design answers the albedo variation problem by performing periodic imaging of the Earth with other celestial references such as the Moon or nearby stars. These sources have well defined intensity patterns that allow accurate measurements of their position, but they require long integration times. The position of the Earth can then be calibrated using the measured celestial references' position and the known Earth ephemeris to determine the correction offset.

Since the Sun–spacecraft–Earth (SPE) angle becomes small during the mission, stray light control is important. At the low SPE angle, the subsystem is intended to operate 2 deg from the Sun; consequently, both optical surface quality and cleanliness need to be controlled to ensure low scattering of incident sunlight. Studies have shown that the required surface quality for the mirror can be achieved [49]. In addition, the optical design incorporates both a field stop in the telescope and a Lyot stop in the post secondary optics to control out of field scattered sunlight.

The innovation and uniqueness of JPL's ATP System has been in the development and integration of advanced components and subsystems, which improve random and system noise and dynamic range. Secondly, system-level improvements have been made in ATP algorithms and architectures to achieve ATP pointing accuracy to the sub-microradian level. Lastly, a unified ATP architecture has been developed that enables precise pointing throughout the Solar System.

5.3.1.1 State-of-the-Art ATP Performance. The objective of JPL's ATP work has been to develop and validate a complete set of acquisition, tracking and pointing (ATP) technologies with <1 μrad pointing accuracy for laser communications throughout the solar system. A comparison with the state-of-the-art systems is presented in Table 5-9. Ultra low pointing accuracies have been achieved for large systems such as the Hubble Telescope with a pointing accuracy of 35 nanoradians. Accurate relative pointing systems, such as Starlight, have also demonstrated low relative pointing control. But for the

Table 5-9. Comparison of some leading-edge precision optical pointing systems.

Organization	ESA (SILEX)	NASDA (OICETS)	Boeing (LADAR)	NASA (Hubble S/C)	NASA (Starlight S/C)
Accuracy (1σ)	0.22 μrad	0.86 μrad	10 μrad	35 nrad	0.5 μrad
Range	LEO-GEO	LEO-GEO	500 km (Ballistic target from airplane)	Observation	Up to 1 km separation
Applicability to deep space	Range-limited	Range-limited	Range-limited	Large, Expensive	Relative pointing only

Legend: ESA = European Space Agency
LADAR = laser radar
LEO = low Earth orbit
NASDA = National Space Development Agency (Japan)
OICETS = Optical Inter-Orbit Communications Engineering Test Satellite
SILEX = Semiconductor Intersatellite Link Experiment

optical communications system, the technologies need to demonstrate preciseness in absolute pointing accuracy.

5.3.2 Link Overview and System Requirements

The main function of the ATP system is to accurately and precisely point the downlink communication beam towards the receiver antenna. This is done by acquiring and tracking an external reference source and using that information to point the downlink to the receiver target. The performance of the ATP system is specified by its pointing accuracy.

5.3.2.1 Pointing Requirement. The communications link equation determines the relation between the mean received signal power and the transmitted power. Any transmitted power that is allocated for pointing of the downlink beam is power not used for communications. This means the data rate and pointing loss are inversely proportional, and any gain in pointing accuracy is a direct benefit to the data rate (i.e., a 3-dB decrease in pointing loss equals a 3-dB gain in data rate). Therefore, it is highly desirable to keep the loss allocated for imperfect pointing of the narrow laser beam very low.

Any mispointing of the laser beam that causes the far-field irradiance profile to be located off-axis from the receiver will result in a signal loss. This is called a pointing loss. Furthermore, keeping the narrow-angular-width laser beam pointed in the presence of spacecraft attitude and vibration disturbances becomes a formidable challenge. Therefore, in determining a link budget, some losses are allocated to pointing.

Another factor that impacts the quality of the link is the probability of burst errors. Due to the random nature of the tracking sensor noise and the control

system error, the achieved pointing accuracy has a statistical behavior and displays a probability of fade errors. The overall link designer must consider the level of fades that it can tolerate in order to provide the desired data rate and data volume. Therefore the data rate depends not only on the pointing loss allocation but also on the pointing-induced fade (PIF) probability allocation.

For high data rate links, the gain of the transmitter has to be high. This in turn, pushes the aperture to be large, typically in the range of 30 to 50 cm. Also, the lasers currently being considered and developed for deep-space communications have a wavelength in the range of 500 to 2000 nm. Therefore, the diffraction-limited beam width (at FWHM) is in the range of 1 to 7 μrad. Projects currently developing practical deep-space applications are considering implementation of lasers with transmitter 1064-nm wavelengths and 30-cm apertures [50,51]. Therefore, the expected diffraction-limited transmit communication laser FWHM beamwidth is 3.65 μrad.

The pointing requirement (also known as mispoint angle) depends on the allocated mispoint loss and the required probability induced fade (probability of burst errors). The pointing accuracy required of these systems depends on the power link budget allocation and the allowed PIF probability. The recent pointing designs for a deep-space optical communications link have set this total pointing loss allocation at 2 dB, which translates to a total mispoint angle of $0.42 \times \lambda / D$, see Fig. 5 23. For a 1064-nm system with telescope aperture of D = 30 cm, the total mispoint allocation is 1.5 μrad.

As an example of possible high data rates links and their pointing requirements, a 40-Mbps rate has been shown to be feasible for a Mars-to-Earth

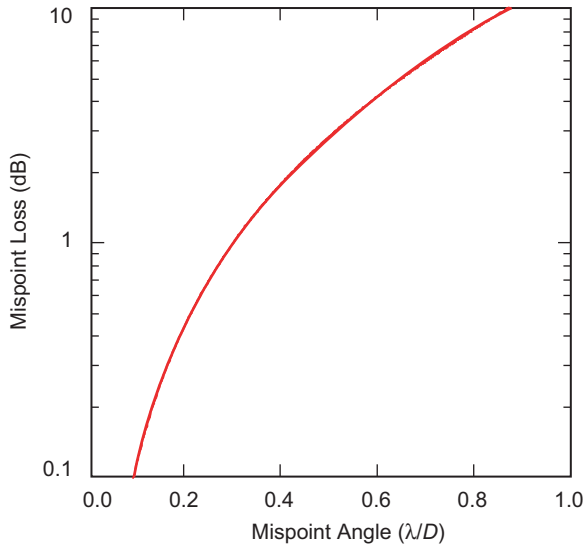

Fig. 5-23. Mispoint loss (dB) vs. mispoint angle (λ/*D*).

link [50] using free-space optical beams. This link was simulated at greatest range (2.7 AU), with a transmitter aperture of 30 cm, a downlink wavelength of 1064 nm, and an average laser power of 5 W. The design of this link allocates to the ATP System a pointing loss of 2 dB with a PIF probability of 0.12 percent. Another example is a design for a Europa Orbiter-to-Earth link with a data rate of 400 kbps at 6.4 AU [49]. This link had a transmitter aperture of 30 cm, a downlink wavelength of 1064 nm, and an average laser power of 3 W. This design allocated to the ATP System a pointing loss of 2 dB with a pointing induced fade (PIF) probability of 1 percent.

Transmitter pointing errors can result in undesirable signal fades at the receiver. These fades decrease the signal power level, which in turn cause a significant degradation of the coded link performance. Therefore, the probability of fades (aka. pointing induce fade probability) that can be tolerated by the link also needs to be specified as part of the ATP pointing requirement. For a particular jitter and bias error of the system, the resulting PIF will depend on the allowed mispoint angle (allowed mispoint loss). As an example, in Fig. 5-24, this relationship is plotted for a jitter and bias error of 0.5 μrad each (bias plus 3 times jitter for a total of 2 μrad mispoint angle). As can be seen, with this mispoint angle of 2 μrad, the probability of a PIF is about 0.3 percent.

Because of the statistics of the error distribution, the PIF depends on the particular distributions of the jitter and bias error, even though the total

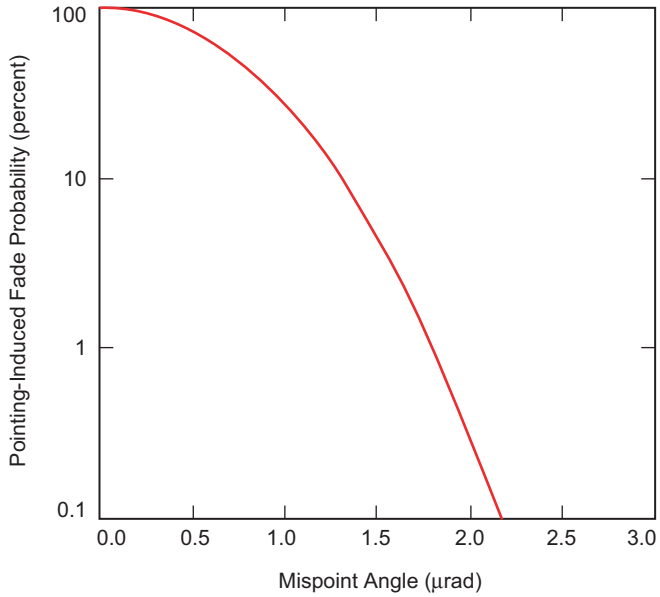

Fig. 5-24. PIF vs. mispoint angle (μrad). Jitter and bias are set at 0.5 μrad.

mispoint angle may be constant. Figure 5-25, shows this dependence by plotting the PIF as a function of allocated loss for cases of different jitter and bias distributions, but keeping the total mispoint angle constant. In this example, the total mispoint angle of bias plus three times σ equals 30 percent of the transmit beamwidth, but with different proportions between bias and jitter. As an example, for a 3-dB mispoint loss, the PIF varies from 0.7 to 0.3 percent for a {bias, jitter} allocation of {0.3, 0.9} µrad to {2.1, 0.3} µrad, respectively. To a first order, the PIF and loss are the same as a function of total mispoint angle, except for extreme cases where either bias or jitter are near zero.

The total mispoint angle includes jitter and bias errors. When designing an ATP system, allocations are made to these two categories depending on the components considered, the platform micro-vibration spectrum, and the particular link scenario (i.e., range, dead-banding, and noise background sources). These allocations have to be taken into consideration while simultaneously meeting the PIF requirement. In summary, to meet the requirements of mispoint loss with a certain PIF, care must be taken to design the jitter and bias errors judiciously. Of course, this value is limited by what the system components can perform, but it sets a preference upon which to set the requirements for jitter and bias errors.

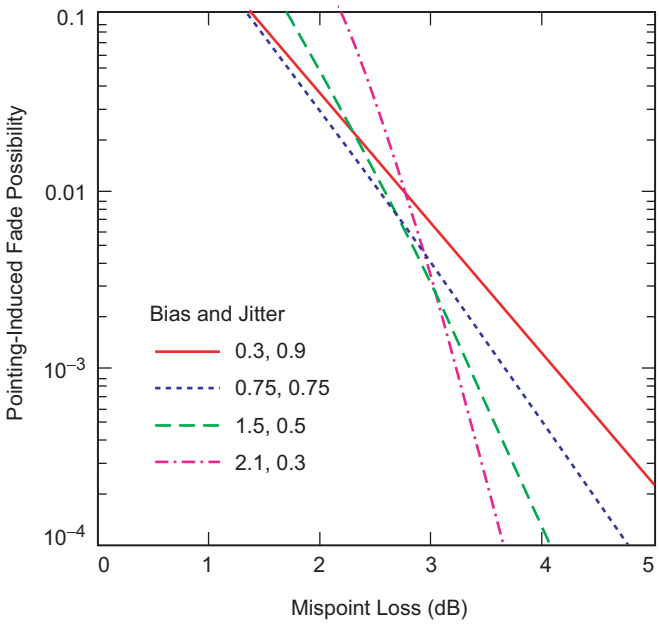

Fig. 5-25. Pointing-induced fade (PIF) probability vs. total mispoint loss (dB) showing dependence on varying jitter and bias error distributions.

5.3.2.2 Pointing-Error Budget Allocations. The pointing accuracy can be book kept in a pointing-error budget. The main sources of error are the pointing knowledge jitter, residual tracking jitter, knowledge bias, and misalignment bias due to thermal/mechanical effects. These relate to the main functions of the subsystem. The pointing requirement, as derived in the previous section, is allocated to these terms based on the estimated performance of the sensors, algorithms, mission parameters and environmental factors (e.g., spacecraft microvibrations and background signal). The total mispoint angle is equal to the bias term plus three times the jitter term (1 sigma). A reasonable allocation of the total mispoint angle partitions divides it into four parts and distributes it into one part for bias and three parts for jitter, as shown in Table 5-10 for a 30-cm and 50-cm flight terminal aperture with a 1064-nm downlink wavelength. This allocation can be later refined once estimates of the separate components are obtained. But, this initial apportioning serves as a guide to set the initial requirements that the subsystems would need to meet in order to support high rate deep-space optical communication links.

The jitter and bias error can be further decomposed into its major contributors. This is shown also in Table 5-10 with the major sources of jitter being the pointing knowledge jitter error (knowing the position of the receiver) and the residual tracking error, which is the amount of vibration not compensated by the tracking loop. The major sources of the bias error are the bias in knowledge of the receiver position and the bias caused by mechanical and thermal effects.

5.3.3 ATP System

5.3.3.1 Pointing Knowledge Reference Sources. Historically the pointing systems developed for optical communications have been based on using a ground laser as the reference beacon source. For deep-space links and

Table 5-10. ATP System Requirements (2-dB mispoint loss).

Total Mispoint Angle (assuming 1064-nm downlink wavelength)	1534 nrad (*D* = 30 cm)	921 nrad (*D* = 50 cm)
Total pointing jitter error (1 sigma)	383	231
Pointing knowledge jitter	271	163
Residual tracking error	271	163
Total pointing bias error	383	231
Pointing knowledge bias	271	163
Mechanical, thermal	271	163

particularly for planetary missions the pointing system called out for in these designs requires that an extremely powerful ground laser be used as the beacon source [49,50,51]. Some of the main impacts of these high power lasers on the system are to make ground operation difficult, to require reliable high power lasers, and to limit the range of the communication links.

Due to the required laser power, ground laser beacon concepts limit the range of the communication links. As is shown in Fig. 5-26, with current high power lasers, the range limit of laser-beacon-based pointing systems is limited to less than 0.4 AU. This range can be extended to about 3 AU, by introducing inertial sensors on the ATP subsystem to measure the high frequency vibrations, which then allows the laser beacon tracking camera on the flight terminal to integrate for longer exposure times and thereby improve its centroiding accuracy. Further studies have shown that the range can be extended to Jupiter with ground beacon lasers of the order of a few kilowatts [52].

The ground laser issues can be mitigated by utilizing pointing systems that rely on natural sources for the beacon. Since the pointing system still requires an absolute reference source, one can use passive celestial sources as the reference, such as stars or the Earth. This ATP approach has been called ‘beaconless’ due to its inherent nature of not using an active ground laser beacon as the reference source. With beaconless ATP concepts, the range of communications can be extended to cover the entire Solar System.

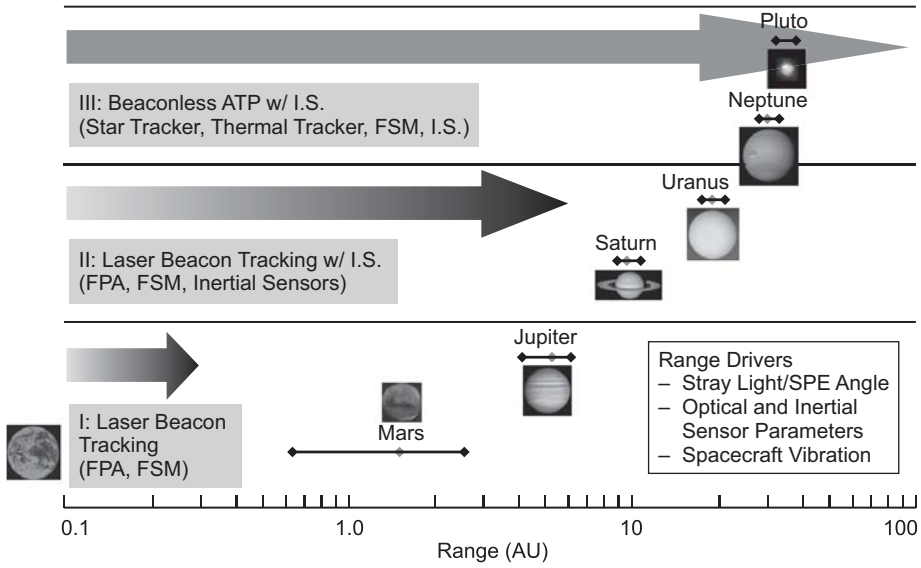

Fig. 5-26. Range capability based on ATP tracking architecture (I.S. = inertial sensor, FPA = focal plane array, FSM = fast steering mirror, SPE = Sun–probe–Earth-angle).

The technical advantages of celestial sources and corresponding sensors in the visible (also known as star tracker) and infrared (IR tracker) regions is to increase the signal to noise ratio (SNR) at high phase angles for the acquisition, tracking and pointing system. This high SNR then allows the flight terminal to accurately point the communications beam from anywhere in the Solar System to the Earth receiver without the need for a high power laser ground beacon. Both the star tracker and IR tracker concepts provide the reference information needed to precisely point the downlink beam. This information is provided at a high enough resolution to enable sub-microradian pointing systems. And with high bandwidth sensors (e.g., gyros, angular displacement sensors) integrated in the loop, the information is provided with sufficient bandwidth to compensate for spacecraft vibrations.

5.3.3.1.1 Optical References. To achieve the desired pointing performance, the orientation of the telescope with respect to the Earth must be determined. This requires a high-accuracy tracking mode to measure an absolute attitude (pointing knowledge) reference target (also known as beacon). The target can be an uplink beacon laser from Earth, the Sun-illuminated Earth-visible signal, the thermal emission from Earth, or other celestial sources, such as the Moon or bright stars. Optical references are used to provide absolute line of sight (LOS) pointing knowledge. From a celestial reference for which the J2000 location is also known in telescope coordinates, and given a S/C-to-J2000 attitude estimate (primarily for twist about the boresight), the full telescope-to-J2000 coordinate transformation can be computed.

The optical reference target is used to determine the LOS of the optical system. This measurement is corrected for distortion, jitter, etc. The (estimated) J2000 location of the Earth centroid and the measurement are then used in the attitude calculation, which in turn is used to estimate where the receiving station will be when the downlink signal reaches Earth. Except for the visible illuminated Earth, all these sources have a predictable light distribution where the mapping from a centroid measurement to a J2000 location is only limited by straylight, noise, S/C jitter, and modeling error. In the case of the visible Earth image, it is additionally limited by the ability to compensate for albedo variations that are a function of weather.

Key considerations for the selection of the optical absolute attitude reference source include the following.

1) Expected signal level and track rate: how bright and how high a track rate can be achieved?
2) Signal availability coverage: When is the source available?
3) Stray light considerations: How significant is the stray light contribution during usage?

4) Target feature location knowledge: How well do we know the location of what we are measuring (e.g., the brightness centroid of the Earth shifts due to albedo variations, contributing to error in the knowledge of the location we are measuring) contrasted to an error in the measurement process itself?
5) Derived point-ahead accuracy: How well can we determine the pointing for downlink?
6) Expected signal wave-band and detector responsivity.
7) ACS requirements, attitude knowledge required from the S/C: Assumptions are that the S/C gives attitude knowledge better than 1 mrad about the telescope boresight, allowing a single target to be used for the tracking function. Needed are 1 mrad in twist for point-ahead, which is generally available, and 160 μrad in twist for Moon-Earth tracking.
8) Field of view (FOV) considerations: For optimal performance in Earth tracking, the FOV should be as small as possible while still containing the Earth during acquisition and dead-band motion. For example, the combination of spacecraft dead-band and pointing uncertainty appear to require about 5 mrad minimum FOV diameter for a Jupiter range.

5.3.3.1.2 Summary of Possible Pointing Targets. Obtaining an accurate celestial reference is a critical step in pointing the optical downlink. Table 5-11 summarizes five tracking approaches. The Earth image provides a bright reference that is close to the receiving location both in the visible band and the long-wavelength infrared (LWIR) band. In the visible tracking approach, the Earth albedo variation is calibrated with occasional laser beacon, Earth–Moon, or Earth–star image tracking. At high phase angle when the Earth image is dim, uplink beacon tracking can be used to provide the accurate reference.

Except for the star tracking option, the S/C attitude is required for downlink pointing (boresight twist is needed for the downlink pointing). For star tracking, multiple stars are expected to be in the FOV, and the point-ahead angle is determined from ephemeris and star measurements. All options have outage at superior conjunction. The star tracking option will probably require a larger FOV to guarantee coverage, to possibly as large as 2 deg.

5.3.3.2 Pointing System Architecture. Over the past decade, JPL has adapted the design of JPL's optical ATP architecture to encompass all deep-space ranges within the Solar System. The driving factor behind this development is the lack of a high-intensity reference source in deep space. The high-intensity reference is a critical source of information for overcoming the two largest pointing errors: estimation of the receiver location and S/C vibrations. Current laser beacons do not have sufficient power to reach deep space. Alternative reference sources such as stars or the Earth have their own strengths and

Table 5-11. Comparison of various tracking approaches.

Approach	Requires	Notes	Sun Geometry Limited	Inertial Sensors Required
Laser beacon tracking	Requires uplink signal	Only applicable at close (<1 AU distances) without inertial sensors	Yes	Not near to Earth
Visible Earth-only tracking	Albedo variations cause center of brightness shift. Calibrate/live with offset error	At close distances, edge tracking can provide updates, or defocus downlink	Yes	During high phase angles
	At 0 phase and 1 AU, Earth has a magnitude of –3.8	Signal varies with phase angle/distance ~40× worse at Pluto than at Jupiter		
Visible Earth–Moon tracking	Moon has predictable Albedo, and can help determine albedo offset	Degraded if Earth–Moon has a large separation or is too close	Yes	During high phase angles
	Error of Moon measurement induces pointing error bias	Signal varies with phase angle/distance ~40× worse at Pluto than at Jupiter		During long Moon exposures
	Moon 40 times dimmer than the Earth	Moon requires 40× more exposure time		
Star tracking	Requires stars to be in FOV Requires inertial sensors	Low signal	No	Yes
	Pointing based on J2000 coordinates/ attitude	Track signal not a function of distance		
	May require offset pointing for stray-light rejection	10–20 Hz for 10^{th} mag stars		
LWIR Earth tracking	Requires cooled sensors (QWIP, HgCdTe)	Very low phase variation	Yes	Yes
	Edge detection to reduce bias error			

HgCdTe = mercury cadmium telluride
QWIP = quantum well infrared photodetector

weaknesses [53,54]. In response to these needs, a unified pointing control architecture for the system has been utilized.

A combination of a low intensity reference source and measurements of S/C vibration are used to provide equivalent pointing as a high intensity reference source. The resulting constraint from the reference source and the addition of S/C vibration measurements led to a new architecture of the

pointing system for deep-space missions. Figure 5-27 shows the diagram and the information flow among the key elements of the pointing system. A typical operating scenario is as follows: the pointing offset is computed from the telescope attitudes and the receiver location. The computed pointing offset is used to command the high-bandwidth steering mirror to direct the downlink laser beam. The telescope attitudes are estimated from the S/C vibration measurements. The receiver location is estimated from the centroids of a reference source seen on the focal plane array (FPA) and measurements of S/C vibrations. The role of the S/C vibration measurements is to compensate for the smearing and jitter of the beacon during the long exposure of the FPA due to the low intensity of a reference. This compensation is done through the enhanced centroid measurement processing which makes use of the jitter and motion during image exposure. The S/C vibration (high-frequency vibration) may need to be dampened to meet the stringent pointing-error budget.

In order to meet sub-microradian pointing requirements, the key pointing system elements should perform with high precision over a broad bandwidth. These elements are the inertial sensors, the FPA, and the steering mirror. The accuracy of the inertial sensors depends on the frequency response over the range of the vibration spectrum, electronic random noise from both the sensor and the sampling device, and any error from the algorithm that performs

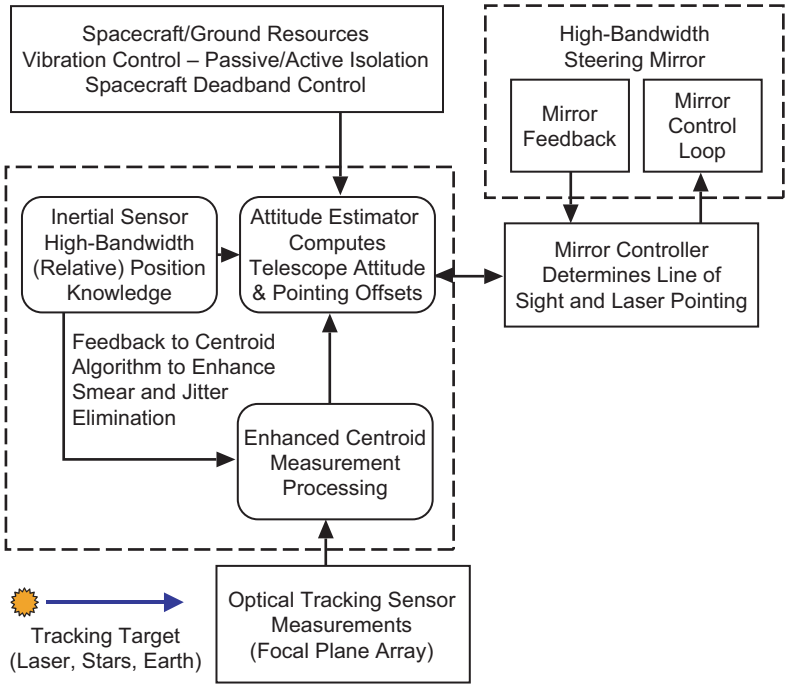

Fig. 5-27. Unified deep-space ATP architecture.

filtering and/or integration. The challenges have been in developing the integration and calibration algorithms for the initial velocity estimation, compensation for acceleration bias and scale factor bias. The main role of the FPA is to collect photons from the low-intensity reference and transfer the high-SNR signal to the sampling device, which will be used by the enhanced centroid algorithm to produce an accurate estimate of the reference position on FPA. The critical parameters of the FPA are low read noise and sub-window read capability at relatively high speed. The challenge on the steering mirror control loop is the rejection of S/C vibration on the line of sight (LOS) of the downlink beam. This requires a high-bandwidth closed-loop control, which can be achieved with the proper design of a mirror driver (controller).

5.3.3.3 Design Considerations. Because of the large trade space available to the system designer, one can easily choose to optimize the design in one aspect and ignore the other problems. An example of this is the flight-ground trade-off. One can require a larger aperture and higher power on the ground and simplify the flight system design. The optical communication technology, which is sensitive to background radiation and pointing loss, will require some adjustment in the operational methodology and mission planning process, both requiring mission inputs. In this section, major system drivers and acquisition and tracking/pointing requirements will be discussed. External parameters or constraints affecting the system design can be defined as system drivers. These parameters influence the system design at various stages with different impacts. Major system drivers include S/C attitude uncertainty, S/C vibration, stray light, and link/mission parameters (such as SPE angle, range, aperture size, wavelength, and FOV, mispoint loss allocation, and pointing induced fade probability). Smaller SPE angles give more straylight. Large range and smaller aperture size require more laser power. Wavelength directly affects transmitting/receiving efficiency among many other impacts. FOV influences acquisition /search time and tracking accuracy. Each of these system drivers is discussed in terms of its impact to the ATP system.

5.3.3.3.1 Pointing Error Sources. The overall pointing error of the subsystem includes a random contribution (which varies with a short time constant and can potentially vary from frame to frame) and a quasi-static error term, which is slowly varying.

The sources of the static pointing error include algorithm error, the error in estimating the Earth–receiver position, the ephemeris error, error in computing the point-ahead angle, and alignment errors. For example, for Earth tracking, the largest static error source is allocated to the error in estimating the geometric center of Earth using the image centroid. This error is due (primarily) to the uncertainty in image intensity distribution, and it will require periodic Earth–Moon or Earth–star calibration to achieve the allocated pointing

accuracy. The boresight alignment error and errors due to thermal-mechanical distortion are the next largest sources of static errors. These sources can be controlled with careful opto-mechanical design and with careful alignment of the optics.

The two major contributors of random pointing error are the sensor noise and control error. The sensor noises include the noise introduced by the random photon noise (shot noise) and errors introduced by the pixel non-uniformity and spatial quantization. The control loop noise includes the uncompensated platform jitter (vibrations) and noise introduced by the control loop electronics.

5.3.3.3.2 Spacecraft Attitude Control Uncertainty. The S/C attitude control uncertainty impacts the design of the FOV of the acquisition detector such that the beacon needs to be always in the FOV of the acquisition detector. Therefore, the FOV of acquisition detector should be larger than the twice the attitude control uncertainty (since this covers only one side of the 3-sigma value of the attitude control uncertainty). If the acquisition detector is also used as the tracking detector, the tracking error will increase as the FOV increases due to the reduced per pixel resolution. Therefore, there will be a trade-off between the required tracking accuracy and the acquisition FOV.

To define a typical range of S/C attitude control uncertainty, 34 spacecraft were surveyed on the JPL mission and spacecraft library website [55]. These were grouped into two categories: 27 Earth-orbiting spacecraft and 7 deep-space spacecraft. A histogram of the spacecraft attitude control uncertainty is shown in Fig. 5-28. Both types of spacecraft have been built with a wide range of attitude control capability. The control uncertainty ranged from less than 1 to

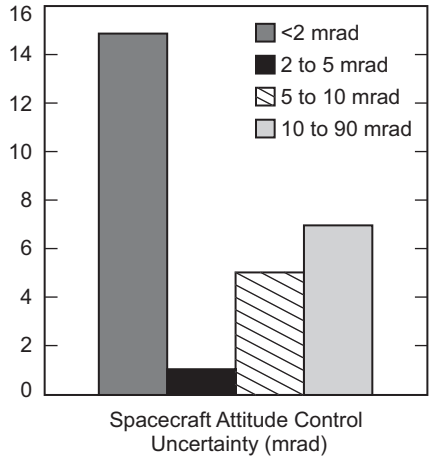

Fig. 5-28. Histogram of spacecraft attitude control uncertainty (mrad) from a survey of 27 Earth-orbiting and 7 deep-space craft.

90 mrad. In both types of spacecraft, the majority fall within +3 mrad in attitude control. This implies that an acquisition detector with an FOV of 6 mrad will cover most missions.

5.3.3.3.3 S/C Vibrations. Spacecraft platform vibrations cause jitter of the downlink beam, which increases the mispointing loss. Compensation for S/C vibration is necessary for precise pointing and generally requires high-speed updates of the downlink steering mirror on the order of few kilohertz. Without proper compensation, these vibrations can result in a mispoint of the beam on the order of more than 10 µrad depending on the vibration power spectral density (PSD).

Several S/C vibration power spectral densities (PSDs) are shown in Fig. 5-29 for the following spacecraft: Space Shuttle, Landsat, Bosch, ESA's communications satellite (Olympus), High Resolution Dynamics Limb Sounder (HRDLS), Relay Mirror Experiment (RME). As an example of mispoint jitter, the total RMS jitter for the Olympus S/C without any compensation is about 16 µrad. To reduce this jitter effect a compensating control loop is designed to stabilize the outgoing optical beam. The design of the control loop depends highly on the frequency content of the vibrations as shown on the PSD plots. The magnitude and frequency content of the spacecraft vibrations drives the need for the control system to include varying levels of passive isolation, active isolation, and active compensation to reduce the effective residual jitter impacting the downlink beam.

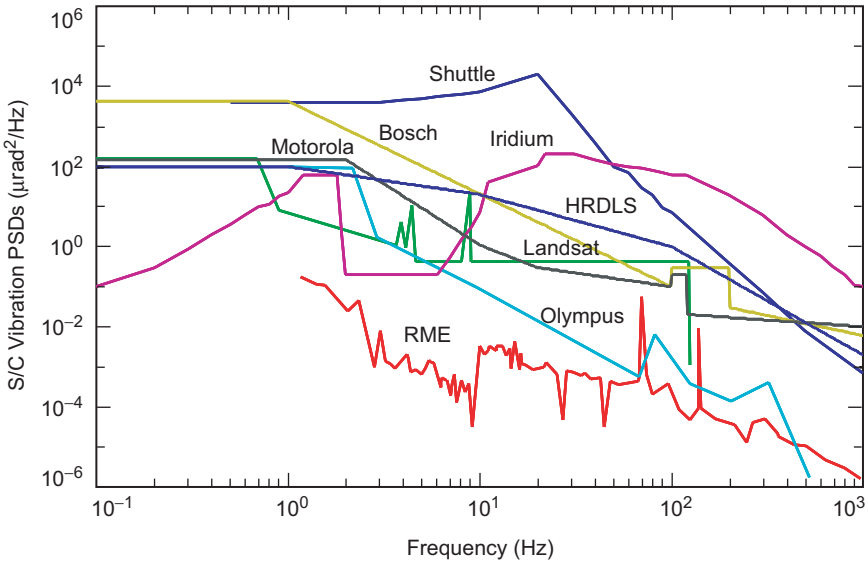

Fig. 5-29. Sample of spacecraft vibration power spectral density characteristics.

5.3.3.3.4 Detector NEA and Bias. For the image detector (or any array detector), there are several components of measurement error. The detector noise equivalent angle (NEA) is usually used to summarize the effects of errors caused by photon statistics, read noise, or other sources, which are temporally random. There are also several bias terms that are functions of the detector pixelization or optics design that may appear to be random. First, there is the high-frequency spatial bias (the S-curve, or centroiding bias) that is approximately periodic on the pixel pitch and is determined primarily by the image distribution—the point-spread function relative to the pixel response function. Low spatial frequency (LSF) bias (or macro distortion) is due to optical distortion, detector shape (flat versus spherical), focal length changes, and chromatic effects that will cause slowly varying offsets as a function of position in the FOV. The LSF bias terms are generally expected to be calibrated and included as part of the focal length calibration. The key elements of the image detector to consider are quantum efficiency, read noise, dark current detector pixel non-uniformity, full well size, and analog-to-digital (A/D) converter resolution.

- Quantum Efficiency. The ability to convert photons to electrons. This is really a simplification (like an average value over a spectral range) of the spectral response, which determines how well the detector converts photons as a function of wavelength.
- Read Noise. We use this term very loosely to mean the noise contributed in the course of reading a pixel.
- Dark Current Effects. Are separately allocated, since they are dependent on exposure time and temperature.
- Detector Pixel Non-Uniformity. Refers to the variation of the average pixel response over the detector.
- Sub-Pixel Response Non-Uniformity. Gives the variation of response within a pixel.
- Full Well. The maximum integrated signal that can be stored in a pixel and measured. Usually the full well is determined by the point where the light transfer curves become non-linear.
- A/D Resolution and Preferred States. The number of electrons per A/D least-significant bit (LSB) determines the resolution. Any preferred states in the A/D converter are modeled as an additional noise source and as reduced resolution.

The following equation for NEA is an approximation, and is based on the center of mass centroid calculations. For a well-known, static image distribution, a reduction in NEA by $\sqrt{2}$ can likely be achieved. The benefit of the center of brightness algorithm is that jitter or small angular rates do not affect the measurement as much as a “fitting” or shape dependent algorithm.

The derived equation separates the centroid noise due to the signal itself, and expresses the noise variance as the sum of the image centroid noise and the per pixel noise, such as read noise or background (e.g., stray light) noise. Errors in the background and A/D conversion are included with the R_{ij} defined below. All quantities are expressed in electrons.

Δt = the exposure time (seconds)

S_{ij} = Signal in the *i*; *j* pixel

R_{ij} = Non-signal noise contribution in the *i*; *j* pixel. For each pixel, R_{ij} is assumed to have the same variance, namely Var(R_{ij}) = Var(R_F)+ $\Delta t R_T$ with integration time Δt. This emphasizes the time-dependent behavior for stray light and dark current.

R_F = Fixed per pixel noise (1σ), such as read noise. A typical value is 5 e to 10 e for the low noise FPA such as scientific quality charge-coupled devices (CCDs).

R_T = Per pixel background signal rate (including stray light and dark current).When separating external (stray light) from detector generated (dark current), they are denoted R_{ET} and R_{DT}, respectively. The noise variance terms are $\Delta t^2 R_{ET}$ and $\Delta t^2 R_{DT}$.

X_C = Centroid computed from signal + noise

I_S = Total star signal intensity, electrons/second.

S = Total image signal, $S = \Delta t I_S$

N = Truncated half width of centroiding area. See usage in equations below.

N_P = Number of pixels involved in the centroiding area, $N_P = (2N+1)^2$

$$NEA^2 \approx \mathrm{Var}(X_C) = \left(\frac{S + Np\left(\mathrm{Var}(R_F) + \Delta t R_T\right)}{S^2} \right) \frac{N(N+1)}{3} \qquad (5.3\text{-}1)$$

Note that with non-uniform pixel response, the error due to pixel non-uniformity can become a major contributor of the NEA.

5.3.3.3.5 Digital Quantization. To convert electron counts in a pixel to digital values, an A/D converter, typically 8 to 12 bits, is used. The A/D output is referred to as DN (digital numbers, or data numbers). Because the number of electrons can be quite large (50,000 to 250,000 electrons) compared to the resolution of the A/D converter, full knowledge of the electron count is lost due to the truncation error, and so is some knowledge of the image. This error is treated as being a random distribution; for the case where the A/D has no

preferred states, it would be described by a uniform distribution. Since we estimate the mathematical centroid of the image from the DN, the error due to this conversion is needed to evaluate the effect of the noise sources. For analysis, the noise contribution due to quantization is a uniform distribution:

$$\begin{aligned}\text{A/D Variance} &= 1\sigma^2 \text{ noise/pixel} \\ &= \frac{1}{12} \times (\text{number of electrons/resolution})\end{aligned} \tag{5.3-2}$$

At best, the resolution is the number of electrons per DN for a perfect A/D converter. Using the value of the number of electrons per 1.5 DN is probably a better estimate of what is actually achievable.

5.3.3.3.6 Interfering Image Sources (Interlopers). If there are interfering targets in the same measurement area (e.g., centroiding window), the composite measurement will be shifted. Assume a target with signal BE and centroid location (x_E, y_E), and a close, interfering object with centroid (x_I, y_I) and brightness B_I. Then the combined system has centroid

$$\left(x_I, y_I\right) + \frac{B_I}{\left(B_I + B_E\right)}\left(x_E - x_I, y_E - y_I\right) \tag{5.3-3}$$

Consider an example where the Earth is 20 μrad in diameter, with the *y* detector direction aligned with the Earth pole, and a star near the pole and 2.5 magnitudes dimmer (i.e., 2.5 magnitudes if the Earth is fully lit and 10.0 magnitude if the Earth is at a 160-deg phase angle). The system centroid shifts by

$$0.09 \times \left(x_E - x_I, 10\ \mu\text{rad}\right)$$

The error is nearly 1 μrad in the *y* axis alone. The 1-μrad error will result in pointing loss. The probability of a star being near, but not behind the Earth is small, but there will be times where the image is degraded in this way. Once a mission is planned, there should be an evaluation of the stars that are angularly close to the Earth (seen from the S/C) to predict/plan degraded pointing or devise workarounds.

5.3.3.3.7 Pixel-to-Pixel Non-Uniformity. Pixel non-uniformity is a property of the individual pixel response, and hence, it does not change during short periods of time. (It can change with radiation damage.) The effects on centroid error appear as a slowly changing bias while an image moves across a pixel. There are two effects to consider. The first is when there is high background signal, such as high stray light. This can be treated in an RMS sense; if the

(uncalibrated) RMS non-uniformity value is σ_U, and the background rate signal is R_T electrons per pixel, then the RMS spatial noise variance is $(\sigma_U \Delta t \times R_T)^2$ per pixel for an integration time of Δt. This can be treated for simplicity in the analysis as though it were a read noise term. Note that the error uncertainty contribution grows with the signal (linearly with time), not with the square root of the signal as do noise contributions, so that this contribution becomes much worse as the background grows.

The second effect is when the scene background is low, and only the image signal is of importance. Considering the worst case when only one column is not uniform while the other columns are uniform for an $M \times M$ centroid window where ρ is the pixel responsivity, $\rho = 1 \pm$ the pixel non-uniformity. The corresponding centroid error due to the pixel non-uniformity is

$$C_x = \frac{M(M-1)(\rho-1)}{2(M(M-1)+M\rho)} \tag{5.3-4}$$

If the responsivity, ρ, is a uniformly distributed random variable (with half the range corresponding to the non-uniformity value), then the RMS error will be $C_x/\sqrt{12}$. If the responsivity, ρ, is a Gaussian random variable, then C_x is the RMS centroid error due to the pixel non-uniformity. The magnitude of this error is therefore proportional to the size of the centroid window and the distribution and magnitude of the pixel non-uniformity.

5.3.3.3.8 Platform Jitter Considerations. Platform jitter micro-vibrations (due to the amplification or transmission by the S/C or terminal or optics structure) will degrade downlink pointing. Such platform jitter can be induced by reaction wheels, thruster rings, external torques, or other moving parts on the S/C, such as the steering mirror for downlink control, or other instrument steering mirrors. The key factors in minimizing platform jitter are

- Passive or active isolation of the optical communications terminal (OCT) from the S/C.
- Using common mode design for measurement and control whenever possible.
- High rate measurement loop using inertial sensors to measure the change of motion of the telescope pointing.
- High rate measurement loop to determine the direction of the pointing steering mirror in telescope coordinates.

5.3.3.3.9 Point-Ahead Angle. Here we assume that the Earth is moving at a constant angular rate about the Sun, which gives a velocity of about 30 km/s. When the reference measurements are based on the Earth/Moon, then twice the

one-way light time is used to calculate the difference between where the Earth position will be when the downlink signal reaches the station, relative to the OCT-measurement-calculated location. When only stars are used as references, then there is no such effect. The computation of the Earth location at the downlink signal arrival time is now relative to the absolute J2000 frame, and may be worse or better, depending on the knowledge of the J2000 Earth location in the star measurement-based frame.

At a distance D from the Earth, the round-trip light time is $2D/c$, where c is the speed of light in kilometers per second $= 2.998 \times 10^5$ km/s. The worst-case point-ahead angle (at inferior conjunction, 180-deg phase angle) is independent of the distance between the S/C and the Earth, and it is given by

$$\begin{aligned} \text{Point–ahead angle} &= \frac{2D}{c} \times \frac{\text{projected velocity}}{\text{D}} \\ &= \frac{2 \times 30}{(2.998 \times 10^5)} = 200\ \mu\text{rad} \end{aligned} \tag{5.3-5}$$

As an example of the effect, with a twist error of 1-mrad accuracy about the boresight, the induced point-ahead error is 0.2 μrad radial. During a full Earth orbit, this error will vary between + 0.2 μrad due to the changing point-ahead, with the largest at 0 and 180-deg phase angle.

The worst-case error in the receiving station location due to rotation is given by

$$\begin{aligned} \text{Earth rotation displacement} &= \cos(\text{lat}) \times 3.6 \times 10^{-5} \\ &\quad \times (\text{angular diameter})/\text{second} \end{aligned} \tag{5.3-6}$$

where cos(lat) is the cosine of the receiving station latitude.

For a receiving station located on the equator, and at a distance of 4 AU, Earth is about 20 μrad in diameter. For this case, the receiving station moves up to 0.1 μrad relative to the S/C in 140 s. For beacon tracking, the same considerations are required when considering the location of the uplink beacon (there possibly may be common-mode cancellation).

5.3.3.3.10 Solar Conjunction Availability. Limited solar-conjunction availability is imposed by the Sun-spacecraft-Earth geometry as well as by the Sun-Earth-spacecraft geometry, which contributes stray light. In addition to the effect of increased background noise at the Earth receiver, at small Sun-Probe-Earth (SPE) angles, the spacecraft's pointing and tracking detector, if co-boresighted, may experience an increase in background noise due to the photon noise in the straylight from the Sun, leading to an increase in pointing error and, at worst case, inability to detect the Earth image or uplink beacon signal.

5.3.3.3.11 Weather-Related Availability of Ground Laser Beacon. The limit imposed by weather-related availability of the ground laser beacon is caused primarily by the limited clear weather probability from the ground stations. Furthermore, it also imposes restrictions on ground station hand-offs and flight-ground coordination if a cooperative beacon tracking scheme is used. Atmospheric availability due to cloud coverage is a significant issue for optical communication systems.

5.3.3.3.12 Stray Light. Stray light is defined as any unwanted photon reaching the terminus of an optical system. Such photons may, among other methods, arrive at the terminus through scattering from mirror imperfections or contaminants, diffraction by the secondary mirror or its supporting structure, or through scattering from the baffles. The dominant source of stray light will be sunlight that is approximately a billion times brighter than the Earth. Even a miniscule fraction of sunlight scattered from the primary mirror or baffling will be significant.

Stray light (or any locally uniform background signal, including dark current) gives two separate types of noise. The first is the shot or photon noise, which can be treated as simply an additional photon noise source. The second is due to the non-uniform background—pattern noise—that contributes to the image error as a bias term. The bias term does not decrease with longer exposure time as does the second term, which is basically the contribution due to photon statistics. For high stray light rates, such as at a phase angle of 160 deg and say with a 5×5 centroiding region, the 1σ NEA (in pixels) is $> 10\sigma_U R_T / I_S$. When the stray light rate equals the signal rate, the non-uniformity uncertainty σ_U must be kept smaller than 0.15 percent to hold the stray-light contribution to less that 0.1 μrad, about 0.14 pixels. Since this is not a priori achievable in the detector design, this places a strong requirement to calibrate and/or measure the background in high stray-light environments. This can be done by maintaining either a calibrated pixel response map or by calibrating in real-time the local background in each pixel near the spot as the image (and stray light) moves. In summary, background calibration is required for high stray-light conditions, while for high phase angles the calibrated pixel non-uniformity is required to be held to less than 0.15 percent.

5.3.3.3.13 Radiation Considerations. There are two basic types of effects to consider. The first can be considered as a single-event upset (SEU), where a particle hits the detector or associated electronics. This produces false images, and it can cause degradation of measurement accuracy. The second, the fluorescence and Cerenkov effect, is primarily caused by high-energy electron flux passing through glass elements and resulting energy deposition, and it increases with the mean path length in the glass as well as the flux rate. The main effect expected here is increased background; this may be significant

depending on the amount and type of glass in the system. SEU radiation presents a different problem—namely, electrons or other high-energy particles depositing corrupting signal into pixels can degrade images.

5.3.3.3.14 Pointing Error Trade Sample. The magnitude and sources of errors are quite varied. These errors must be judiciously traded and managed to meet the overall pointing requirements. As a sample, a laser beacon tracking scenario is analyzed. There are various pointing error sources that can be classified into three groups (Fig. 5-30). The RSS (root- sum-squared) value of the total dynamic pointing error was allocated to meet the sub-microradian pointing requirement. The error allocation has been done using the Acquisition Tracking Link Analysis Software [56] (ATLAS) simulation tool. The simulation results are based on the projected pointing system performance such as FPA read noise, closed control loop update rates, and inertial sensor (accelerometer) noise. As indicated in Fig. 5-30, the largest error comes from S/C vibrations, which are determined by the specific S/C vibration and the disturbance rejection of the tracking control loop. The second largest error source, inertial sensor noise, is mainly determined by the given noise specifications (Honeywell QA-3000 accelerometer specifications used in this example) [57]. The centroid errors on transmit laser (NEA, pixel-to-pixel non-uniformity, spatial quantization) are relatively smaller than those of the beacon since the transmit laser power on FPA can be easily controlled to meet the requirements.

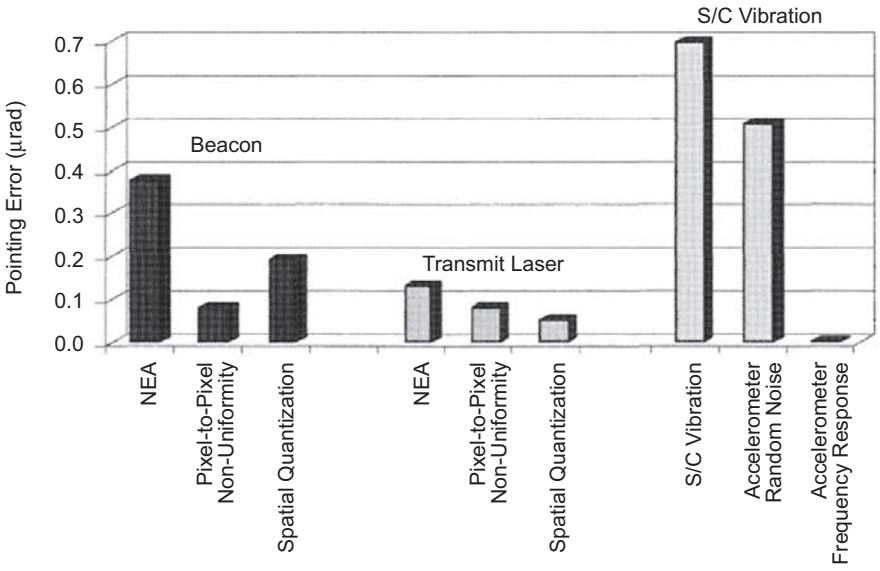

Fig. 5-30. Pointing error allocations to various error sources using simulation results.

5.3.4 Cooperative Beacon (Ground Laser) Tracking

Uplink beacon tracking is an attractive option from the implementation point of view. A laser signal presents a well-defined point spread function, and the very narrow spectral bandwidth allows easier rejection of the background-scattered sunlight. The problem with uplink beacon tracking is the amount of available power. For example, at Jupiter (6 AU range) using a 500-W uplink laser operating at 532 nm, for example, the number of photons received at the tracking detector is approximately 2.3×10^5 photons/s. Even with aggressive assumptions on the uplink power and beamwidth, the amount of available uplink power is not expected to exceed 5×10^5 photons/s. Compared with the required signal power of approximately 10,000 *detected* photons/frame, it can be seen that uplink beacon tracking alone cannot provide the tracking bandwidth required to control the pointing error [54].

Signal availability has two key limitations. The ground laser beacon transmitting station must be in direct line of sight with the spacecraft, and the weather conditions must be relatively clear to permit transmission of the optical beam.

Stray light can be reduced, using a narrowband filter. It appears that a 0.2-nm to 1.0-nm wide filter can be used, reducing the stray-light contribution. A narrowband filter is needed to filter out both the stray light from the sun and light from the Earth background. The Earth at zero-phase angle, when seen from Jupiter, has a similar intensity and spectral distribution as that of a 0th magnitude black body. Using the blackbody signal model, the Earth at 0-deg phase angle and 5-AU distance generates about 6×10^6 photons/nm/s.

By tracking an uplink beacon, the knowledge of the ground station location is essentially perfect. The difficulty is distinguishing the beacon location from the Earth background. The laser output (5×10^6 photons/s) is clearly overwhelmed—especially considering the variability of the total signal from the Earth. Even with a narrowband optical filter of 0.2-nm bandwidth, the background photon flux is still 5 times higher than the beacon signal strength. In order to perform beacon tracking, therefore, accurate calibration of the Earth background will be required. A practical limit for the beacon tracking will be at a SEP angle of 30 deg when the Earth background is of more comparable strength to the beacon uplink.

Above 90-deg phase angle, the Earth background becomes less of a problem, and beacon tracking becomes more feasible. Depending on the phase model, the Earth background is about 10–25 percent of the beacon signal strength. At very high phase angles, (>160 deg), the Earth background is (depending on the model assumed) on the order of 5×10^3 incoming photons/nm/s. Here the flux from the laser beacon is significantly larger; eliminating any image-induced bias.

At smaller phase angles, there can be sizeable centroid error from the Earth background. Given two centroid measurements—(x_L, y_L) for the beacon and (x_E, y_E) for the Earth image, with intensities B_L for the laser and B_E for the Earth (the intensities are measured in the waveband)—the centroid of the system is shifted from the uplink beacon source by an amount

$$(x_L, y_L) + (x_E - x_L, y_E - y_L)\frac{B_E}{B_L + B_E} \tag{5.3-7}$$

With an Earth image that is 20 μrad wide, the separation between the Earth and beacon centroids $(x_E - x_L, y_E - y_L)$ could be as large as 20 μrad. Considering the brightness ratio, $B_E/(B_L + B_E)$, a 1:10 ratio would cause a 2.0-μrad shift in the estimated centroid location. This is much too large an error. A 1:100 ratio is acceptable in this case, since the laser spot would be located to 0.2 μrad, approximately the error for measurement error. Because of the possible atmosphere-induced intensity fluctuations of the laser signal, and the variability of the Earth background intensity, knowledge of the intensities values for B_L and B_E could have significant errors. Additionally, the centroid location for the illuminated portion of the Earth, (x_E, y_E) is susceptible to variation in Earth intensity (albedo variation). Some of this error can be taken out by knowing the position of the laser beacon relative to the lit Earth, but there still will be residual errors.

Because of the predictability of the laser spot shape, a better centroiding algorithm (such as the maximum likelihood algorithm or some other model based algorithm) might yield better results by working on the part of the signal away from the lit limb. There are some obvious operational complications, but at last resort, if the uplink beacon could be pulsed at slow intervals, Eq. (5.3-7) could be calculated with both $B_L = 0$ (laser off) and using the laser signal. The change in brightness (if the image transmission were controlled on the Earth) could be used to determine whether the laser image was combined in the signal, or the image included the Earth only. Knowing one of the terms in Eq. (5.3-7), as well as the sum, gives a more accurate location of the point (x_L, y_L). A procedure like this could also be used as part of a calibration procedure to attempt to correct for Earth's albedo variation.

For the case where the Earth is large, but less intense than the laser spot at the relevant wavelength, the expected size in pixels of the laser spot can be used to limit the centroid window area and the contribution of the Earth image.

5.3.5 Noncooperative Beacon Tracking

Three major noncooperative beacon ATP technologies have been developed at JPL in the past decade. (These methods are also sometimes

referred to as beaconless tracking.) The distinguishing factor is the type of reference sources, namely visible Earth images, long-wavelength infrared (LWIR) Earth images, or visible stars. A visible Earth tracker was conceived as the first beaconless tracker. Although several potential solutions have been proposed for the visible Earth tracker, albedo variation was identified as the major challenge. To solve the albedo variation problem, three centroiding algorithms based on the edge detection and maximum likelihood criteria were explored. Two different approaches, LWIR Earth tracker and star tracker, were later proposed to overcome the albedo variation problem, and the analysis shows that attitude jitter of less than 150 nrad (1-sigma, single axis) can be achieved, which would meet the requirements of the current deep-space optical communication pointing system.

5.3.5.1 Earth Tracker–Visible Spectrum. Visible Earth-image tracking appears to be attractive because of its high brightness, and importantly, it does not require an uplink laser beacon (which considerably simplifies link operation). However, visible Earth-image tracking requires accurate compensation for centroid shifts (bias) due to the Earth weather-induced albedo variations. Figure 5-31 illustrates this problem. Figure 5-31(a) shows Earth images taken by the Galileo spacecraft as it receded from the Earth. The image contains intensity variation due to the presence of cloud pattern. The same image as would be seen through diffraction limited optics is shown in Fig. 5-31(b). The diffraction-limited point spread function reduces the image contrast significantly. Finally, at Europa distance, the image is only several pixels in diameter, and the detector pixel quantization lowers the image resolution, as illustrated in Fig. 5-31(c). It has been shown that achieving centroid accuracy (1-sigma) of 0.1 pixel requires that the intensity need to be known to be within 10 percent of the true value [53]. Since the average Earth

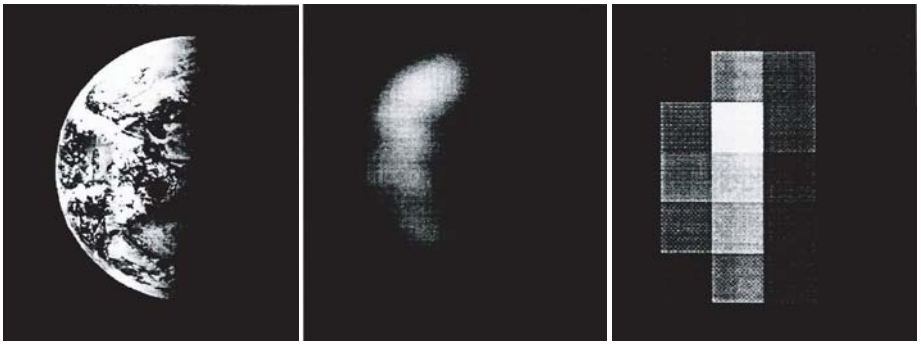

Fig. 5-31. (a) High resolution Earth image as seen by the Galileo spacecraft as it receded from Earth, (b) same image of Earth as seen through a diffraction-limited optical system. The image blurring is due to the diffraction-limited spread of the receiver optics, and (c) same image of Earth as seen through an array detector with a pixel FOV of 3.5 μrad.

albedo variation is much more than 10 percent, computing accurate centroids from the pixilated image with albedo variation presents an enormous challenge to the design.

Conceptually, the optical communication subsystem can mitigate the albedo variation problem by performing periodic imaging of the Earth image with other celestial references such as the Moon or nearby stars which have a more predictable distribution of light. Since the distance between the Earth and other celestial references are accurately known, the albedo offset of Earth can be deduced. The limiting factors in the albedo offset include the measurement error of the celestial reference sources, spacecraft jitter, and stray-light noise. For the case of using the Moon for bias compensation, the centroid measurement uncertainty increases as the mission range becomes large due to the dim Moon image. For the stars, it is independent of the mission range, and the details of analysis are presented later in the star tracker section.

The concept of the ATP system using the Earth tracker is illustrated in Fig. 5-32. First, Earth is imaged on FPA and the centroid is computed. Then, the ground position is deduced from the known distance between the geo-centroid of the Earth and the ground receiver position. The pointing vector to drive the fine-steering mirror (FSM) is the difference between the current transmit laser position and the ground receiver position with the addition of point-ahead vector to account for the two-way light travel time between the receiver and the transmitter. When the Earth image cannot provide sufficient signal for high-rate tracking, inertial sensor measurements are used to propagate the knowledge of the optical boresight at a higher rate between FPA updates.

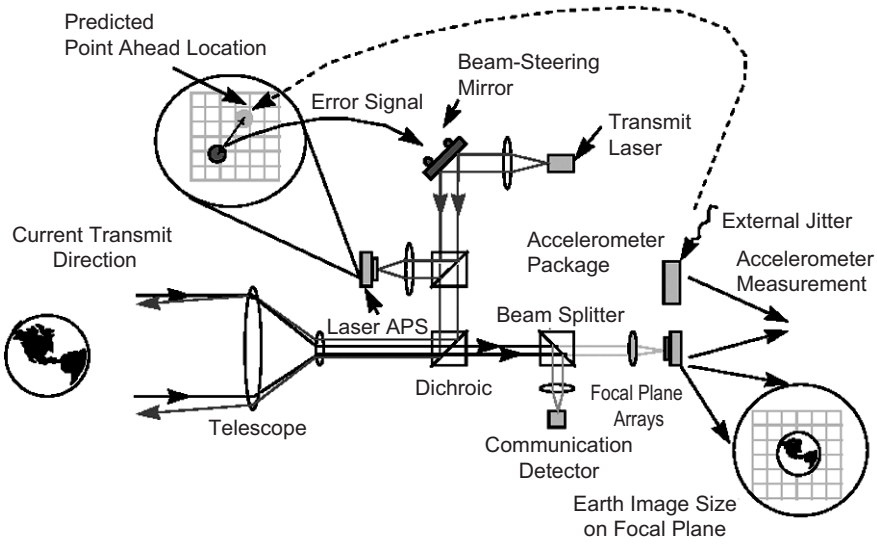

Fig. 5-32. The ATP concept using the visible Earth tracker.

Functionally, FSM jitter is measured using the reflection of the downlink laser off the FSM, while telescope jitter or S/C vibration is measured using a combination of FPA and inertial sensors.

One of the key considerations for the Earth image tracker to provide an accurate pointing is the Earth signal level and availability. The signal level affects the tracking rate, and the signal availability directly influences the communication link availability. Earth signal (reflected sunlight) has about the same spectral distribution as the Sun with most of the energy in the 400–900 nm band, which requires the tracking detector to have high spectral response for 400–900 nm. At low phase angle, an Earth image provides sufficient photons for tracking even at a 2-kHz frame rate. However, the signal from the Earth image has a wide variation, both in total and spatial distribution. The current best estimates show that the total signal follows a phase law between that of the Moon and a Lambertian sphere. There is some direct evidence the total Earth signal can be as bad as the Moon model under some weather conditions. Table 5-12 shows signal estimates versus phase angle with no optics loss, and it assumes a low quantum efficiency (Q.E.) of 25 percent, such as from a photogate (PGT) active pixel sensor (APS) design. Assuming the minimum requirement of 10,000 electrons per frame [54] and Earth at Jupiter distance, maximum frame rates of 6.2 kHz, 100 Hz, and 20 Hz are available for the phase angles of 90, 160, and 170 deg, respectively. Therefore, use of inertial sensors is required somewhere between 90 and 160 deg of phase angle. For the signal availability, it is limited by the angular separation between the Earth and the Sun, and between the Earth and the Moon. Based on conic elements, the Earth as seen from Jupiter, for example, nearly always has sufficient separation from the Moon, since the Moon's orbit is inclined to the ecliptic by about 5 deg. The angular separation between the Earth and the Sun is limited by straylight considerations, rather than overlapping images.

Other key considerations include stray light from the Sun. When the stray light rate becomes high, not only does the added photon noise cause additional centroid error, but the pixel non-uniformity also becomes much more significant and requires pixel response calibration. Two to three degrees separation is considered as the current requirement.

In the next sections, we present three centroiding methods to mitigate the albedo variation problem.

5.3.5.1.1 Maximum-Likelihood Method. The maximum likelihood method is considered to be an optimal solution if one can assume the existence of a perfect reference image. The acquisition process using this approach has been developed for the cases of rigid translation movement between the two image frames under static conditions [58,59,60]. It has been shown that the optimal spatial acquisition requires solving two nonlinear equations to estimate the coordinates of the transceiver from the received camera image in the

Table 5-12. Estimated Earth signal at Jupiter distance, assuming QE of 25 percent of photogate mode APS and 100 percent optical efficiency.

Phase Angle	Distance	Total Photons, 400–900 nm	Electrons, No Phase Law, No Optics Loss, PGT Device	Electrons, Lambertian Model, PGT Device	Electrons, Moon Model, PGT Device
90	5.2 AU	5.7×10^9	7.0×10^8	1.7×10^8	6.2×10^7
160	4.3 AU	3.9×10^9	1.0×10^9	2.8×10^7	1.0×10^6
170	4.3 AU	3.9×10^9	1.0×10^9	7.0×10^6	2.0×10^5

transformed domain when the uncertainties between the reference image and the received image are modeled as additive white Gaussian disturbances. The optimal solution can be obtained iteratively by solving two linear equations. Numerical results using a sample Sun-lit Earth as a reference image demonstrate that sub-pixel resolutions can be achieved in a high disturbance environment. Spatial resolution is quantified by Cramer-Rao lower bounds [61].

The above process was applied to acquire a Sun-lit Earth image. The image is assumed to be detected by a CCD array and corrupted by additive white Gaussian disturbances such that $(S/N)_\ell = 1$, where $(S/N)_\ell$ is the average signal to noise ratio at time t_ℓ defined by

$$\left(\frac{S}{N}\right)_\ell = \frac{1}{\sqrt{M_d N_d}} \frac{\left\|\vec{\mu}_\ell\right\|}{\sigma_\ell} \tag{5.3-8}$$

Table 5-13 lists the lower bound for the estimation variances for different sizes of CCD arrays. As an example, consider a requirement to achieve a sub-pixel resolution of 10 percent during acquisition. The corresponding σ_ℓ computed to be 16.68 for a signal-to-noise ratio of unity for a 4×4 detector array. From Table 5-13, the standard deviation of $(\hat{x}_\ell - x_\ell)$ is evaluated to 0.13 pixels. If the standard deviation is used as a measure of the resolution capability of the process in the spatial coordinate, the 4×4 detector array will not be able to meet the requirement. Following the same argument, a sub-pixel requirement of 10 percent can be achieved by using an 8×8 CCD array, which indicates that better accuracy can be achieved with higher resolution reference image.

5.3.5.1.2 Edge Detection Method. The edge detection method uses the fact that, even though the Earth albedo varies widely across the Earth surface, there

is a relatively high contrast between the solar illuminated surface and the dark space background [62]. Furthermore, since the distance between Earth and the spacecraft is known, the radius of the limb can be calculated easily. If the Earth limb can be accurately extracted from the focal plane image, the precise orientation of Earth can be derived. The receiver location can then be calculated using the spacecraft ephemeris and the relative orbital geometry. Although both maximum likelihood and edge detection methods are technically sound, in practice their performances are influenced by the varying Earth albedo, solar illumination, as well as the receiver point spread function and detector pixel quantization. The combined effects of these factors on the accuracy of extended imagery process are very difficult to analyze. On the other hand, it is necessary that the algorithms be fully characterized before the method can be proposed as a replacement for a beacon-based tracking system. A software simulator approach in which the algorithms are tested against a large number of test images was taken as the logical solution to the algorithmic verification process.

The test images were generated with realistic parameters such as the proper Sun-Earth-Probe (SEP) angle to the spacecraft, representative albedo contrasts and spatial correlation properties, the blurring due to the receiver optics point spread function, and discrete quantization due to finite CCD pixels. Figure 5-33 is the histogram of the simulation results of the maximum likelihood method. The error in estimating the image offset is normalized to the full-width half maximum of the Gaussian point spread. Note that most of the simulations resulted in a normalized error of 0.2 to 0.5 range. An improved correlation algorithm using iterative steps and nonlinear estimations was shown to provide improved results for the limited number of cases tested [62]. Further tests are needed to characterize the RMS error in estimating the image shifts.

Table 5-13. Performances of various detector array sizes.

CCD Array Size		Normalized Lower Bound	
Md	Nd	$\frac{\mathrm{var}(\dot{x}_\ell - x_\ell)}{\sigma_\ell^2}$	$\frac{\mathrm{var}(\dot{y}_\ell - y_\ell)}{\sigma_\ell^2}$
2	2	5.72×10^{-4}	3.64×10^{-4}
4	4	6.13×10^{-5}	2.61×10^{-5}
8	8	1.06×10^{-5}	2.77×10^{-6}
16	16	3.59×10^{-6}	4.39×10^{-7}
32	32	9.52×10^{-7}	7.32×10^{-8}

Because the Earth limb forms an arc of a circle, a simple curve-fitting routine can be used to derive the Earth location. When there is a high contrast between the limb and background, edge detection and curve fitting provides an accurate way of estimating the Earth centroid. When the spatial contrast is reduced, such as when excessive blurring by the receiving optics is experienced, or when the limb point is not directly illuminated by the Sun, then the edge extraction routine may have problems identifying the correct limb points. The focus of the edge-detection algorithm development was on adapting (modifying) the edge-detection method such that an accurate edge could be extracted under such conditions.

As the plots in Fig. 5-34 show, The results of the edge-detection method were more encouraging than the correlation algorithm, but they still did not quite reach the 0.1 normalized error. These results are plotted in Fig. 5-34. The results for the crescent (large SEP angle) cases show that 95 percent of the cases producing a centroid estimate below the 0.1 beam divergence. The combined results for all cases were not as good, with approximately 80 percent of the cases below the 0.1 normalized error and more than 95 percent of the cases below 0.2 normalized error.

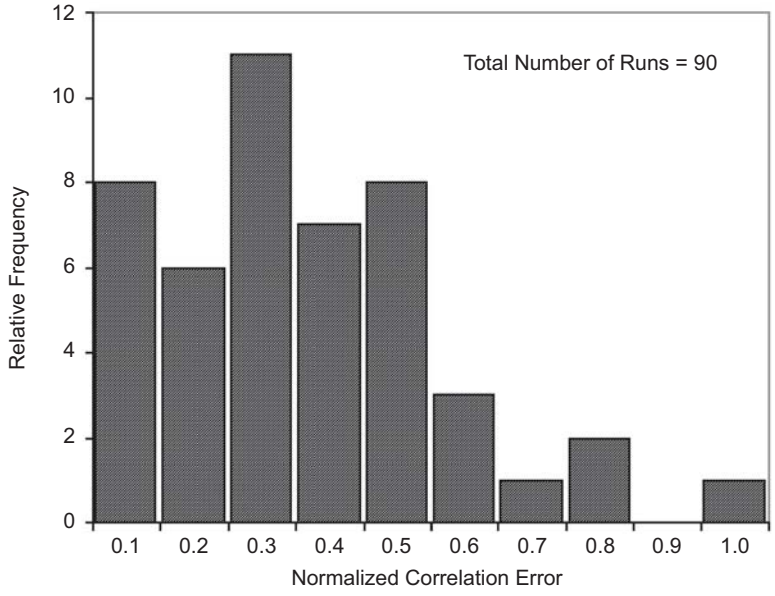

Fig. 5-33. Simulation results for the correlation tracker.

Both maximum-likelihood and edge-detection algorithms show potential for extended-source image acquisition. Initial results from the correlation algorithm do not reliably satisfy the 0.1 normalized error, but improvements in the algorithm using an iterative nonlinear estimator have shown an improved performance. Initial results from the edge-detection algorithm also do not satisfy the 0.1 normalized error, but the normalized error was steadily reduced as the algorithm was refined. For the simulated Earth images, the edge-detection method exhibits superior performance relative to the correlation algorithm. Future improvements in the correlation algorithm include better reference template generation, hard limiting the image, and addition of nonlinear estimating routines.

5.3.5.1.3 Subpixel Scanning Method. As one of the variants of the edge detection method, the concept of subpixel scanning was used [63,64]. The technique increases the resolution of the Earth image with subpixel scanning using FSM: a sequence of images is captured as the Earth image is moved across a CCD array in subpixel increments using FSM scanning. Using this high-resolution data, the algorithm then locates the geo-center of the Earth regardless of the illumination by the Sun. The algorithm relies on two parameters for its solution; cutoff frequency of the low-pass filter and a threshold used to extricate the Earth image from the background of the image. The optimal cutoff frequency of the low-pass filter is estimated using cross validation. For the threshold, a Monte Carlo simulation is used to determine the threshold that minimizes the mean squared error between the estimated and true locations of the ground-based terminal. Simulations indicate that the parameters can be determined very accurately using these methods. Numerical results of

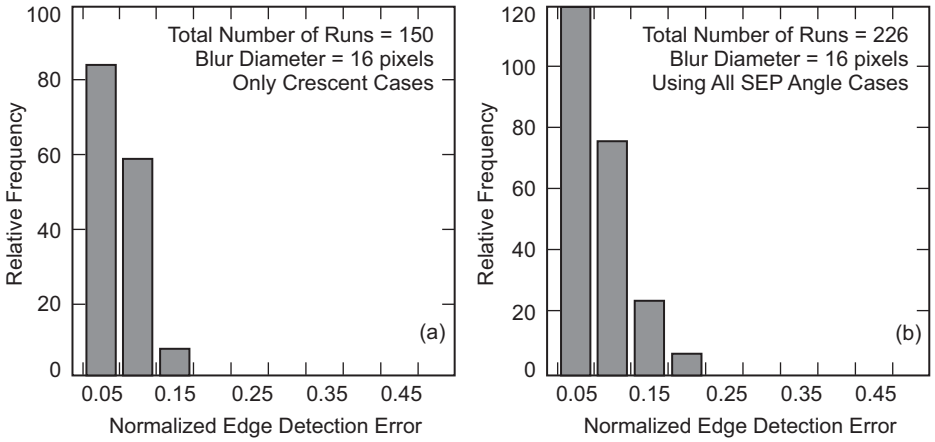

Fig. 5-34. Simulation results for the edge detection tracker for (a) large SEP angle (crescent Earth) cases and (b) for all SEP angle cases.

the acquisition algorithm, including parameter estimation, demonstrate that subpixel resolutions can be achieved regardless of the observed shape of the Earth or the presence of noise. Results on the centroid accuracy were achieved to within 1/10th and 1/20th of a pixel accuracy using partially to fully illuminated Earth images with an SNR of 1 to 20 used to test the algorithm [64].

5.3.5.2 Star Tracker. As stated earlier, the use of a star tracker for the ATP system is one of several options that can potentially solve the albedo variation problem of the visible Earth tracker [54,65]. The perceived potentials of this concept are twofold: a) range independent signal level and, b) point source that does not have an albedo-variation problem. Since the star tracker provides low-bandwidth signal, high-bandwidth gyros and angle sensors need to be combined for the high-bandwidth pointing knowledge estimation. The analysis which is presented later in Fig. 5-36, shows that pointing knowledge of 150 nrad (single axis, 1 sigma) can be achieved with an 8-cm diameter telescope aperture with assumptions of centroiding NEA of 1/25 pixel accuracy per star, Space Infrared Telescope Facility (SIRTF) class gyros (angle random walk, ARW = 0.0001 deg/root-hr), 5 Hz star trackers with ~5.0 degree FOV, detector of 1000 by 1000 pixels, and stars of roughly 9 to 9.5 magnitudes. This 150-nrad pointing knowledge is well below the typical deep-space optical communications requirements of about 300 nrad. The star coverage study shows that the average link availability is above 98 percent with a single star tracker.

The general approach is to determine both the attitude of the optical communications terminal (OCT) coordinate frame, and receiving station location in inertial space, such as relative to the J2000 coordinate frame (or the newer International Celestial Reference System (ICRS) frame), and point to a derived location in the optical communications frame. This approach is akin to that used to point science cameras on a Voyager-, Galileo-, or Cassini-type spacecraft. A specific approach to attain this attitude (or pointing) knowledge accuracy is to use a combination of high-precision star tracker measurements and high-bandwidth inertial sensor updates: gyros for medium bandwidth (< 50 Hz) and angle sensors for high bandwidth (> 50 Hz). An attitude estimator integrates this information with any additional data (such as position data from navigation (ephemeris), alignment data from in-flight calibrations, or data provided from communication with the ground) for the attitude knowledge estimation. Adding the point-ahead to the attitude knowledge to account for the two-way light time gives the pointing knowledge. The pointing knowledge is used to drive the fine-steering mirror to transmit the downlink laser beam.

5.3.5.2.1 The Pointing Knowledge Estimation Method. Star trackers are very accurate and provide accurate (absolute) pointing knowledge with typically a low update rate (depending on the star magnitude). On the other hand, inertial

sensors can provide high bandwidth (relative) pointing knowledge. Here the mathematical derivation is given on how to combine the star tracker and inertial sensor measurements to estimate the attitude of star tracker using star tracker and gyro measurements. Here we treat the attitude of star tracker equivalent to the pointing knowledge since the point-ahead, coordinate transformation from star tracker to optical communications terminal, and the receiver position do not affect the uncertainty of the final pointing knowledge. This method is based on an "averaging" technique, which mainly reduces the jitter of the pointing knowledge estimate. Angle-sensor measurements are to fill in between the two successive gyro measurements for higher update rate, and the total RMS error (or jitter) increases in a root-sum-squared (RSS) sense.

Assumptions for the pointing knowledge (attitude) jitter estimation procedure (after the initial acquisition of stars).

- A one-dimensional discrete time example is assumed. The estimation works the same way in two or three dimensions, except that it is mathematically more complex.
- The gyro is assumed to be high bandwidth and to have random noise and bias consistent with high-precision gyros. The "high bandwidth" is assumed to be high enough compared to the platform disturbances for sufficient disturbance rejection control.
- The equations shown depend primarily on the information rate, which is a measure of the SNR per unit time. Information rate is a method where, that to first order, we can compare the net effect of star trackers with different accuracies and update rates, such as noting that 100 measurements/second with $\sigma^2 = 100$ are the same as 1 measurement with accuracy $\sigma^2 = 1$ (= 100/100).
- The star tracker is at lower frequency. In this example, a tracker measurement is made at every *N* steps of the gyro. The tracker has random noise s_k with variance (assumed as a constant in this case), σ_S^2, and the star tracker measurement propagated to the correct time for inclusion in the estimate (and that the σ_S^2 includes any additional noise due to propagation, such as gyro bias contributions).
- In this example, the initial estimate of the attitude, x_0, with variance, $\sigma_{x_0}^2$, is assumed to be based on the star tracker measurement.
- The gyro angle measurement is g_k. We assume there is an estimation state (not shown) for bias, and the measurement is compensated for the estimated bias;
  - The random error (angle random walk, assumed to contain a priori uncertainty due to gyro bias) w_k, with variance σ_w^2 (degrees^2/hr)

- Bias error b_k (degrees/hour), with mean value b over the short interval in question.
- The only bias error contribution is due to the residual bias error.

- Assume uniform time spacing Δt seconds between successive gyro measurement updates, and uncorrelated error sources; with N measurements of the gyro between every star tracker update. The star tracker measurements are then $T = N\Delta t$ seconds apart.
- x_k will be the pointing estimate after k steps for the gyro.

Basic equations

To estimate the attitude of the one dimensional telescope boresight, x_k

$E[w_k] = 0$	white noise
$\theta_0 = x_0$	initial state
$\theta_{k+1} = \theta_k + (g_k + w_k)$	gyro based state equation

and the change in error which includes residual bias error,

$$e_{k+1} = e_k + w_k + \Delta t \times b_k \tag{5.3-9}$$

and the total error becomes (with bias and noise)

$$E\left[(e_{k+1})^2\right] = \Delta t\, \sigma_w^2 + (\Delta t\, b_k)^2 + E\left[(e_k)^2\right] \text{ (degrees}^2\text{)} \tag{5.3-10}$$

Then for N steps, the total error becomes

$$E\left[(e_{k+1})^2\right] = N\Delta t\, \sigma_w^2 + (N\Delta t\, b_k)^2 + E\left[(e_k)^2\right] \tag{5.3-11}$$

The variance (after taking out the mean error, $(N\Delta t\, b_k)^2$) is

$$\text{Var}[e_k + N] = \text{Var}[e_k] + N\Delta t\, \sigma_w^2 \tag{5.3-12}$$

The increase in the total error is approximately $N\Delta t\, \sigma_w^2$ (jitter) + $(N\Delta t\, b)^2$ (bias) between measurement intervals of N and $N + k$.

Without any star tracker measurements, the estimated attitude angle is

$$x_k = \theta_k, \quad \text{Var}[x_k] = \text{Var}[e_k] \tag{5.3-13}$$

After a star tracker measurement, using standard type Kalman/least squares weighting to incorporate the star tracker measurement, and with a defined by

$$a = \frac{\sigma_S^2}{\sigma_S^2 + \mathrm{Var}\left[e_k\right]} \tag{5.3-14}$$

the update is (note the superscript +) made by computing

$$x_k^+ = \left(S_k\right)\left(1 - a\right) + a \times x_k \tag{5.3-15}$$

$$\mathrm{Var}\left[x_k^+\right] = \left(1 - a\right)^2 \sigma_S^2 + a^2 \mathrm{Var}\left[e_k\right] = \frac{\mathrm{Var}\left[e_k\right]\sigma_S^2}{\sigma_S^2 + \mathrm{Var}\left[e_k\right]} \tag{5.3-16}$$

Then, for $k = 0$ and time $t = 0$, the total error variance is σ_S^2 with $T = N\Delta T$.

For $k = N$, before the next tracker update,

$$\mathrm{Var}\left[x_N\right] = \mathrm{Var}\left[x_0\right] + T\,\sigma_w^2 = \sigma_S^2 + T\,\sigma_w^2. \tag{5.3-17}$$

And the corresponding bias error is $T\,b$.

After the update with a star tracker measurement, substituting $\mathrm{Var}\left[x_N\right]$ in Eq. (5.3-17) for $\mathrm{Var}\left[e_k\right]$ in Eq. (5.3-16) gives the new variance,

$$\mathrm{Var}\left[x_N^+\right] = \frac{\sigma_S^2\left(T\,\sigma_w^2 + \sigma_S^2\right)}{2\sigma_S^2 + T\,\sigma_w^2} \tag{5.3-18}$$

For accumulated bias error, substituting $\mathrm{Var}\left[x_N\right]$ in Eq. (5.3-17) for $\mathrm{Var}\left[e_k\right]$ in denominator of Eq. (5.3-16) and $T\,b$ for $\mathrm{Var}\left[e_k\right]$ in numerator of Eq. (5.3-15) gives the new estimate,

$$\frac{\sigma_S^2\,T\,b}{2\sigma_S^2 + T\,\sigma_w^2} \tag{5.3-19}$$

The derivation process for Eq. (5.3-18) is graphically shown in Fig. 5-35.

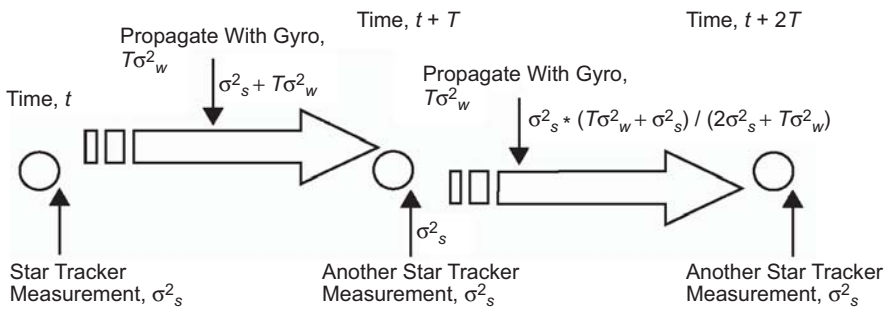

Fig. 5-35. Iterative averaging process for the pointing knowledge estimation variance.

At time, $t+T$, the new estimate is average of the star tracker measurement at time, *t*, (which has 1-sigma error of σ_S^2) propagated using gyro angle measurements (the propagated star tracker measurement taken at time *t* has a 1-sigma variance of $\sigma_S^2 + T\,\sigma_w^2$ at time $t+T$) and the new star tracker measurement at time, $t+T$ (1-sigma variance of σ_S^2). The equally weighted average of the attitude estimate with gyro propagated, x_N, and star tracker update, x_S, is

$$x_N^+ = \frac{x_N + x_S}{2}$$

Under those assumptions, the variance is

$$\begin{aligned}\mathrm{Var}\left(x_N^+\right) &= \frac{\mathrm{Var}\left(x_N\right) + \mathrm{Var}\left(x_S\right)}{4} \\ &= \frac{\sigma_S^2 + T\,\sigma_w^2 + \sigma_S^2}{4} \\ &= \frac{2\sigma_S^2 + T\,\sigma_w^2}{4}\end{aligned}$$

However, a more reasonable assumption is to give more weight to the estimate with smaller variance. One method to perform the weighted averaging is, noting that

$$
\begin{aligned}
x_N^+ &= \frac{\mathrm{Var}(x_N)x_S}{\mathrm{Var}(x_N)+\mathrm{Var}(x_S)} + \frac{\mathrm{Var}(x_S)x_N}{\mathrm{Var}(x_N)+\mathrm{Var}(x_S)} \\
&= \frac{\left(T\,\sigma_w^2+\sigma_S^2\right)x_S}{\left(T\,\sigma_w^2+2\sigma_S^2\right)} + \frac{\left(\sigma_S^2\right)x_N}{\left(T\,\sigma_w^2+2\sigma_S^2\right)}, \text{ then} \\
\mathrm{Var}\left(x_N^+\right) &= \frac{\left(T\,\sigma_w^2+\sigma_S^2\right)^2\sigma_S^2}{\left(T\,\sigma_w^2+2\sigma_S^2\right)^2} + \frac{\left(\sigma_S^2\right)^2\left(T\,\sigma_w^2+\sigma_S^2\right)}{\left(T\,\sigma_w^2+2\sigma_S^2\right)^2} \\
&= \frac{\sigma_S^2\left(T\,\sigma_w^2+\sigma_S^2\right)}{2\sigma_S^2+T\,\sigma_w^2}
\end{aligned}
\tag{5.3-20}
$$

For a more general case where the attitude estimate at time, *t*, is star tracker measurement propagated with gyro measurement, let the attitude estimate be x_u (with the corresponding 1-sigma variance σ_U^2), then the variance of x_N^+

$$
\mathrm{Var}\left[x_N^+\right] = \frac{\left(T\,\sigma_w^2+\sigma_U^2\right)^2\sigma_S^2}{\left(T\,\sigma_w^2+\sigma_U^2+\sigma_S^2\right)^2} + \frac{\left(\sigma_S^2\right)^2\left(T\,\sigma_w^2+\sigma_U^2\right)}{\left(T\,\sigma_w^2+\sigma_U^2+\sigma_S^2\right)^2} \tag{5.3-21}
$$

After additional *N* gyro measurements, the error variance grows to

$$
\mathrm{Var}\left[x_{2N}\right] = \mathrm{Var}\left[x_N^+\right] + T\,\sigma_w^2 \tag{5.3-22}
$$

Equation (5.3-21) is plotted in Fig. 5-36 for the Gyro ARW of 0.0001 deg/rt-hr and three star tracker NEAs of 0.7 μrad/frame, 1.0 μrad/frame, and 2.0 μrad/frame, respectively. Notice that the combined jitter of a star tracker and a gyro of smaller than 150 nrad can be obtained after averaging of 5 s.

The 0.7-μrad NEA can be achieved with 25 stars of visual magnitude of 9 or brighter. Centroiding NEA for each star is assumed as 1/25th pixel. 1/25th pixel NEA can be achieved with roughly 3500 e/frame using the centroid window of 5x5 pixels for a read noise of 10 e^- and 3500e/frame for a 5-Hz star tracker is feasible with 8-cm aperture with 5-deg FOV [54].

5.3.5.2.2 Star Tracker Configuration Trades. In this section, four star tracker configurations are discussed in terms of attitude estimation accuracy and star coverage. Depending on the requirements on the accuracy and the link availability, one can select among these options.

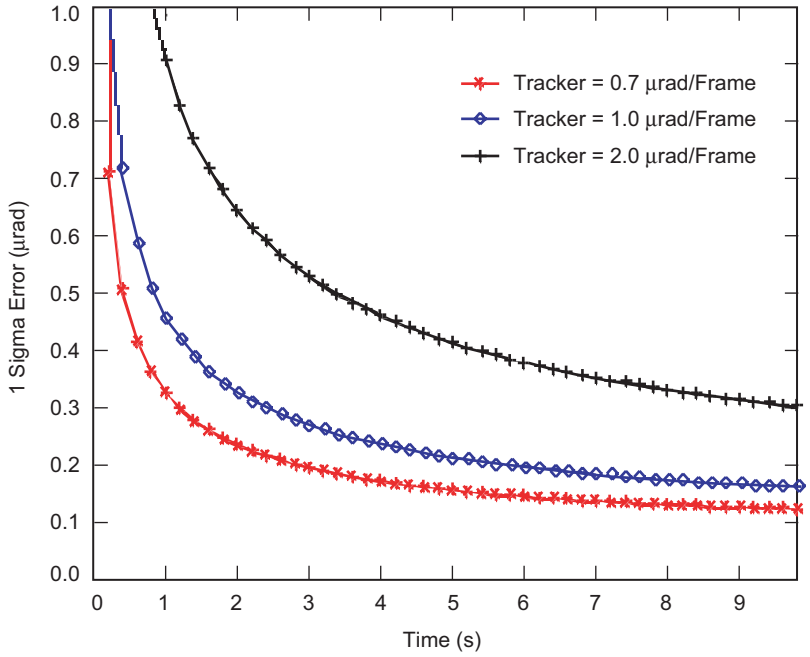

Fig. 5-36. Star tracker-gyro combined jitter as a function of integration time for the ARW = 0.0001 deg/root-hr.

The single star tracker approach (antipodal or boresighted configuration). A single star tracker gives two good attitude estimates (around the x axis and the y axis) and one poor attitude estimate (the twist around the boresight) because of the lack of star separation from the center of FOV. Typically for narrow-angle star trackers, the attitude estimates on the twist around the boresight is about 10 to 20 times worse than that of the other axes. Therefore, the star tracker orientation relative to the optical comm. terminal is critical. To take advantage of this fact, the star tracker is aligned along the telescope's optical axis either facing the Earth receiver (bore-sighted) or 180 deg away from it, facing the opposite direction (antipodal). Due to the Sun's stray light issue, antipodal is the preferred configuration. One potential issue with the single star-tracker approach is the relatively low star availability due to the limited star-search area. However, this availability heavily depends on the actual mission profile. As shown later in link availability analysis, the average sky coverage with a single star tracker can be better than 98 percent.

The two (or multi-FOV) star tracker approach (normal or gimbaled configuration). Since the boresight-twist estimation is large, a common approach is to use multiple star trackers. Some implementations use separate independent trackers. There are other designs that use mechanically integrated trackers, and others that use multiple FOVs (such as the mini-owls) on a single

detector. Another advantage of the two-star-tracker approach is the enhanced star coverage compared to the single star tracker. Table 5-14 summarizes the four configuration options with the pros and cons of each configuration.

5.3.5.2.3 Link Availability Analysis. The link availability, which directly depends on the star coverage, is one of the most critical mission parameters that affect the success of the mission. Previously, a link availability of 98 percent was assumed for a single star tracker with a FOV of 5 deg × 5 deg. The assumption on the visual magnitude of star is 9 to 9.5. The data analysis presented here is based on star position and visual magnitude data that were extracted from the Tycho II star catalog. A computer program was constructed that centered a circular FOV diameter of 3.5, 4.0, 4.5, 5.0, 5.5, and 6 deg at each point of an RA (α) and declination (δ) grid defined on the celestial sphere. The spacing of the grid was 0.1 deg in both RA and declination. For each combination of positions (α, δ), FOV size, and cutoff magnitude, the number of stars found within the FOV was computed. Finally, as a function of FOV size,

Table 5-14. Pros and cons of the four configuration options for the star-tracker-based ATP system.

Star Tracker Orientation (relative to Optical Comm Telescope)	Pros	Cons
Antipodal (single star tracker)	Looks away from Earth, more stars without Earth in FOV. Generally no Sun problems for outer planets, lower twist error contribution to pointing. Best pointing direction in the telescope direction.	Places more restrictions on mounting, requiring unrestricted viewing area, especially if mounted on the same platform as optcomm terminal. Requires accurate alignment with telescope pointing optics and need to develop calibration procedure.
Boresighted (single star tracker)	Shares channel, lower twist error contribution to pointing. Common optics relaxes alignment requirements.	Earth blocks out stars in partial field of view. Sun increases background and stray light so that long baffle may be required.
Normal (two star trackers)	Can be rotated with spacecraft for greatest star coverage field of regard.	Large error in one of LOS axes (can be reduced with two star trackers) due to large star-tracker twist error
Gimbaled (two star trackers)	Can be pointed and slewed to particular star or celestial body.	Requires gimbal mechanism, twist error about star tracker boresight may cause large pointing errors as boresight moves away from antipodal pointing. Knowledge of gimbaled position introduces additional error source.

the fraction of the sky where the specified number of stars can be obtained was computed as a function of visual magnitude. Tables 5-15 and 5-16 thus provide a snapshot for the star magnitude cutoff needed to achieve 98-percent sky coverage and predicted performance. In Table 5-15, for the given FOV and the number of stars, the star magnitude cutoff was computed such that the average sky coverage is 98 percent. In Table 5-16, the corresponding centroiding NEA was computed using the results of Table 5-15 assuming 1000 pixels across the detector and 1/25 pixel random error /star /axis attached to each measurement. The performance is reported in microradians 1σ, per axis, worst case RMS for 98 percent of the sky. For example, there are 25 stars of magnitude 9 for an FOV of 5 deg. The NEA using 25 stars is computed using the assumption of a single star NEA of $1/25^{th}$ pixel. Due to averaging of 25 centroids, the centroid NEA using 25 stars becomes

$$\text{NEA using 25 stars} = \frac{\text{NEA of single star}}{\sqrt{\text{number of stars}}}$$

$$= 85\ \mu\text{rad (pixel FOV from 5 deg and } 1000 \times 1000) \times \frac{1}{25} \times \frac{1}{\sqrt{25}}$$

$$= 0.7\ \mu\text{rad}$$

Table 5-15. Star magnitude (Mv) cutoff required to achieve 98 percent of sky coverage for various star counts and FOV sizes.

Count	FOV (deg)					
	3.5	4.0	4.5	5.0	5.5	6.0
5	8.5	8.0	8.0	8.0	7.5	7.5
10	9.0	8.5	8.5	8.5	8.0	8.0
16	9.5	9.0	9.0	8.5	8.5	8.5
25	9.5	9.5	9.5	9.0	9.0	9.0
36	10.0	10.0	9.5	9.5	9.5	9.0
49	10.5	10.0	10.0	9.5	9.5	9.5
64	11.0	10.5	10.0	10.0	10.0	9.5
81	11.0	10.5	10.5	10.0	10.0	10.0
100	11.5	11.0	10.5	10.5	10.5	10.0
121	11.5	11.0	11.0	10.5	10.5	10.5
144	11.5	11.5	11.0	11.0	10.5	10.5
169	***	11.5	11.5	11.0	11.0	10.5
200	***	***	11.5	11.5	11.0	11.0

Table 5-16. Performance estimate based on Table 5-15 and having 1:1 correspondence with Table 5-15.

Count	FOV (deg)					
	3.5	4.0	4.5	5.0	5.5	6.0
5	1.09	1.25	1.40	1.56	1.72	1.87
10	0.77	0.88	0.99	1.10	1.21	1.32
16	0.61	0.70	0.79	0.87	0.96	1.05
25	0.49	0.56	0.63	0.70	0.77	0.84
36	0.41	0.47	0.52	0.58	0.64	0.70
49	0.35	0.40	0.45	0.50	0.55	0.60
64	0.31	0.35	0.39	0.44	0.48	0.52
81	0.27	0.31	0.35	0.39	0.43	0.47
100	0.24	0.28	0.31	0.35	0.38	0.42
121	0.22	0.25	0.29	0.32	0.35	0.38
144	0.20	0.23	0.26	0.29	0.32	0.35
169	0.19	0.21	0.24	0.27	0.30	0.32
200	0.17	0.20	0.22	0.25	0.27	0.30

In summary, the star-tracker-based ATP approach can provide high accuracy on the order of 150 nrad (1-sigma, single axis) in pointing knowledge estimation with reasonable assumptions on the aperture size and star visual magnitude. The average link availability is estimated at over 98 percent using the FOV of 5 deg. As for the implementation, misalignment error between the optical communications terminal and the star tracker can be a major issue if they are not co-aligned, which may require sophisticated calibration.

5.3.5.3 Earth Tracker—Long Wavelength Infrared Band. Earth image tracking in the long wavelength infrared (LWIR) band is another option that can mitigate the albedo variation problem of the visible Earth image tracker for its low emissivity variation [66]. Low emissivity variations of thermal images is due to the relatively slow thermal changes of the Earth surfaces compared with rapid changes of reflectivity of the Earth surface for the visible wavelength.

Additionally, a full Earth image can be maintained even for high phase angles with the thermal imaging, which gives higher centroiding accuracy. The recent release from the Mars Odyssey program shows that the entire (full) Earth thermal image was successfully taken, whereas the visible-light image shows the thin crescent Earth viewed from Odyssey's perspective (Fig. 5-37, [67]). These images, taken at a distance of 3,563,735 km on April 19, 2001, as the

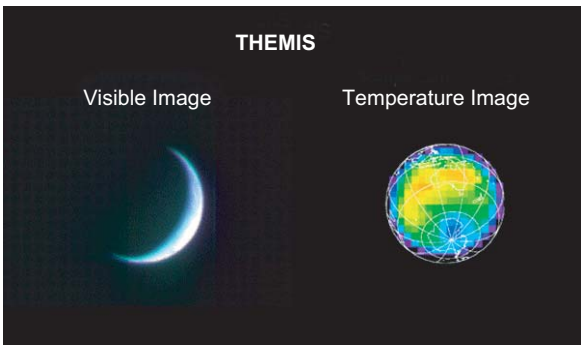

Fig. 5-37. Visible Earth image vs. thermal image.

Mars Odyssey spacecraft left Earth, support the potential of Earth thermal images in tracking/pointing applications.

5.3.5.3.1 Wavelength Selection. The advantage of using LWIR Earth images is the ability of the Earth-tracking sensor to observe energy emission from the Earth rather than reflected solar energy. To take a full advantage of steady Earth thermal emission, the optimum spectral band needs to be selected. The optimum spectral band involves a trade-off between the need for more signals to overcome the detector noise and the pointing bias introduced by thermal variations across the Earth's surface. The spectral signal variations for black bodies of different temperatures vary much more at the shorter wavelengths, so the longer wavelengths are preferred to minimize any bias error resulting from this effect. An additional advantage in the use of longer-wavelength radiation is attained from the reduction of direct solar background and solar scattering from the Earth's surface. The ability of the LWIR tracking system to generate an accurate Earth centroid value is related to the signal-to-noise ratio (SNR) in the sensor used to image the Earth. If the noise level on each pixel is not much lower than the signal value, the effect will be a shift of the final centroid value from the true value. Several different types of noise exist in detectors, and the amount of each varies from detector to detector. The aggregate noise on detectors tends to grow more slowly with integration time than does the accumulated signal, affording some potential to improve the SNR by operating the sensor at lower speeds, but this approach reduces the Earth centroid update rate.

The approach for selecting an optimum spectral band is to start at the 13-μm end of the 8- to 13-μm waveband and integrate the signal down to the spectral point at which the improvement to centroid estimation from higher signal-to-noise ratios is offset by the centroid shift inherent in the use of shorter wavelengths. The rationale for using the 8- to 13-μm waveband is its high atmospheric transmission and higher black-body radiation [68]. The available

radiance for this approach is shown in Fig. 5-38. The roll-off of the curve at shorter wavelengths further demonstrates the lack of value in extending the spectral band to shorter wavelengths. At shorter wavelengths, the variation of the radiance is larger over the entire phase angle. This radiance variation directly affects centroid bias. Based on this result, three spectral bands were selected for comparison. The 3- to 5-μm transmission window of Earth was evaluated and appears to be a rather poor choice. Only a very small fraction of the thermal energy is emitted in this band, and because of the short wavelengths, that means even fewer photons. Additionally, the blackbody response also shows that the background from scattered solar radiation will be much, much higher than would be found around 10 μm. Finally, since Rayleigh photon scattering is proportional to λ^{-3}, there will be over 20 times more Rayleigh background in the 3- to 5-μm band than around 10 μm. The 10- to 13-μm band looks quite good. There is a strong signal integrated over a full 3-μm band. Increasing the width of the band to 8–13 μm increases the signal strength by about 2 dB, according to this model. However, the model does not take into account the strong atmospheric absorption of the CO_2 band that reduces the signal gain rather significantly. Also, there is more diurnal variation in the 8- to 13-μm signal and, consequently, more spectral shift of the Earth centroid. Finally, for the 8- to 13-μm waveband, there is about 25 percent more solar-induced background than there is in the 10- to 13-μm waveband, resulting in a much greater reduction in the background level than in the signal level by limiting the band.

In summary, the 8–13-μm band was selected as the optimum band after several trades, and the subsequent analysis is based on this band.

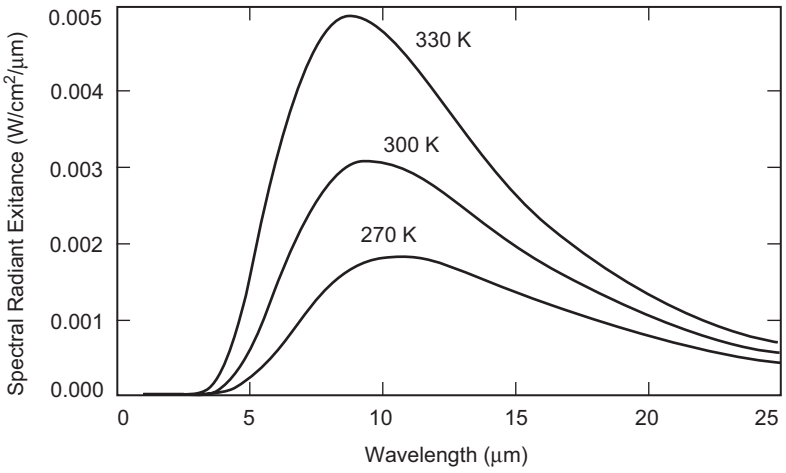

Fig. 5-38. Spectral radiance as a function of waveform for three temperatures: 270 K, 300 K, and 330 K.

5.3.5.3.2 Estimated Signal Level. A simple computer model was generated to estimate the effects of thermal variations across the surface of the Earth. The model calculates a very crude surface temperature profile based on expected diurnal, seasonal, and latitudinal variations. The model generates smoothly varying temperature profiles, without the steep gradients expected from weather patterns or surface topography. To obtain an available signal level, the model integrates the spectral radiance in the specified waveband for a selection of spatial points across the visible Earth surface. Multiplying by the known area of the Earth's surface yielded the radiant intensity of the Earth (photons/s/sr) (Fig. 5-39). Since the temperature of the visible portion of the Earth varies by season and by aspect angle (Sun–Earth–probe (SEP) angle), these values were plotted in Fig. 5-40 as a function of hour (of local time) and for solstice versus equinox.

5.3.5.3.3 Centroid Jitter Estimate. The photon radiant intensity values in Fig. 5-39, with the assumed parameter values in Table 5-17, were used to estimate the centroid jitter or noise equivalent angle (NEA). For simplicity, the center of brightness centroid is discussed here. Since the Earth image is a relatively uniform disk, it is assumed that each pixel in the sum experiences the same noise due to sensor-plus-signal photon statistics. All quantities are assumed to be measured in electrons. *DT* is the integration time used for dark current noise, and *DC* is the dark current rate in electrons/second. The basic center-of-brightness centroiding formula for a uniform signal (pixel value $D_{i,j}$ after background compensation) with a variance formula (assuming very large total signal, *T*, to take it outside the expectation) given by variance S_x (S_y is similarly computed) is approximately given by

$$\left.\begin{aligned} T &= \sum_{j=1}^{M}\sum_{i=1}^{N} D_{i,j} \\ S_x &= \sum_{j=1}^{M}\sum_{i=1}^{N} i \times D_{i,j} \\ S_y &= \sum_{j=1}^{M}\sum_{i=1}^{N} j \times D_{i,j} \end{aligned}\right\} \qquad (5.3\text{-}23)$$

Then

$$\left.\begin{aligned} x_e &= \frac{S_x}{T} \\ y_e &= \frac{S_y}{T} \end{aligned}\right\} \qquad (5.3\text{-}24)$$

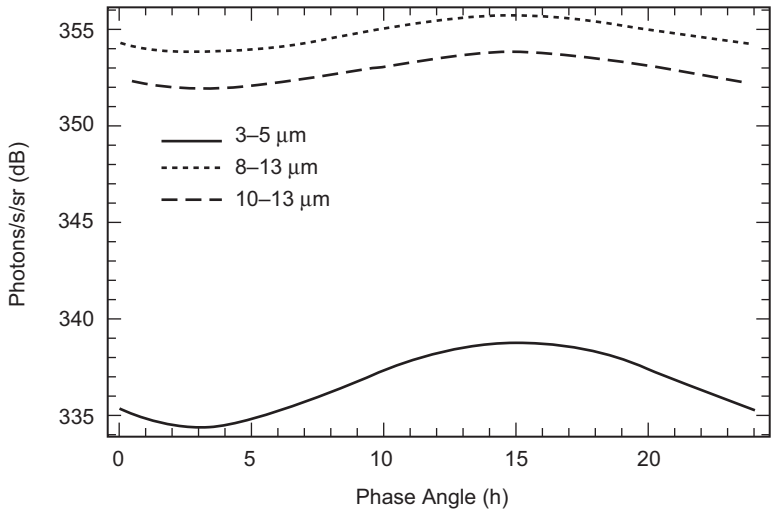

Fig. 5-39. Spectral signal for three wavelength bands.

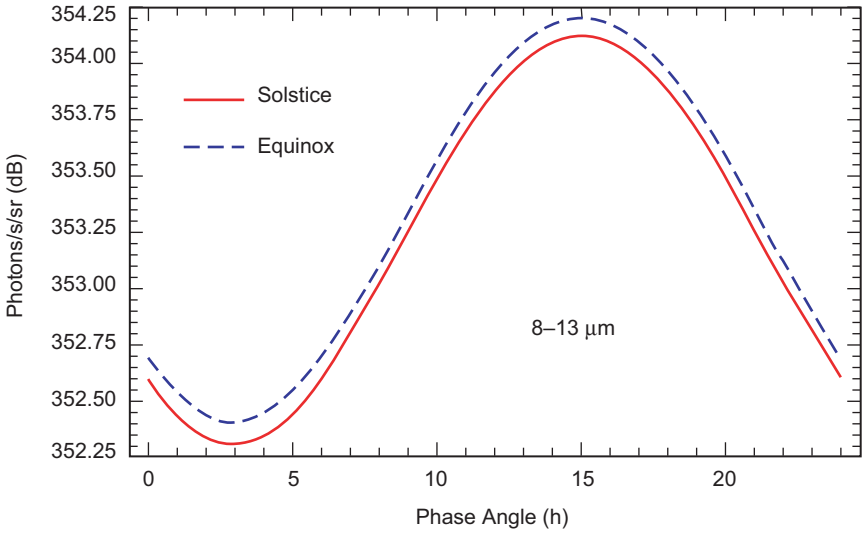

Fig. 5-40. Earth thermal signal level for solstice vs. equinox.

Table 5-17. Assumptions for NEA estimations.[a]

Parameter	Value	Rationale
Centroid window size	9 × 9 pixels to 25 × 25 pixels	Earth image of 60–220 μrad, 10 μrad/pixel, extra 3 pixels
Focal plane array (FPA) full well	20×10^6 to 30×10^6 electrons	Specification of DRS Technologies IR FPA of 25- to 40-μm pixels
ADC effective bits	14 bits	14 bits
System noise (1 sigma)	200 electrons	Read noise + electronic noise + background noise
Frame update rate	10 Hz to 1 kHz	10 Hz (inertial sensor assisted) to 1 kHz (optical only)
Aperture size	10 cm to 30 cm	Previous baseline for optical communication for deep space
Range	0.5 AU to 2.7 AU	0.5 AU to 2.7 AU (Mars missions)
Optical transmission efficiency + detector QE	10 percent	Detector QE of 80 percent and optical transmission of 13 percent

[a]Underlined values were used for the simulations presented in Figs. 5-41 and 5-42.

$$\left.\begin{aligned}\mathrm{Var}(S_x) &= \frac{N}{2} \times \frac{N/2+1}{3} \times \frac{T + N \times M \times (\mathrm{Var}(\mathrm{Read\ Noise}e) + DT(DCe))}{T^2} \\ \mathrm{Var}(S_y) &= \frac{N}{2} \times \frac{N/2+1}{3} \times \frac{T + N \times M \times (\mathrm{Var}(\mathrm{Read\ Noise}e) + DT(DCe))}{T^2}\end{aligned}\right\} \quad (5.3\text{-}25)$$

Assuming $N = M$, and that the dark current noise is negligible, the variance simplifies to

$$\frac{N}{2} \times \frac{N/2+1}{3} \times \frac{T + N^2(\mathrm{Var}(\mathrm{Read\ Noise}e))}{T^2}$$

There are two classes of parameters: one consists of design values such as aperture size and detector full well; the other is mission-dependent parameters such as range and centroid window size (governed by beacon spot size). Consider the two tracking scenarios, optical-only tracking and inertial-sensor-assisted tracking. The beacon update rates of 10 and 1 kHz were used, respectively. For inertial-sensor-assisted tracking, the NEA is very small—on the order of 10 nrad (10 μrad/pixel) for 8- to 13-μm bands (Fig. 5-41). For the

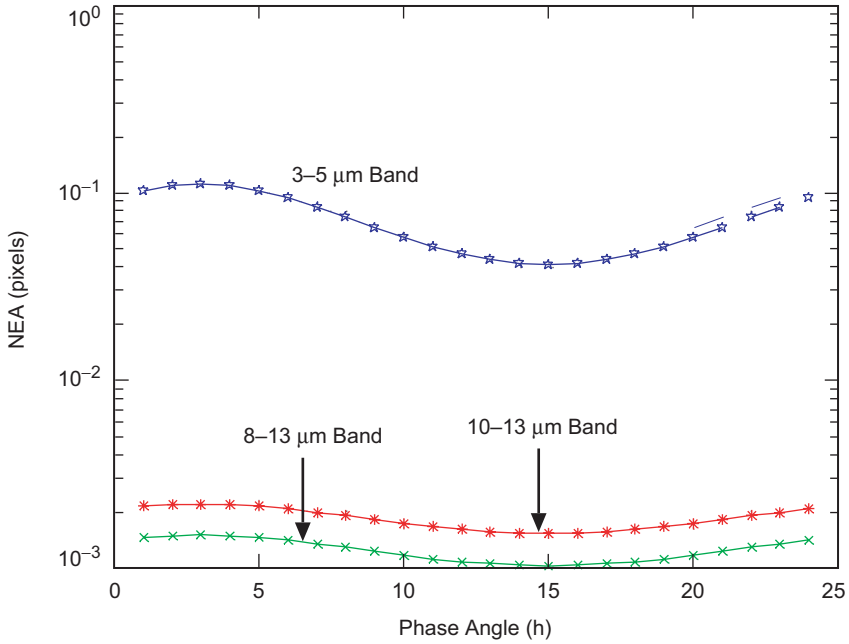

Fig. 5-41. NEA for inertial-sensor-assisted tracking update rate (10 Hz) using the worst-case scenario outlined in Table 5-17.

3- to 5-µm band, the NEA is up to 1 µrad, and with trade-offs on the detector full well and aperture size, this can be reduced to 70 nrad. For optical tracking only, the worst-case estimate of the NEA is more than 1 µrad. However, an NEA of better than 100 nrad can be achieved with the trade-offs on the smaller detector full well and larger aperture size (Fig. 5-42).

5.3.5.3.4 Centroid Bias Error Estimate. For bias estimation, the edge-detection-based centroiding can take full advantage of the Earth thermal image with all the edge pixels detected. An estimate of the bias error can be derived based on the single-edge pixel detection error and the number of edge pixels. The key concept is that the bias error decreases as more edge pixels are averaged to obtain the centroids. A *d*-pixel-diameter image will have a πd pixel edge length; for each axis, the accuracy will range, depending effectively on the half of the total number of edge pixels, $\pi d/2$ (using the side of square pixel) to $(\pi d/2)/\sqrt{2}$ (using the diagonal of a square pixel) edge pixels, where the majority of the information for a particular axis comes from edges with intensity gradients with large components in that axial direction. This gives an expected rms accuracy of

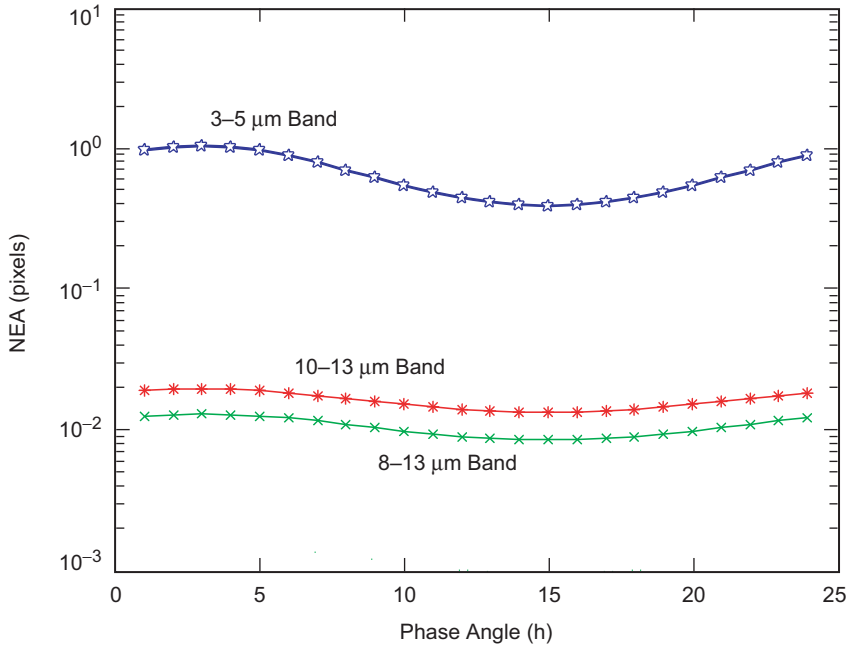

Fig. 5-42. NEA for optical tracking update rate (1 kHz).

$$\frac{\sigma}{\sqrt{\frac{\pi d}{2}}} \text{ to } \frac{\sigma}{\sqrt{\frac{\pi d}{2\sqrt{2}}}} \text{ pixel} \qquad (5.3\text{-}26)$$

where σ is the 1-sigma bias error in edge detection.

Assuming 10-μrad pixels and the range of 2.7 AU, the above estimation gives about 400- to 474-nrad bias error (1 sigma) with $\sigma = 0.1$ pixel. Bias terms arise because of non-uniformity of the surface emission near the edge of the Earth and spatial quantization (sampling) of the thermal image. To reduce the bias error, the number of edge pixels needs to be increased with smaller pixel FOV, as the Eq. (5.3-26) indicates.

In summary, the analysis on LWIR Earth image trackers indicates that the pointing knowledge jitter of less than 150 nrad for update rate of 1 kHz assuming the range of 2.7 AU is feasible. For larger ranges, the update rate decreases for the equal pointing-knowledge jitter. For example, the signal will be 100 times dimmer at 27 AU. If the update rate is reduced to 10 Hz, then the integrated total signal would be identical by integrating 100 times longer time. In this respect, the performance of the LWIR Earth image tracker is equivalent to that of star tracker for the Solar System range. For the bias error, the star tracker is independent of the range while the LWIR Earth image tracker

depends on the Earth size on the FOV of the FPA such that the pixel FOV needs to be specifically designed to meet the bias error requirement.

5.3.6 ATP Technology Demonstrations

5.3.6.1 Reduced Complexity ATP Architecture. A CCD-based spatial acquisition, tracking, and pointing subsystem architecture has been developed to perform both spatial acquisition and tracking functions for a lasercom terminal [69]. The focal plane array detector can achieve both the wide field of view required for spatial acquisition and the high update rate needed for effective platform jitter compensation by operating the CCD in the "windowed" read mode. Furthermore, this spatial tracking subsystem based on the CCD tracker requires only one steering mirror to perform both line-of-sight stabilization and point-ahead functions, and to provide means to optically close the point-ahead control loop without additional sensors. When incorporated into the lasercom system designs, the array tracking concept leads to a reduced complexity system and hence a lower system cost.

Previous designs of lasercom systems generally achieved the desired pointing accuracy by using a directionally sensitive detector (such as a quadrant avalanche photodiode) to measure the angular error between the detector line-of-sight and the beacon direction [70,71]. The error was then fed back to a high-bandwidth steering mirror to stabilize the detector line-of-sight along the beacon direction. A second point-ahead mirror in the transmit beam path was then used to provide the required pointing offset between the transmit and receive signals. Since the quadrant detector had a limited FOV, a separate, larger format detector was usually required to provide the wide field of view coverage during the acquisition process. Furthermore, in order to properly relay the optical signals between the steering mirrors and the detector focal planes, additional optical relay elements were required that further increased the system complexity. However, with the advances in array detector technology, conceptual simplification of the lasercom tracking and acquisition subsystem can be achieved without sacrificing the system performance. This is because a pixilated detector can provide wider FOV coverage, thus simplifying the spatial acquisition process. A wide-FOV system can also permit tracking of the receiver beacon off axis, thus permitting the system to be implemented with only one steering mirror.

A conceptual block diagram of the array-based tracking system is shown in Fig. 5-43. A remote beacon laser is imaged by the telescope optics onto the focal plane array. By reading out the area of the detector containing the beacon signal and calculating the image centroid, the angular direction of the beacon can be accurately deduced relative to the optical axis of the system. A small amount of the transmit signal can also be imaged onto the acquisition detector and the location of the transmit signal can be measured relative to the optical

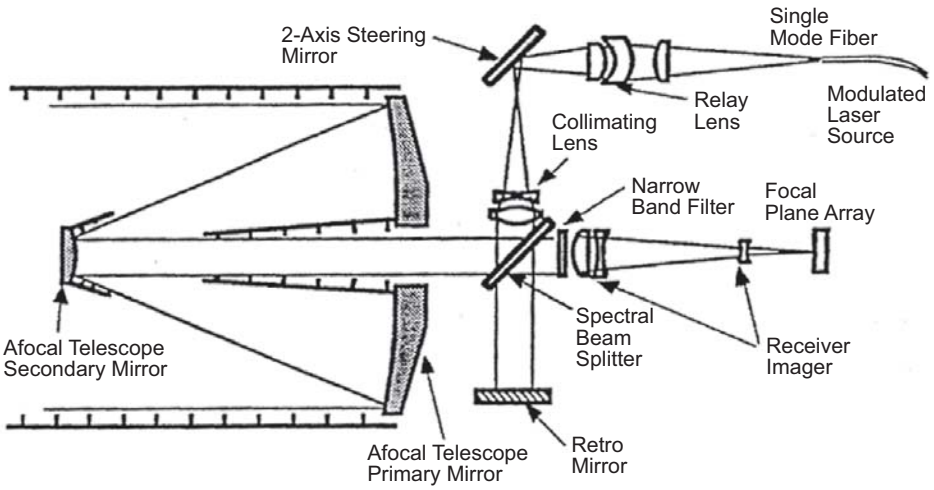

Fig. 5-43. Reduced complexity two-spot spatial tracking using a single focal plane array detector.

axis. The distance between the two image spots in the focal plane is a direct measure of the relative angular offset between the transmit and beacon signals. By sensing any difference between this measured, instantaneous point-ahead angle and the desired point-ahead value, the instrument can derive a real-time control signal to maintain pointing of the transmit signal. The subsequent beam-steering control can be achieved using a tandem of high-bandwidth steering mirror and wide-dynamic-range spacecraft. Large amplitude disturbances (such as the dead-band cycle of the spacecraft) are first removed using spacecraft attitude control. A fast steering mirror in the optical path is then used to compensate for the high-frequency, small-amplitude disturbances (micro-vibrations). The spacecraft removes the bias and maintains the steering mirror at the middle of its dynamic range. During the initial acquisition, the spacecraft is also used to orient the instrument line of sight for acquisition.

Shown in Fig. 5-44 is a block diagram of the two-spot tracking control loop. The detector images both the beacon signal and a portion of the transmit signal. The output digital data are then relayed to a control processor, which computes the positions of the image centroids and hence the instantaneous point-ahead angle. This point-ahead angle is then compared to a reference point-ahead angle, and the difference is fed into a compensation filter, which calculates the control needed for the fine-steering mirror. At the same time, the position of the beacon signal is fed to the gimbal control circuit, which stabilizes the position of the gimbal spot on the focal plane.

This simplified ATP architecture was implemented and demonstrated in the Optical Communication Demonstrator [72], which was verified in laboratory [73] and field experiments [74]. It was also implemented (in its second

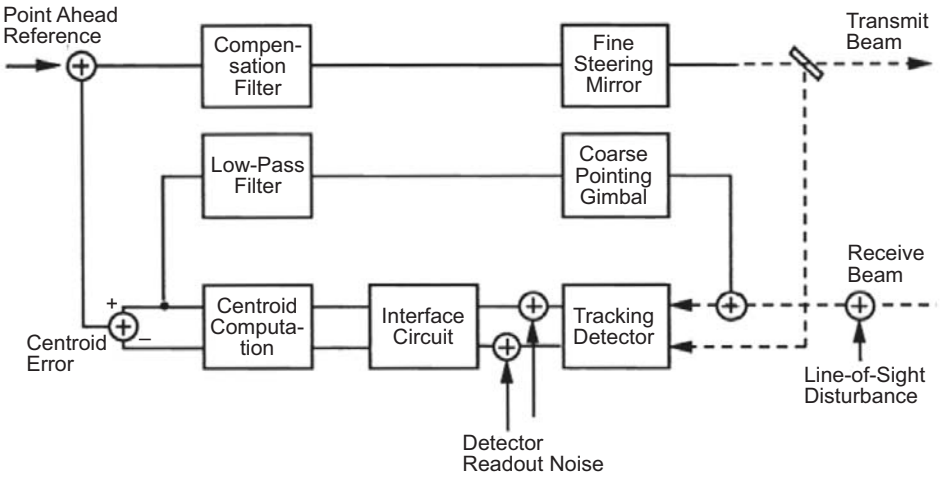

Fig. 5-44. Block diagram of a CCD-based tracking-control loop.

generation) for an Altair unmanned aerial vehicle (UAV)-to-ground 2.5 gigabits per second (Gbps) optical communications experiment as the optical communication terminal [75,76].

5.3.6.2 Centroiding Algorithms—Spot Model Method. Accurate centroid estimation is critical for free-space optical communications where the number of photons from the reference optical sources (such as stars or an uplink beacon) is limited. It is known that the centroid accuracy is proportional to the SNR. The presence of various noise sources during the exposure of the CCD can lead to significant degradation of the centroid estimation. The noise sources include CCD read noise, background light, stray light, and CCD-processing electronics. One of the most widely used methods to reduce the effects of the noise and background bias is the thresholding method, which subtracts a fixed threshold from the centroid window before centroid computation. An improved centroiding method that utilizes the spot model to derive the signal boundary (which is used to truncate the noise outside the signal boundary) has been developed and is presented in this section [77]. This process effectively reduces both the bias and the noise. The effectiveness of the proposed method is demonstrated through simulations.

Accurate centroid estimation is a critical task for a beacon-based pointing system. Past studies have shown that the centroid error (random and bias error) for deep space optical communications needs to be less than 1/20th of a pixel, whereas the total pointing error allowed (1 sigma) is 1/15th of a pixel [78.79]. Two types of centroid errors, random and bias, are affected by various sources. A random error is caused by noises, such as CCD read noise, shot noise, dark

current, and ADC quantization noise. A bias error occurs when non-uniform background light, such as stray light and Earth background image, exists.

Conventional methods to reduce the noise and bias include thresholding and centroiding of the normalized zero-crossings [80,81]. For the thresholding method, an estimated threshold is subtracted from the centroid window, which equivalently performs a bias subtraction and eliminates the noise. This method can be effective when the threshold value eliminates most of the bias and the noise. However, a simple threshold, in general, is not effective since the threshold value is dependent on the brightness of the image, and the number of pixels forming the object may be altered by the thresholding process. To avoid this problem, the use of zero-crossings for centroid estimation was proposed [81]. The limitation of that approach is the assumption of equal weighting on every pixel.

For the same objective of reducing the effects of noise, there were suggestions to use only nine pixels around the signal peak [82,83,84]. This truncation can simplify the centroid calculation without affecting the centroid accuracy if the signal is limited to this small local region. As was indicated in [85], however, the truncation of the wide signal considerably affects the accuracy of centroid estimation. Therefore, the number of pixels used in centroid estimations needs to be carefully selected so as not to sacrifice the centroid accuracy.

In this section, we develop the use of a spot model to determine which pixels are used for centroid estimation. A spot model can be constructed from the characterization of the optical system point spread function (PSF). On the centroid window, which is usually several pixels larger than the beacon spot size to allow beacon motion, the approximate signal boundary of a beam spot can be estimated from the spot model and the measured noise level. Once the boundary is identified, the pixels to the outside of the signal boundary can be set to zero, effectively eliminating all the noise and bias outside the beam spot.

5.3.6.2.1 Effects of Noise and Bias on Centroiding Accuracy. The equations for centroids (centers of brightness) for spots on a CCD-type focal plane arrays are well known [79]:

$$C_x = \sum_i ip_{ij} / \sum_{ij} p_{ij}, \quad C_y = \sum_j jp_{ij} / \sum_{ij} p_{ij} \tag{5.3-27}$$

where i and j are the x and y axis coordinates, and p_{ij} is the output of the (i, j)th pixel value of CCD. From Eq. 5.3-28, it is clear that the noise or bias closer to the edges of the centroid window dominates the centroid error due to the larger weighting factor as coordinates increase toward the edges. This is one of the

most important motivations that led to the development of the spot model method.

The equation for the random centroid error (or NEA, noise equivalent angle) is summarized as follows,

$$NEA = \sqrt{\frac{S + N_P(\mathrm{Var}(R_F) + \Delta t\, R_T}{\frac{S_2 N(N+1)}{3}}} \tag{5.3-28}$$

where S = total signal.

Δt = the exposure time.

N = truncated half width of centroiding area.

N_P = number of pixels involved in the centroiding area, $N_P = (2N+1)^2$

R_F = fixed per-pixel noise (1σ), such as read noise.

R_T = per-pixel background signal (including straylight and dark current).

Equation (5.3-28) indicates that NEA is inversely proportional to SNR. Therefore, either the signal needs to be increased, or the noise needs to be decreased in order to reduce the NEA. This implies that the effect of the noise is small if the signal is relatively larger than the noise and vice versa. To illustrate this, let us take an example where the spot signal is low. For deep-space optical communications that may require stars as a beacon source, the minimum signal available from an 11th-magnitude star with a 30-cm telescope is 10,000 photons (with 25-percent system efficiency). Assuming a CCD QE of 0.5, this translates to 5000 electrons. In this example, the reduction of the centroid window size improves the centroid accuracy significantly if it does not truncate the signal notably. Response of the NEA versus the number of pixels used in the centroid estimation is shown in Fig. 5-45. The assumptions are (1) the same fixed per pixel noise ranging from 5 e^- to 20 e^- and (2) no background signal. Figure 5-45 shows that NEA increases more rapidly with larger fixed per-pixel noise as the number of pixels (used in centroid estimation) increases.

Bias error is caused by non-uniform signal distribution, which includes stray light and background image. This corresponds to the cases where the telescope is pointing toward the Earth or close to the Sun. Even if background subtraction were applied, there would be some bias left, especially if the threshold is below the maximum of the background signal. As Fig. 5-46 shows, even 0.1 percent of the peak spot value as the maximum bias value can cause considerable bias error if the centroid window size is large, such as 9 × 9 pixels as in this example.

5.3.6.2.2 Comparison of Algorithm Performance. To demonstrate the effectiveness and robustness of the model-based noise reduction method in centroid estimation, three cases were investigated. First, three centroiding

algorithms (including model-based) were compared at various noise levels given a total signal equivalent of 5000 e^-. Second, the bias error resulting from the three centroiding methods was compared. And last, three scenarios of using incorrect spot models were used. Incorrect models at 0.1 pixels, 0.2 pixels, and 0.3 pixels were used to show the robustness of the model-based method.

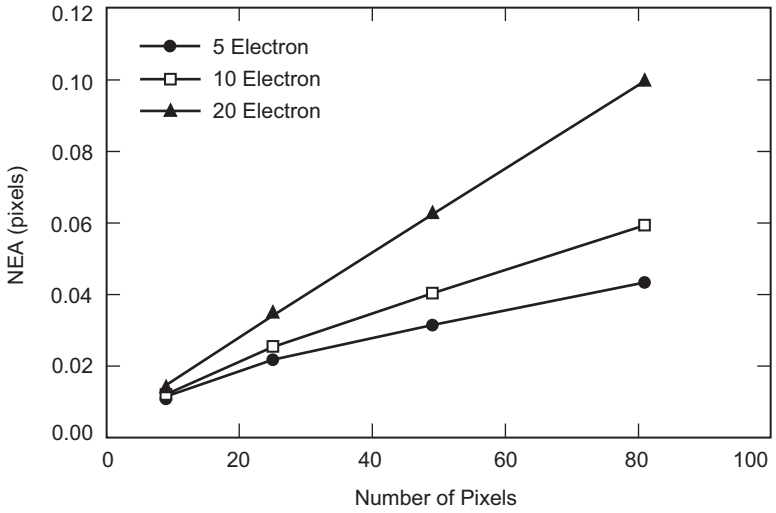

Fig. 5-45. Effect of the number of pixels used in centroid estimation. NEA increases as the number of pixels increases and more rapidly with larger noise level.

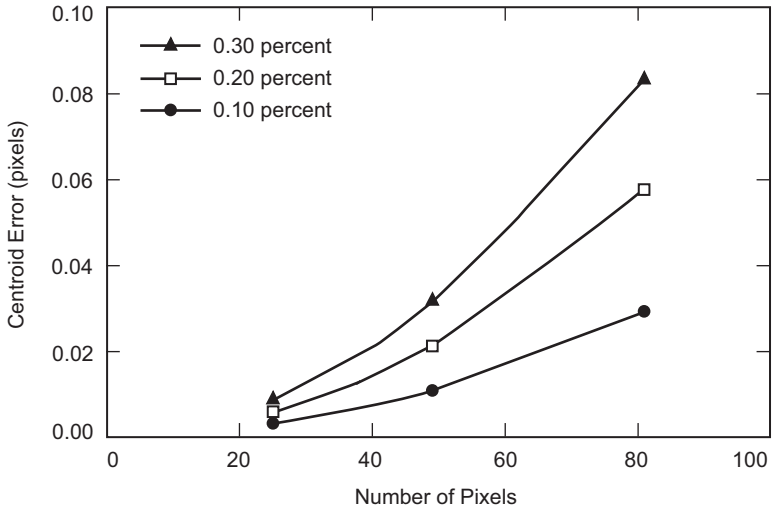

Fig. 5-46. Bias centroid error vs. the number of pixels used in centroid estimations at bias values from 0.1 percent to 0.3 percent of the peak pixel value.

Three algorithms were run 100 times for a fixed-noise value, and the noise was increased from 10 e^- equivalent to 100 e^- equivalent (Gaussian noise with 1 sigma value from 10 e^- to 100 e^- equivalent). The 1-sigma error and mean error were computed and plotted in Fig. 5-47. As is shown, the model-based algorithm outperforms the other two methods. The strength of the model-based method is not only the much smaller centroid error but also its insensitivity to the noise, as demonstrated in both plots. As the noise increases, the centroid error from the standard and thresholding methods also increases. However, the model-based method exhibits a nearly constant error.

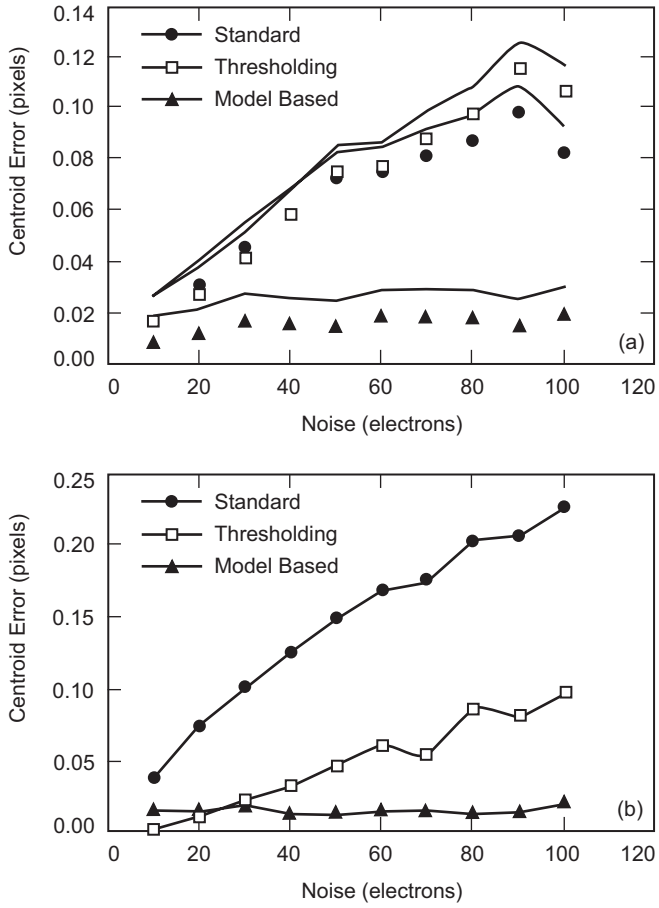

Fig. 5-47. Comparison of three centroid methods: standard centroid, thresholding method, and model based method. Plots show the centroid error vs. fixed per pixel noise (equivalent to electrons based on total signal of 5000 electrons): (a) 1 sigma random error and (b) mean error.

5.3.6.2.3 Bias Error. The effect of a bias in the spot image using the three centroid methods was also compared. As was evident in Eq. (5.3-27) above, even the model-based method would be affected by the presence of the background bias unless complete removal of the bias is conducted. The bias value was selected based on the peak pixel value that is 28.5 percent of the total signal. Maximum bias was varied from 0.1 percent to 1 percent of the peak pixel value. Figure 5-48 shows the results. As expected, the model-based method outperforms the other two methods, which exhibit a linear relationship between the bias value and the centroid error.

A method based on the spot model was proposed to improve centroid estimates of a point source image. The method assumes the spot model can be used to truncate noise and bias in the measured spot, thereby improving centroid estimates. Simulations were performed to demonstrate the effectiveness of the proposed method for noise and bias. Compared with the standard centroiding and the more advanced thresholding method, the model-based method was found to be superior in accuracy. From the simulations where the incorrect spot models were intentionally used, the effect on its performance was minimal, especially at high noise levels. Since this method was intended for low SNR signal, it could prove to be essential for deep-space missions, where a strong optical signal is not readily available. Notice that both the 1 sigma and mean errors are in the neighborhood of 1/50th of a pixel.

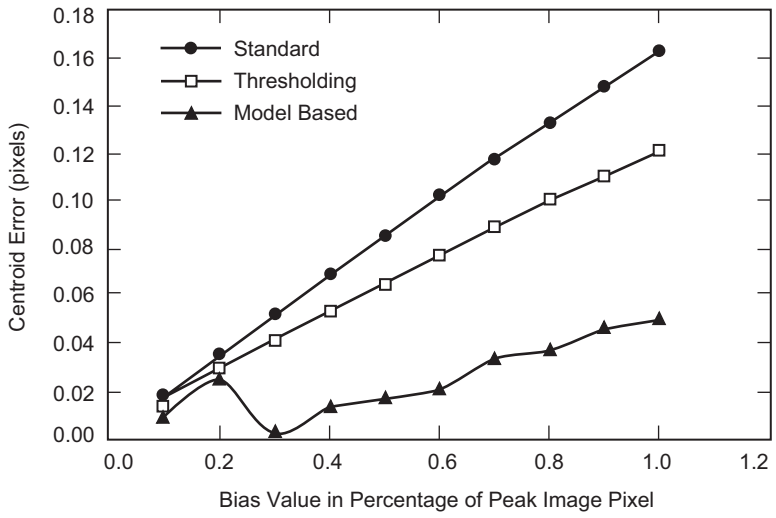

Fig. 5-48. Bias was added to the spot image, and the three centroid methods were applied. Bias values increased from 0.1 to 1 percent of peak pixel value of the spot image. The model based method has a noticeably smaller bias error contribution.

5.3.6.3 High Bandwidth, Windowing, CCD-Based Camera. In this section, we describe the functionality, architecture, and control methodology of a random-access, real-time, event driven (RARE) camera [86] as part of a real-time target acquisition and tracking platform. The camera implementation uses a Texas Instruments TC237 charge-coupled device (CCD) focal-plane array (FPA) and two TLV987 signal processors [87]. Control of the imager and signal processors is via custom logic in a field-programmable gate array (FPGA) that accepts user commands and provides region-of-interest pixel data to a host tracking processor. A message-passing paradigm is used to provide real-time imager control without knowledge of detailed imager operation.

Commercially available CCD cameras are not designed for a combination of single frame and high-speed streaming digital video with real-time control of size and location of multiple regions-of-interest (ROIs). To achieve low-level camera control with high-level system operation, a message-passing paradigm is defined. This functionality is achieved by asynchronously sending messages to the camera for event-driven operation, where an event is defined as image capture or pixel readout of a ROI, without knowledge of detailed in-camera timing. This methodology provides a RARE camera for adaptive camera control, and it is well suited for target-tracking applications requiring autonomous control of multiple ROIs. This methodology additionally provides for reduced ROI readout time and higher frame rates as compared to a predecessor architecture [88] by avoiding external control intervention during the ROI readout process.

5.3.6.3.1 Camera Requirements. The primary motivation for this camera development is to realize an adaptive sensor mechanism as part of a platform for real-time autonomous acquisition and tracking applications [89]. Such a platform requires both a sensor and a control philosophy that provides real-time adaptation of the sensor based on target characteristics and dynamics and environmental conditions. The requirements for the sensor in a deep-space application are generally for a low-noise, high-QE, high fill factor, large-format device. These requirements are currently best met by CCDs. To achieve this tracking goal requires a camera capable of frame rates of several hundred to several thousand frames per second with operating parameters that can be adjusted on a per-frame basis. High frame rates with adaptive imager control are achieved with a conventional CCD by reading out only the pixel regions of interest and discarding all other pixels. This mode of operation required the development of a customized local controller for the CCD imager to provide a tightly coupled mechanism for imager operation. Configuration of the controller is handled by a host tracking processor that loads initialization and tracking parameters into the controller to define imager operation. The initialization parameters are needed for defining the start-up mode of the controller, and the tracking parameters define detailed operation of the imager

during acquisition and tracking operations. A previous release of the camera used software control of low-level CCD operations as a first implementation but required tight coupling of the camera with the host tracking processor. That release of the camera was discussed previously [86]. Release 2.0 represents the current state of the RARE camera development.

5.3.6.3.2 Hardware Architecture. Release 2.0 is used as part of a real-time target-tracking apparatus for free-space optical communications and non-invasive eye tracking [89] and provides simplified high-level control of low-level camera operation on an intra-frame basis. The architecture of the release 2.0 RARE camera is shown in Fig. 5-49. This figure illustrates the three-component system of the RARE camera, consisting of a custom imager card with a low-voltage differential signaling (LVDS) cable assembly, a commercial of-the-shelf (COTS) field-programmable gate array (FPGA) card, and a commercial processor. The imager card was designed with a Texas Instruments TC237 CCD imager chip [90] with two TLV987 signal processor chips [87]. Two 987 processors were required to handle the dual-pixel-stream output capability of the TC237 CCD. Each processor accepts an analog pixel stream and provides transistor–transistor logic (TTL)-level output signals to the custom LVDS cable. The cable assembly provides single-ended TTL-level input–output (IO) signals to the CCD card and the FPGA card, but it runs differential signals through a pair of small computer system interface (SCSI) cables to allow for high-speed strobe operation over several feet of cable. The FPGA card is a TransTech PMCFPGA-01 card with a 300 kilo-gate Xilinx XCV300E FPGA for the low-level controller of the CCD imager. The host tracking processor is a general-purpose computer with a 32-bit peripheral

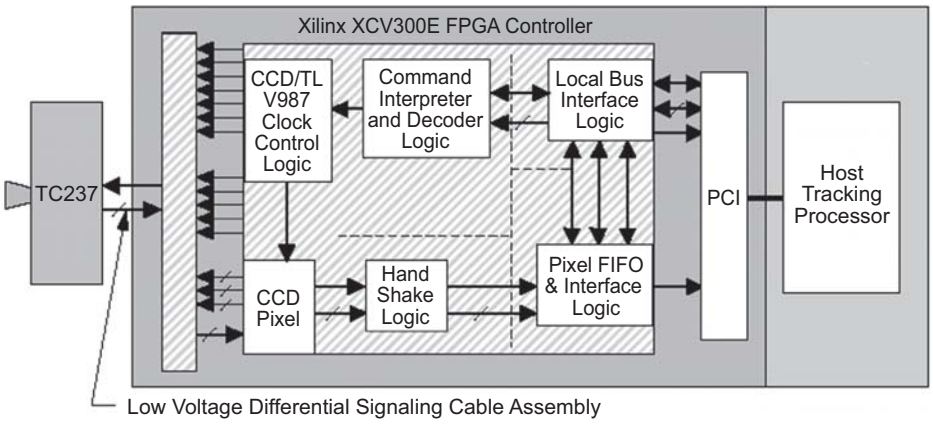

Fig. 5-49. Random-access real-time (RARE) camera tracking system architecture (FIFO = first in, first out; PCI = peripheral component interconnect).

component interconnect (PCI) bus used to provide FPGA control parameters, to read camera status, and to read pixel data from the FPGA card.

5.3.6.3.3 Multi-ROI Operation in Software. The host tracking processor loads ROI parameters into the FPGA controller to define the ROI size and location. These parameters are used to scroll through unwanted lines and unwanted pixels per line until the ROI is reached. They additionally define the number of pixels per line and the number of lines to read out for the ROI.

Dynamic adjustment of these parameters can be done on a per-frame or intra-frame basis to allow for enhanced system adaptation. They can be used to define an ROI for one or more frames, or they can be adjusted within one frame to allow for multiple ROIs within a single frame.

When readout of a ROI(s) is required, the tracking processor sets the mode of the FPGA controller to ROI readout and requests pixel data as defined by the ROI parameters previously loaded. The tracking processor then polls the FPGA controller for available pixel data to initiate the ROI readout from the pixel FIFO in the FPGA. If more than one ROI per frame is required, the tracking processor can load new size and location parameters for the next ROI without requesting a new frame transfer. The vertical location parameter of the next ROI is defined relative to the last line of the current ROI and denoted by the inter-window scroll area.

This methodology also allows for ROIs that overlap or share common rows of pixels with or without vertical separation. The primary difference as compared to the case above is in the definition of the ROI. For the case of common lines of pixels between ROIs, the tracking software must read out three different regions corresponding to the two areas where the ROIs do not share common rows of pixels and an additional third region containing pixels from both ROIs. This additional region must read out pixels for both ROIs and will have a width parameter defined by the left edge of the left-most ROI and the right edge of the right-most ROI. This methodology is illustrated in Fig. 5-50 for two ROIs and is applicable to N(>2) ROIs.

5.3.6.3.4 Dual-ROI Benchmark Results. The dual-ROI methodology was benchmarked to determine the achievable frame rates for this scheme. The "home" position of two 11×12 ROIs is defined by origins (320,236) and (320,248). These locations place the ROIs in the same columns and with a one-row separation at the center of the CCD FOV. The top ROI is allowed to move throughout any portion of the upper half of the CCD FOV, and the bottom ROI moves in an opposite sense throughout the bottom half of the FOV. The ROIs are moved in opposite directions to emulate the operational mode required in the acquisition and tracking platform. The reported frame rates include the time needed to perform frame transfers and read out the ROI data only. Figure 5-51 shows that frame rates from 900 to 1100 Hz are achievable for dual-pixel-

stream operation. There was no timing delay effect observed when shifting the ROIs horizontally. The reason for this result is that the total number of pixels read out from the CCD is constant. Consequently, the only parameter that affects the frame rate is the position of the last row of the bottom ROI. The reason for this result is that the only variable for this operational mode is the number of line-scroll operations performed, and the aggregate number of line scrolls increases as the bottom window is moved toward the bottom of the CCD FOV. A further increase in the frame rate is possible by using only a portion of the CCD FOV. This approach requires the defining of a sub-region of the CCD FOV and the centering of the ROIs in this region. The number of line scrolls and pixel reads is reduced by moving the "home" position of the two ROIs closer to row one, column one of the CCD FOV.

The RARE camera provides a key component for the real-time, adaptive tracking platform. We have developed this infrastructure by implementing a methodology to quickly extract pertinent pixel data using a commercially available progressive scan imager. This technology is also well-suited to adjusting the camera parameters to accommodate changing ambient and target conditions during tracking. In this section, we presented details of the RARE camera design based on the Texas Instruments TC237 CCD imager chip. The novel feature of this design is the use of an event-driven paradigm for imager control. This capability was implemented by developing a custom FPGA controller that converts a commercially available CCD imager into a smart pixel device. Communication to the FPGA controller is via commands from a host tracking processor. This combination of FPGA controller and host tracking

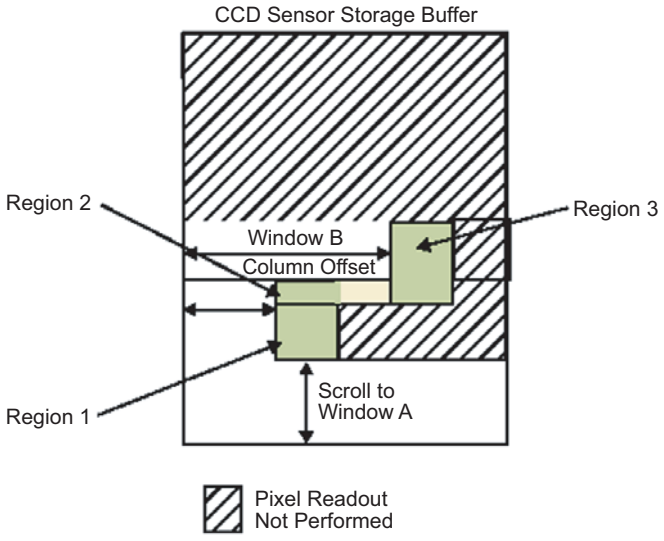

Fig. 5-50. Region-of-Interest (ROI) readout with common rows of pixels.

processor provides for higher-level commands to handle low-level imager operation for dynamically controlled ROI capability on a per-frame and intra-frame basis.

To assess the speed performance, several experiments were conducted for single- and dual-ROI operation. The first experiment illustrated the change in frame rate for a single fixed ROI origin and varying ROI size. The second experiment illustrated the change in frame rate for a single fixed-sized ROI with varying origin from the first row (top) and first column (left) of the CCD FOV. The results from these experiments achieved 75 percent of the theoretical best-possible frame rates for this CCD imager. The difference between the theoretical limit and the experimental results is due to a combination of both fixed and variable delays in the FPGA logic and host tracking processor software.

The dual-ROI results presented in Fig. 5-51 show that frame rates from 900 to 1100 Hz are achievable for two 11 × 12 ROIs centered about the CCD FOV. The two ROIs move in a counter-propagating fashion to emulate the operational mode of the envisioned acquisition and tracking platform. These frame rates will vary if the ROIs are allowed to move in a co-propagating fashion, as would be the case for the tracking of two targets within a scene. The frame rates for this case are governed by the ROI sizes and by the relative positions of the ROIs.

A nearly two times speedup is possible by running the imager at its maximum possible clock speed of 20 MHz per pixel stream. Additional speed

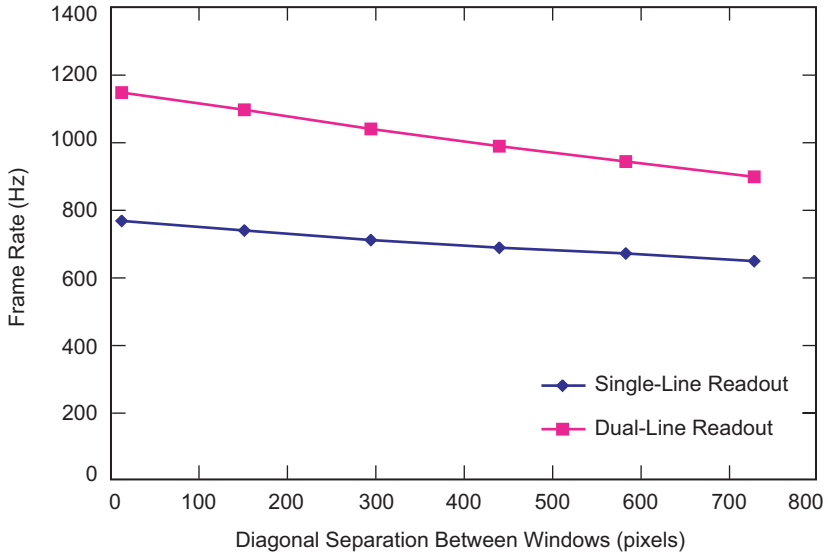

Fig. 5-51. Two-window ROI timing with diagonal shift. (Windows start at center of FPA and move to opposite corners.)

increases require using a different progressive scan imager with more than two pixel outputs to provide more parallelism in accessing the image data. Due to the generality of the RARE camera control scheme, the FPGA controller can be used for other commercially available CCD imagers to optimize system performance in terms of speed, image quality, or other parameters of interest.

5.3.6.4 Accelerometer-Assisted Beacon Tracking

5.3.6.4.1 Increasing Loop Bandwidth with Dim Beacon Sources. In deep-space optical communications, acquisition, tracking, and pointing are all challenging because of the stringent—on the order of sub microradian—pointing requirement. To achieve this level of pointing accuracy, one must maintain high-bandwidth tracking control. Feasible tracking sources (beacons) include uplink laser beams and celestial objects such as the Earth, the Moon, and stars. However, these tracking sources do not all provide the kilohertz tracking rate needed for pointing in deep space. One approach to enable a high tracking rate is to augment the tracking loop with inertial sensors to estimate high-frequency beacon movements [91]. In this section, we discuss the use of linear accelerometers, mounted in a configuration to measure angular displacement, to achieve high-bandwidth tracking with dim beacon sources. The advantages of linear accelerometers (or angular accelerometers) are their low cost, high bandwidth, and small size compared with other inertial sensors such as gyros. Simulation and experimental results show good agreement. A tracking bandwidth increase of 11 times has been demonstrated [92].

High-data-rate, narrow-beam optical communication imposes the challenge of pointing a downlink beam to a fraction of the beam divergence, typically sub-microradian in jitter and bias. This, in turn, requires a reference optical source, a beacon that can be used as a reference for closed-loop tracking/pointing control. In the past, ATP system design required a beacon-tracking rate of several kilohertz to maintain the link properly. The required tracking rate depends on the platform vibration amplitude and frequency contents. A typical tracking source has been a laser beacon, especially for short-range optical communications such as intersatellite optical links [93].

However, the kilohertz beacon-tracking rate is not readily available in most deep-space applications due to the long range that limits beacon energy collected at the spacecraft telescope. This is true even for Earth-image-based tracking and star tracking [54]. The challenge is to achieve high-rate beacon tracking, even with low-rate beacon centroid measurements, that is, to estimate accurately the relative beacon position movements between the measured beacon centroids. In the past, similar problems were addressed with the use of inertial sensors: spacecraft attitude control using star trackers and gyros [94], and (in the case of the Hubble telescope) pointing using star trackers and various inertial sensors [95]. Although these applications are slightly different,

the underlying principle is identical. Since the downlink target is moving very slowly in inertial space, all high-frequency motions come from the spacecraft. The high frequency movements of the beacon relative to the target can be deduced from the measurements of the source (platform) vibrations that cause movements of the reference beacon (either laser beacon or celestial objects) on a CCD array. If the error between the true and the estimated beacon positions is smaller than the error budget, a fast tracking rate can be maintained. Implementation of this concept requires accurate high-bandwidth inertial sensors. Among the possible inertial sensors are angular-rate sensors, angle-displacement sensors, gyros, and angular and linear accelerometers. Because of the low cost of linear accelerometers (as well as their accuracy over high bandwidth, small size, and availability) they make an attractive option for implementation. Using linear accelerometers requires double integration for the position estimation from acceleration measurements. Furthermore, linear accelerometers are not as sensitive to low-frequency vibration as are gyros, a feature that limits their usage in the case of very low beacon intensity. However, previous use of linear accelerometers suggests their promise in a range of ATP applications. Linear accelerometers have been used successfully, in the line-of-sight stabilization of a gimbaled imaging sensor suite [96] and in measuring the rotational and translational acceleration of a rigid body [97]. For deep-space optical communications, we sought to demonstrate that linear accelerometers could be used for beam pointing and control as well as for line-of-sight stabilization and for measuring the movement of a single body. For the double integration of accelerations to estimate displacements, some problems and solutions for zero-mean displacement signals have been addressed [98,99].

The key issue in high-bandwidth tracking is the availability of beacon centroids at high rate. Given the limited beacon intensity in deep space (thus, small number of beacon centroids available) and the fact that the beacon movements are caused by spacecraft vibration, it is essential to be able to estimate the beacon centroids (or movements) at times when the beacon centroids are not available. In this section, we give the three-accelerometer configuration for the two angular position estimations and describe the algorithm used. Detailed treatments of the trapezoidal method for the linear displacement estimation, initial velocity/acceleration bias estimation, and random error analysis are given in [92].

5.3.6.4.2 Algorithm Theory. Angular displacements on two axis (α, β) can be obtained using three accelerometers, as shown in Fig. 5-52. Let α (horizontal) and β (vertical) be the angular displacements of the x−z plane around the z-axis and the y−z plane around the y-axis, respectively. A_1, A_2, and A_3 represent three accelerometers, and d_1, d_2, and d_3 represent the corresponding estimated linear displacements. Linear displacement estimation from the acceleration

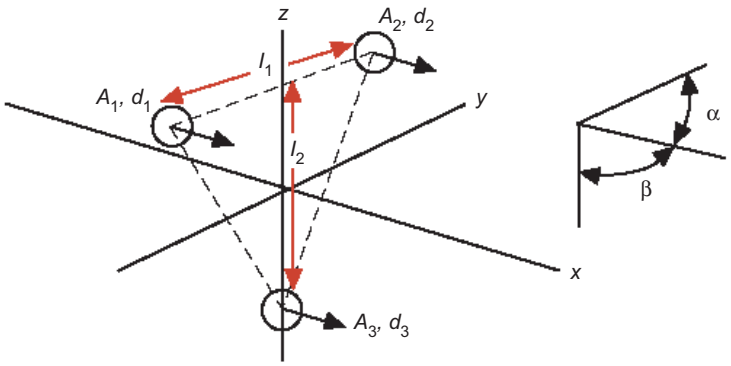

Fig. 5-52. Triangular configuration of three accelerometers.

measurements using the trapezoidal method is described in [92]. Then, the two angular displacements due to the three linear displacements are

$$\left.\begin{aligned}\alpha &= \frac{d_1 - d_2}{l_1} \\ \beta &= \frac{\frac{d_1 + d_2}{2} - d_3}{l_2}\end{aligned}\right\} \tag{5.3-29}$$

where l_1 is the separation between A_1 and A_2, and l_2 is the separation between A_3 and the middle point of the line connecting A_1 and A_2.

Angles at the Nth sample time can be represented as

$$\left[\alpha_N \beta_N\right] = B\left\{C\left[D_1 D_2 D_3\right]\right\}^3 \tag{5.3-30}$$

where

$$B = \begin{vmatrix} \frac{1}{l_1} & \frac{-1}{l_1} & 0 \\ \frac{0.5}{l_2} & \frac{0.5}{l_2} & \frac{-1}{l_2} \end{vmatrix}$$

$$C = \left[1, (N-1)\Delta t, \frac{1}{3\Delta t^2}, \frac{\Delta t^2}{6}\right], N = 2$$

$$C = \left[1, (N-1)\Delta t, \left(\frac{0.5N-2}{3}\right)\Delta t^2, (N-2)\Delta t^2, \cdots, (N-i)\Delta t^2, \cdots \Delta t^2, \frac{\Delta t^2}{6}\right], N > 2$$

Δt = sampling interval

$D_i = \left[d_{i1} v_{i1} \alpha_{i1} \alpha_{i2}, \cdots, \alpha_{iN} \right]^T$

d_{i1} = initial position of d_{iN}

v_{i1} = initial velocity of d_{iN}

d_{iN} = displacement estimation at the Nth sample time from $\alpha_i's$

$\alpha_{i1}, \alpha_{i2}, \cdots, \alpha_{iN}$ = accelerometer outputs from accelerator $A_i, i = 1,2,3$

5.3.6.4.3 Algorithm Design. Figure 5-53 shows all the major signal flows, from three accelerometer measurements, two angle reference inputs (beacon position centroids), and the final outputs of the two angular position estimates of the angular position estimation algorithm (APEA). Additional inputs are reference signals in terms of beacon centroids (x-axis, y-axis). The linear displacement estimator produces three displacement estimates corresponding to the three accelerometer outputs. Combined with the three initial positions derived from the beacon centroids, three position estimates (p_1, p_2, p_3) are obtained. These are, in turn, inputs to the initial velocity and acceleration bias estimator. The estimated initial velocity and acceleration bias are fed back to the linear displacement estimator to improve the next position estimations. The final angular position estimations are obtained from the estimated three linear

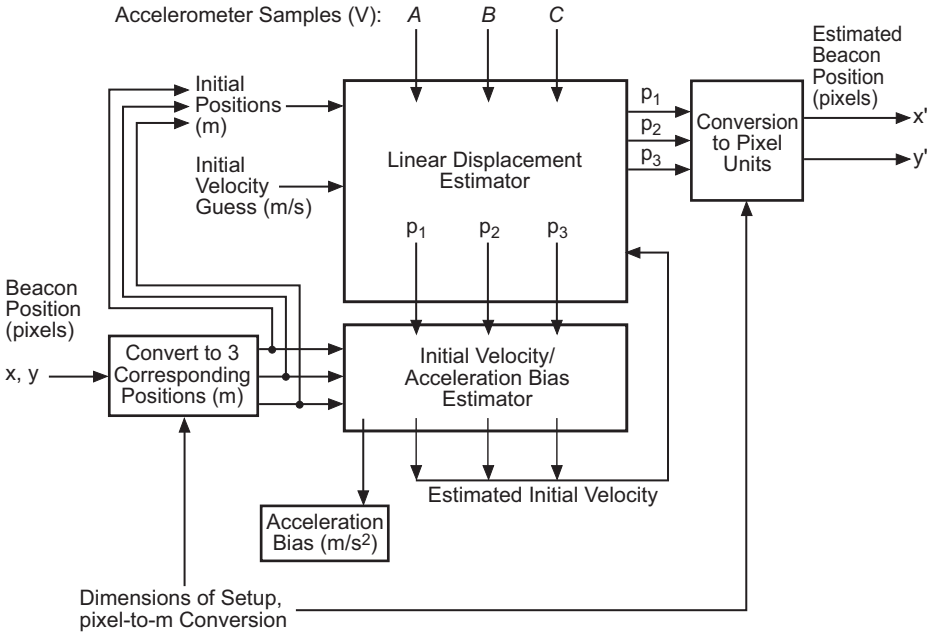

Fig. 5-53. Angular position estimation algorithm (APEA) block diagram showing the major signal flows.

positions, after performing the linear displacement-to-angle conversion [Eq. (5.3-29)]. The rate of beacon reference inputs to the APEA determines the reference reset period, *N*. For example, if $N = 2$, every second beacon position output is an estimation, while the other is the true beacon position. If $N = 5$, every 5th output is the true beacon position. For this experiment, we did not do any smoothing over multiple beacon samples due to the noise of the accelerometers.

5.3.6.4.4 Algorithm Simulation. A three-accelerometer configuration of the experimental setup was used. Sinusoidal signals of 1, 10, and 100 Hz for vibration were used with an assumption of zero measurement noise. The only error sources are the algorithm errors of the APEA. Figure 5-54 shows the displacement estimation results. As shown, the error increases with both the frequency of the vibration signal and the reference reset period.

5.3.6.4.5 Experimental Validation. For the experiment, three accelerometers were mounted around the optical communications terminal, and the entire setup was placed on a vibration table (Fig. 5-55) [100]. The experimental procedure was as follows.

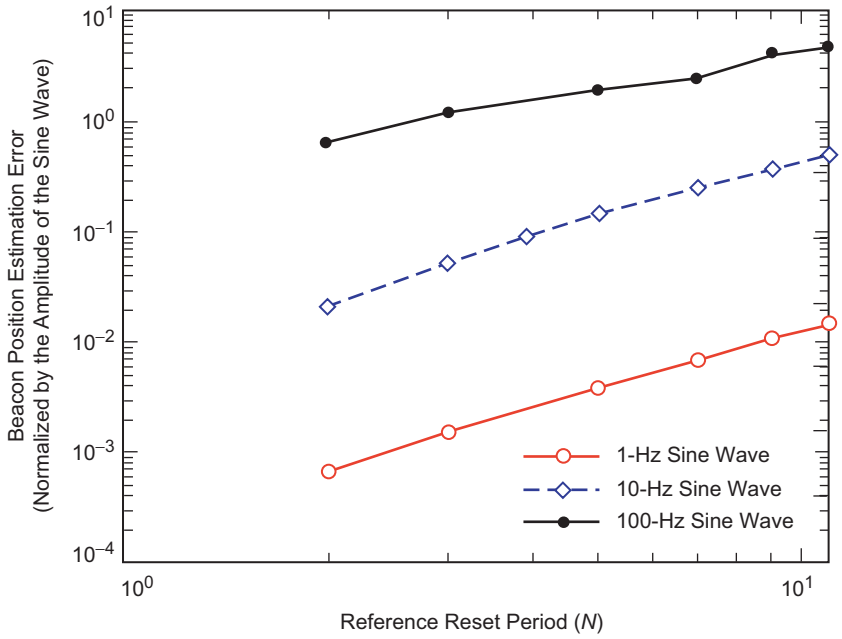

Fig. 5-54. Angular position estimation error as a function of reference reset periods for sinusoidal signals of 1, 10, and 100 Hz. The error is proportional to both the reference reset period and frequencies of the underlying vibration signals.

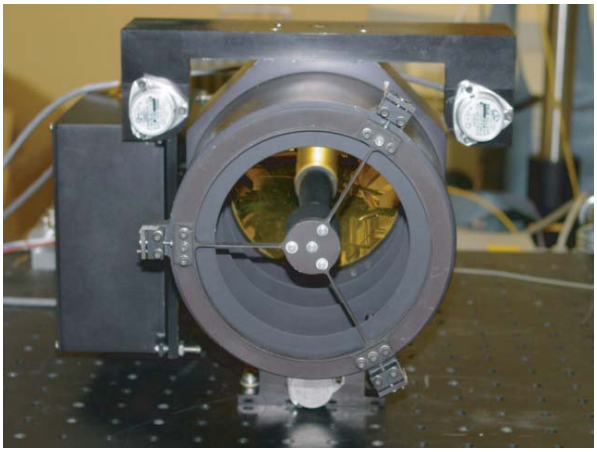

Fig. 5-55. Three accelerometers were mounted around the optical communications terminal, and the entire terminal was place on the vibration table. The piezo-actuator underneath was commanded to shake the table with the generated vibration signal.

1) Generate the angular spacecraft vibration signal to command the piezo-actuator. In this experiment, the laboratory-measured Cassini spacecraft vibration [linear acceleration power spectral density (PSD)] was used to derive the angular vibration signal for a more realistic frequency content of the expected deep-space vibration signal. The amplitude of the vibration signal was inversely proportional to the length of the interface plate of the optical communications terminal. For this experiment, 15 cm was used. The transformation of linear acceleration into rotational displacements was done following the procedure in [101].
2) Command the piezo-actuator to shake the platform vibration table with derived PSD.
3) Measure the angular motion (reference vibration signal or beacon centroids) using the optical communications terminal.
4) Run the angular position estimation algorithm with various reference reset periods.
5) Compute the angular position estimation error. The derived vibration signal was sampled with a CCD at a 625-Hz rate.

The experiment was done for reference reset periods of 2, 3, 5, 7, 9, and 11 frames. The beacon position estimation results for a reset period are given in Fig. 5-56. As was indicated in the simulation results, the error is proportional to the frequencies of the vibration signals. The error also grows for larger reference reset periods (Fig. 5-57).

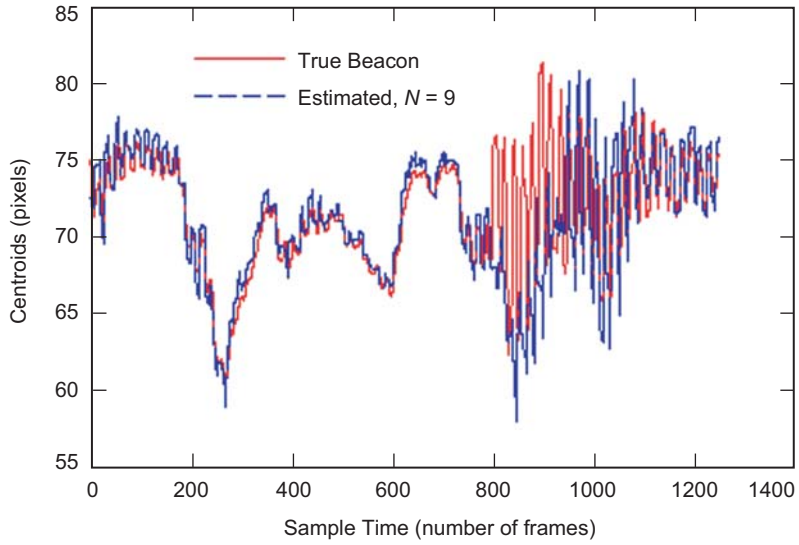

Fig. 5-56. Experimental beacon position estimation results for a reference period of 9 frames. As was shown in the simulation results, the larger error is noticeable for larger reset periods.

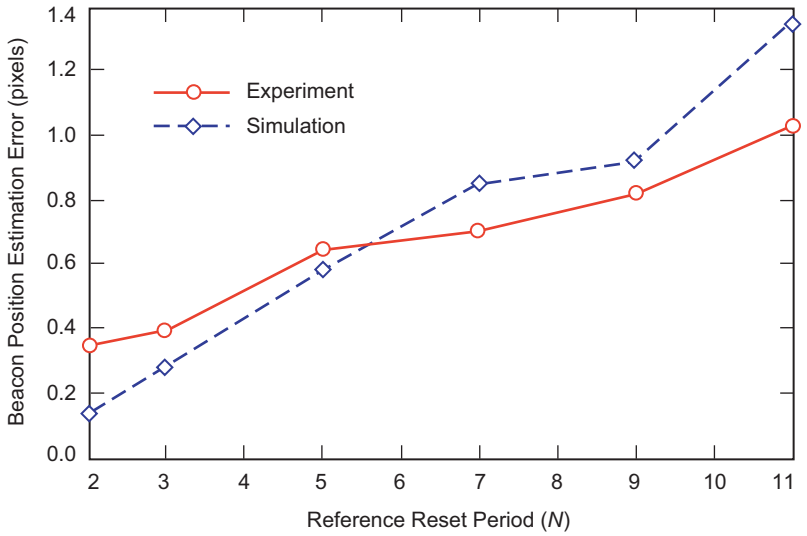

Fig. 5-57. Comparison of the experimental and simulation results. The measured vibration on the CCD of the optical communications terminal was used for the simulation with an assumption of zero noise in the acceleration data. Overall estimation (RMS) errors match between the two results.

Overall, the simulation and experimental results matched closely. The amplitude of the vibration signal shown in Fig. 5-56 is about ±10 pixels (or 36.1 μrad). The resulting angular position error is about 1 pixel (or 3.61 μrad) for the reference reset period of 11 (Fig. 5-57). Since the estimation error is directly proportional to the amplitude of the vibration signal, the desired sub-microradian pointing is achievable for the deep-space optical communications if the spacecraft vibration can be suppressed below a certain threshold. The threshold depends on the amplitude and frequency contents of the specific spacecraft vibration. For our experiment, about one-third of the given vibration amplitude, or ±12 μrad, would give microradian-level error in angular position estimation for the reference reset period of 11, as an example. This would increase beacon-tracking bandwidth by 11 times. Therefore, a tracking bandwidth of 1 kHz can be achieved with a beacon tracking rate of 91 Hz.

The concept of using linear accelerometers to increase the tracking bandwidth can be applied for deep-space optical communications tracking and pointing with a trade-off for the additional error in the beacon position estimations. Simulation and experimental results show good agreement in the beacon-position estimations with the various reference reset periods. The results also showed that the estimation error is proportional to both the reference reset period and the frequencies of the vibration signals.

5.4. Flight Qualification

Hamid Hemmati, William T. Roberts, and Malcolm W. Wright

During the early days of the Apollo program, there was great concern at NASA Headquarters over the effect on the program of a failure outside of earth orbit. Because of the obvious safety concerns, NASA leaders were insistent that the Apollo missions hold to a standard of 'three nines' (99.9%) reliability during the lunar phase of the mission. The NASA administrator questioned Dr. Von Braun, asking him if he could be assured of this level of reliability. Dr. Von Braun considered the question, and then put the question (in German) to each of his four lead engineers, "Can you think of any problems which might cause a catastrophic failure." Each engineer answered confidently "Nein!" At the completion of this questioning, Dr. Von Braun turned back to the contingent from NASA Headquarters, and said, "Gentlemen, I give you four 'neins' reliability!"

Anecdote related by Dr. Ernst Stühlinger
Former Associate Director for Science,
Marshall Space Flight Center, Huntsville, Alabama

5.4.1 Introduction

The expense of launching spacecraft, and the limited ability to repair or replace components on deep-space missions, leads to the practice of producing

flight hardware systems using the highest grade components available and proving their reliability and durability in the space environment through rigorous, repeated testing. This process is known variously as flight qualification or space qualification, and it is applied in varying degrees of rigor, depending on the mission. The flight qualification testing of electronic and electro-optical parts is often very expensive, requiring many tests on many sample parts to validate the reliability claims and assure in-flight performance.

This portion of the chapter is intended to provide an overview of the process of flight qualification and the various levels to which testing is carried out under typical flight qualification is described here. The description begins with an examination of the approaches available in qualifying parts for space flight, and describing the latitude to which one can reasonably tailor a flight qualification program. Section 5.4.5 goes on to explain the various conditions under which a deep-space optical communications terminal may be called upon to operate, and covers most of the environments of concern on a deep-space mission. The final section deals with the specifics of qualifying electro-optic detectors, lasers, and other optical components for space flight.

5.4.2 Approaches to Flight Qualification

There are two main approaches to the development of parts that are ultimately qualified to operate in space. In the first approach, flight parts are developed for the particular space environment from inception. In this case, a part can be designed with operating requirements in mind from the beginning; environment-tolerant processes, materials, and structures can be designed to accommodate operation at the required levels; and manufacturing systems with traceability and accountability can be implemented to achieve the goals and requirements of the program. This approach is obviously difficult to implement, and it requires an extremely long lead-time to set up the facilities and establish the procedures that will ensure part survivability. As a result, flight parts development for a particular space environment is generally expensive to implement. Programs have been developed along these lines; device and materials development for operation in space environments and in high radiation environments have been pursued for development of detectors and CCDs under various military programs. However, they are usually implemented only after existing products intended for terrestrial applications are tested and shown to be inadequate [102].

The more common approach to flight qualification focuses on the testing of commercial off-the-shelf (COTS) components, with the intent of determining the likelihood that the particular component will withstand the environment to which it is to be subjected. In many cases, COTS components can withstand many of the stringent requirements levied on them by the space environment. However, because they may never have been tested to this level, there is little

or no data upon which to rely. In this case, lots of components must be purchased and rigorously tested to determine the part's reliability under expected space conditions. This process is referred to as "up-screening," which is the main focus of the section on qualification of specific parts and materials (5.4.6 and 5.4.7).

Usually, preparatory research is invaluable in selecting a part that will require much less additional screening, and it will have a favorable impact on the program's cost and schedule constraints. For example, it may be that a particular detector was used on a previous flight program. Successful performance of the detector under the particular conditions of that mission is somewhat useful in providing confidence of the part's reliability, even though the vibration, thermal, or radiation environments may be different. It is likely that there will be test data on any similar components used to qualify the flight part on the mission. This data will be useful in flight qualification of the considered part, though the cognizant engineer must check with the manufacturer to assure that the materials, structures, and processes of component manufacturing have not changed in the interim. The most fortuitous outcome of this research may be that there are additional flight-qualified parts, either spares in flight storage or perhaps integrated into an engineering unit, which may be available to the program.

If the failure rate of a part is too high to be acceptable, minor modifications to the manufacturing processes and materials and testing methods are pursued first in an effort to effect a remedy. The screening tests should be helpful in indicating the source of the failure, and generating data that can be used to develop more environment-tolerant designs or assist in the selection of materials and processes. While this process is expensive and time-consuming, it nevertheless is still significantly less costly than setting up a dedicated manufacturing line for flight-qualified component development.

Here again, research is very important in identifying potential cost and schedule savings. There may be alternative parts that already incorporate the changes being considered to the product, and knowledge of the performance of those parts under the particular environment leading to failure may help to avoid a costly dead-end in the development of a qualified component.

Finally, if the changes required to bring a part up to the specifications will have a significant impact on the cost or schedule of the component integration, this must be communicated back to the project. In many cases, the component requirements can be relaxed with little or no impact on the overall performance of the system. For example, radiation-tolerance requirements may be relaxed by the addition of shielding to the system, or often simply by placing the component in a different location within the spacecraft. Vibration requirements can be relaxed by minor modifications to the structure or component placement to avoid particularly sensitive resonances. Addition of a thermal shield, addition

of a heater, or placing the component in a more benign location may afford a significant relaxation on thermal excursion and thermal cycling requirements.

5.4.3 Flight Qualification of Electronics and Opto-Electronic Subsystem

A number of different standard procedures and test methods have been established from which to draw upon in establishing a flight qualification program. These procedures and test methods have been adopted from the military standard (MIL-STD) test procedures [103]. Though these standards are generally provided for testing electronics components, many of them are equally applicable to optoelectronic components. A basic list of these is provided below.

5.4.3.1 MIL-PRF-19500. MIL-PRF-19500 is a generalized set of performance requirements for qualification of semiconductor devices, and they are therefore applicable to semiconductor detectors and lasers. These test requirements were developed for qualifying military components that often have very different specifications and requirements, and so much of the test flow is not applicable. It calls out five different 'quality' levels.

MIL-PRF-19500 does not actually describe the tests, but rather the sequence of tests to be applied and allowable lot failures for qualifying parts. It refers to MIL-STD test procedures, generally MIL-STD 750 tests for semiconductor devices, indicating which tests should be conducted under various circumstances, and in which order the tests are to be applied. These test procedures are quite extensive for electrical systems, but limited for application to electro-optical devices. For the testing of detectors, one needs to supplement these tests with additional optical characterization to assure adequate radiometric performance. Such tests would likely include spectral responsivity, total responsivity, response uniformity, temporal response, dark noise as a function of temperature, responsivity as a function of temperature, and detector isolation and crosstalk, to name but a few. The ultimate selection of tests should be decided based on the required operational characteristics of the detector.

5.4.3.2 MIL STD 750. MIL STD 750 is a comprehensive list of tests and procedures for general semiconductor devices. The list covers environmental, mechanical, digital electrical, and linear electrical tests and procedures. Only certain tests from this suite are applicable to detectors, detector materials, and diode lasers, which are similar to MIL STD 883.

5.4.3.3 MIL STD 883. MIL STD 883 is a comprehensive list of detailed descriptions of tests for electronic microcircuits. This standard covers tests for a wide variety of environments (e.g., space, high altitude, land, underwater),

mechanical tests for material and construction integrity and vibration and shock environment survivability, digital electrical tests to exercise and verify the operation of digital electronic devices under various electrical conditions, linear electrical tests to characterize the operating performance and range of electronic devices under various electrical conditions, and test procedures. Most of these tests are only applicable to certain types of laser diodes, detectors, or packages. It is up to the qualification engineer to select tests from this suite that are applicable and of significant consequence for the expected environment.

5.4.3.4 Telcordia. Telcordia is a source of testing procedures particularly relevant to opto-electronic systems [104]. Telcordia tests were developed to establish a certification standard for terrestrial fiber-optic-based telecommunication components. The procedures rely heavily on MIL-STD-883 tests but are tailored for terrestrial-based opto-electronic components to ensure the standardization and reliability across the entire telecommunications infrastructure. Telcordia standards are the evolved set of qualification standards originating under Telcordia's previous name of Bellcore.

In general, parts that are Telcordia qualified have already passed some of the stringent qualifications procedures. They have a very extensive application legacy for mission life assurance and operation under most of the conditions required for flight-qualified hardware. Radiation testing and outgassing (the materials requirements for space applications) are noticeably lacking in the qualification guidelines.

5.4.3.5 NASA Electronics Parts and Packaging (NEPP). The NEPP program was developed to establish flight-qualification guidelines for electronic parts, including opto-electronic and photonics devices that might be used in free-space optical communication systems [105]. These guidelines are being developed with data generated from multiple testing programs to assess the effects of space environments on recently developed COTS components. The program consolidated the work of previous programs in space environmental testing, and it is currently addressing the relative lack of standards and procedures for the testing of opto-electronic and optical components. Issues of radiation tolerance and parts reliability testing are at the core of the NEPP program, but other issues (such as low temperature exposure, thermal cycling, mechanical shock, mechanical vibration, and aging) are also considered.

5.4.4 Number of Test Units

Clearly, successfully testing more parts results in higher confidence levels in the selected flight units. The problem is, how many units must be tested to achieve the level of confidence required by the mission?

The probability of failure of n units out of a sample of N units is governed by the binomial distribution, and is calculated by

$$P_f = \binom{N}{n} p^n q^{N-n} \tag{5.4-1}$$

where

$$\binom{N}{n} \equiv \frac{N!}{n!\,(N-n)!} \tag{5.4-2}$$

In this notation, N is the number of units sampled, n is the number of units that fail the test, p is the probability of failure of a randomly chosen device, and q is the probability that the device does not fail. The difficulty arises in that, in general, the failure probability p is not known *a priori*. To determine the probability of survival or failure (q or p) exactly requires that an infinite number of trials be conducted, because it is only in the limit as $N \to \infty$ that the trials give the exact probability. To account for the uncertainty in estimating the probability from a finite number of samples N, one can apply the estimated probability $\hat{p} = n/N$. Then, assuming a normal distribution from which the sample N was taken, and associating some error ε with the uncertainty in the estimated probability, the confidence level α can be derived for the sample. The derivation of this is beyond the scope of this book, but excellent references are available. The confidence level is shown to reduce to

$$\alpha = erf\left(\sqrt{\frac{N}{2}}\,\frac{\varepsilon}{\sqrt{\hat{p}\left(1-\hat{p}\right)}}\right) \tag{5.4-3}$$

in the condition that the product $Np >> 1$.

At this point, it must be kept in mind that the failure probability of an essential part for which flight qualification is necessary had better be small. This forces a large number $\underline{N}$ of samples to be tested, just to attain a high certainty that the failure probability is close to the estimated value. Because of this, other methods of testing are generally performed.

In practice, devices are often procured and tested in quantities of 5 to 100, based on the experience of engineers with the parts and failure mechanisms on similar parts. It is helpful to have information on failure rates, but again, this requires testing many units, indeed often in the thousands, to establish the reliability that is expected on some missions. Though detector vendors may maintain this information, they are often shy about sharing it. The small sample of devices deemed adequate for testing by the qualification engineer is

submitted to inspections and screening tests, and all parts are assumed by similarity to withstand the same loads across the lot.

5.4.5 Space Environments

The requirements of any space mission must ultimately address the unique demands of operating in the space environment. To qualify a system to operate in a space environment, its constituents, namely the components and subsystems, have to be qualified in the first place. A deep-space optical communication system has to survive the pre-launch, the launch, the cruise, and the prime mission's environmental conditions that may vary widely from one stage to another. The most egregious stresses include high vibrational loads during the launch phase and thruster firings on orbit; high thermal and mechanical loads in orbit due to the extremes of solar heat loads alternating with radiating to extremely low deep space temperatures; radiation-induced damage; and contamination resulting from out-gassing of materials in a high-vacuum environment. The magnitudes of these effects can vary depending on the mission, but most must be considered to some degree for any space-flight system. For example, while the radiation field is particularly strong in a Jovian mission, and temperature cycling is more demanding for an Earth-orbiting system, both radiation and thermal effects must be considered in each of the different missions.

Implicit in the definition of the environmental requirements is the need to consider the required operational lifetime of the system. For most concerns, the failure probability dies off exponentially with operation; outgassing falls with time on orbit as the outgassed material is emitted; thermal cycling problems tend to lead to early failures, but it is rare for failures to occur after many cycles. The exception to this rule is in total accumulated radiation dose, which accumulates roughly linearly with time on station, up to a level where the device no longer operates as required. Finally, the availability of resources on the host spacecraft will have an effect on the overall requirements levied on the system. For example, a large spacecraft in geosynchronous Earth orbit (GEO) will generally be able to provide significantly more power for thermal management, and more mass allocation for radiation shielding than a mass-limited and power-starved deep-space probe. Given the range of missions and above considerations, the following environmental requirements provide a backdrop for detailing the qualification plan for any flight optical communication system.

5.4.5.1 Environmental Requirements. A component, a subsystem, or a system prepared for spacecraft use may experience a variety of environmental effects [106–109]. The environmental conditions with major effects on the instrument and its constituents include:

1) Ionizing radiation (in space)
2) Vibration (handling and launch)
3) Mechanical, thermal, and pyro shock (orbit, launch)
4) Thermal gradients (due to solar irradiation)
5) Depressurization (from humid atmospheric pressure to vacuum)
6) Electromagnetic field emission/susceptibility, coronal arcing, plasma bias
7) Outgassing (cleanliness)

Generally, the environmental requirements are designated at the assembly level and sometimes at the subassembly level. These requirements are often more difficult to attain at the device or component level since the detailed design affects the requirements, and might not be known early in the spacecraft development process. In that case and in the absence of any specific localized information, one may assume the same environmental specifications for the subsystem and component levels, as well. To verify that the environmental requirements are met or can be met, analysis is needed in conjunction with a set of well-defined tests.

5.4.5.2 Ionizing Radiation. The space radiation environment is composed of many different types of ionizing radiation, comprised of large fluctuations in particle density, energetic distribution, and spatial distribution. Fortunately, we on Earth are shielded from almost all of the ionizing radiation by the Earth's magnetic field and our atmosphere. In leaving these protective barriers behind, the damage from radiation exposure of all types must be considered.

Sources of ionizing radiation in space are summarized in Table 5-18. Radiation types include electrons, neutrons, protons, heavy ions, and cosmic rays. Radiation effects range from single event upsets (SEUs) and single-particle damage to displacement damage and dosage accumulation leading to

Table 5-18. Sources of ionizing radiation.

Source	Type and Effect
Earth's Van Allen belts	Electrons, protons in Earth's magnetic field 1,000 to 6,000 km range, seen as low as 100 km
Galactic cosmic rays	High energy (100s of MeV) ions Belts shield LEO satellites
Solar flares	Highly intense protons, electrons, and some heavy ion bursts pump up the Van Allen belts
Fields around other planets and moons	Sulfur and oxygen near Jupiter and Europa Fields as high as 10 Grad
Spacecraft-borne reactors	Effect more pronounced in smaller spacecraft Secondary reactions in shielding may occur

gradual or sudden fatal damage. As one proceeds up from the Earth's surface, the upper regions of the atmosphere no longer provide enough density for the dissipation of cosmic-ray energy, allowing for high-mass cosmic-ray nuclei to be a radiation source. At regions above 20 km, the ozone layer is left behind, and materials must be capable of withstanding degradation from solar ultraviolet (UV) rays. These rays are of approximately the same energy required to bind many materials, especially hydrocarbons. As a result, these molecular bonds can be disrupted by UV, leading to material degradation.

Radiation sensitivity is highly dependent on the environment and the component itself. For example, passive optical elements and fibers are particularly sensitive to most forms of ionizing radiation including electrons, protons, and gamma rays. In contrast, diode lasers, some photodetectors, and some fiber-optic components are sensitive to displacement damage caused by protons and neutrons [110]. Doped fiber and polarization maintaining fiber are usually more sensitive to total accumulated dose of radiation, but not to displacement effects [111]. Germanium-doped (Ge-doped) glasses and rare–earth-doped fibers are particularly sensitive to radiation-induced photo-darkening [112]. Annealing and photo bleaching help recovery from radiation exposure, particularly at elevated temperatures.

Photodetectors, particularly Geiger-mode APDs, are especially sensitive to ionizing radiation [113]. Protons and cosmic rays result in false signals. Protons and neutrons result in displacement damage leading to higher dark current from the photodiodes [110]. In photodiodes with on-chip circuitry, total ionizing dose can be harmful. CCDs are similarly sensitive to radiation effects. However, active pixel sensors (APSs) are more immune to harmful radiation [114]. Also, detectors made of III–V materials (e.g., indium gallium arsenide and gallium arsenide (InGaAs and GaAs)) are less sensitive to harmful radiation effects than those made of silicon [115].

Diode lasers are less sensitive to ionizing radiation and more sensitive to displacement damage from protons and neutrons [109,115]. GaAs-based devices are robust with respect to typical radiation doses present in LEO environments with photo-bleaching possible in high power devices [116]. Laser active elements (e.g., Nd: YAG) are not very sensitive to radiation; whereas, doped fiber active laser or amplifier mediums are more sensitive to radiation [117]. Visible-region (e.g., 800 nm) fiber and fiber-optic components have a lower damage threshold than the near-infrared (1550 nm) fibers. In general, fibers and detectors do better at longer wavelengths. Modulator materials (e.g., lithium niobium oxide ($LiNbO_3$)) have relatively higher damage threshold [118].

Typically, the reliability and radiation hardness assurance (RHA) documentation is not available for commercial-off-the-shelf (COTS) components. Also, it is difficult to predict the radiation effects without testing. Even with testing, one cannot rely on devices to behave similarly since the

manufacturing process may change from one batch to other. Shielding of components generally helps, but not always. Certain levels of shielding may in fact slow down the highly energetic particles and increase their interaction cross section in the devices being shielded, leading to greater radiation sensitivity. Optics and opto-electronic devices also require a certain unobstructed field of view that may mean shielding is impractical. Manufacturer's packaging practices often make testing more difficult to perform. To fully understand the effects, lids of opto-electronic devices should be removed with direct exposure of the devices to the ionizing radiation. Each of the above effects and their consequences on the devices or subsystems is described below briefly. The possible adverse effects of major radiation effects on components and devices are summarized in Table 5-19.

As discussed earlier, radiation effects range widely among differing locations of space. Even for a given orbit, the radiation levels could vary significantly if it is an elliptical orbit. Two other variables are the amount of shielding and the duration of exposure. For example, the accumulated radiation dosage accumulated over a few years in a Martian environment behind 4 mils (0.1 mm) of aluminum is about 20 krad, while at Europa (a moon of Jupiter), one of the worst radiation places in our Solar System, radiation levels are 1 to 2 Mrad behind 4 mils of aluminum accumulated over one month.

5.4.5.3 Vibration Environment. The vibration environment is the vibration experienced by the subsystems and the system during ground handling and launch of the spacecraft. Adequate levels of design practice, followed by structural analysis and testing on the engineering model are required to ensure survivability. Depending on the launch vehicle used, the sinusoidal or other

Table 5-19. Possible effects of ionizing radiation on components and devices.

Radiation Effect and Type	Adverse Effect
Single event effects (SEE)	
Protons and heavy ions	
Single event upsets (SEU)	Soft failure
Single event latch up (SEL)	Functional and hard failure
Single event functionality interrupt (SEFI)	Recoverable failure
Single event burnout (SEB)	Hard failure in power transistors
Single event dielectric rupture (SEDR)	Hard failure
Displacement damage	Bulk lattice damage to photodetectors, diode lasers, and analog devices
Protons, neutrons	
Total ionizing Dose (TID)	Gradual and cumulative
Electrons, protons, gamma rays	Parametric, sudden degradation, malfunction
Single particle	TID failure of single transistor
Heavy ions	

mechanical vibrations and resonances vary greatly from spacecraft to spacecraft and will have a time-dependent and frequency-dependent component during launch. Figure 5-58 shows an example of typical launch vibration environments.

5.4.5.4 Mechanical, Thermal, and Pyro Shock Environment. Mechanical, thermal, and pyro shock are sudden changes in the environment. Subsystems and components experience shocks from explosive (pyro-activated) release mechanisms during fairing separation or spacecraft separation. Proper design practices followed by mechanical and thermal cycling of a selected number of subsystem or the prototype model under the specified environments and commensurate with the established military specifications (Mil-Specs) and military standards (Mil-STDs) are part of the qualification process. Figure 5-59 shows an example of a typical launch acceleration environment.

5.4.5.5 Thermal Gradients Environment. The temperature of a spacecraft may vary greatly as it travels from Earth to deep space, or the temperature rises and falls during a spacecraft's orbit. Temperature ranges of –200 to 50 deg C may be experienced for deep-space missions. A system's or subsystem's

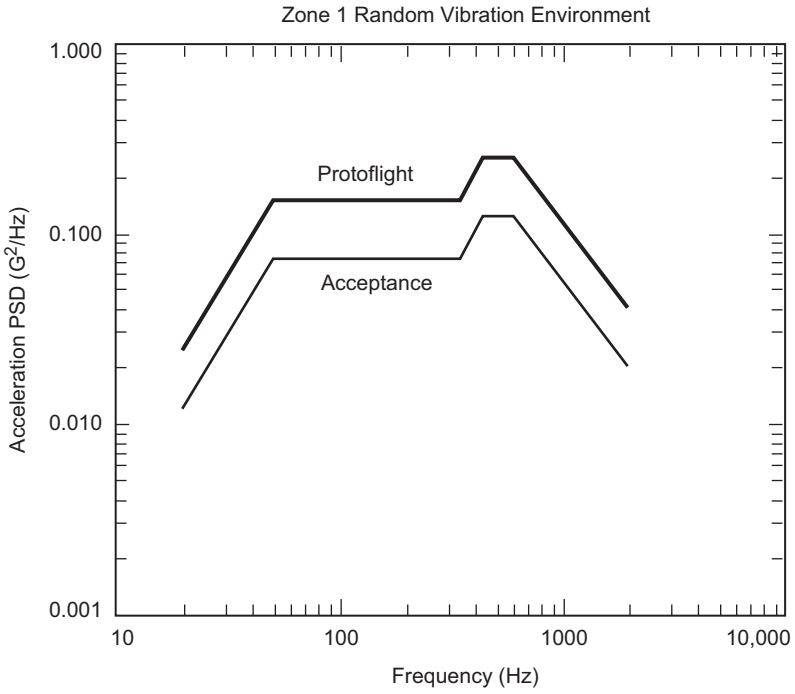

Fig. 5-58. Example of a launch vehicle vibration spectrum and pattern.

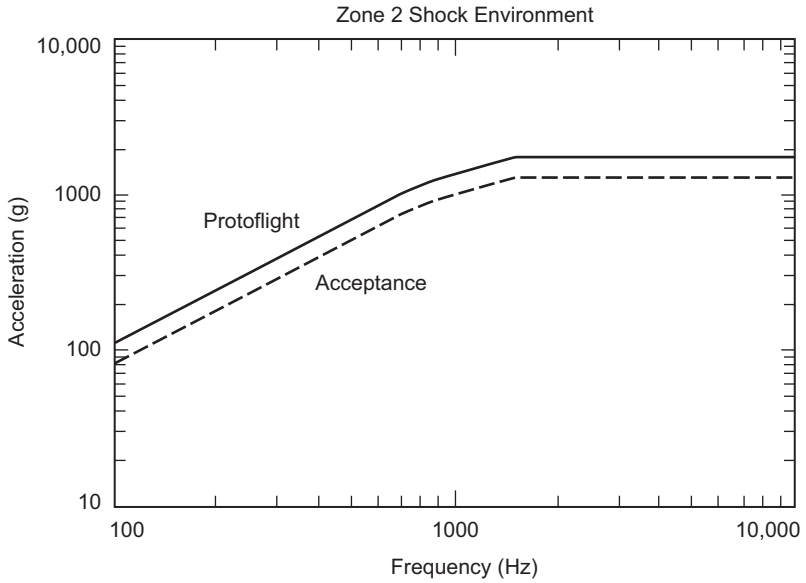

Fig. 5-59. Example of an acceleration profile during launch.

temperature may be maintained to within ±10 deg C if adequate mass and power are available for radiators and heaters. The concern is that thermal cycling and temperature gradients may induce misalignment of optics and laser resonators. Proper design practices, such as, selection of mechanical and optical parts, design of the laser resonator, and qualification at the prototyping stage, are required.

5.4.5.6 Depressurization Environment. During the ground assembly, the system operates under atmospheric pressure and a certain level of humidity. In space, the system should be either kept under pressure and hermetically sealed or operated under vacuum. Special design provisions, such as inclusion of windows, choice of very low outgassing materials, and allocation of vent orifices, should be practiced for each case. Again, vacuum testing at the prototype stage is necessary to insure integrity of optical alignment and functionality of the system. Hermetically sealed components have an advantage and are usually sealed with specific gases to either inhibit degradation (such as from oxidation effects) or act as getters for any impurities.

5.4.5.7 Electric and Magnetic Field Environment. The electromagnetic compatibility (EMC) is of interest primarily to electrical and electronics subsystems. Electric fields, magnetic fields, and electrostatic discharges could potentially pose a threat to the drivers, controllers, and the processor portion of a lasercomm terminal. Table 5-20 summarizes some of the known preventive

Table 5-20. EMC avoidance design practices.

Requirement	Design Practices
Electric field Emissions and susceptibility	Use of twisted shielded wires Control of grounding via single-point chassis reference Conductive mating surfaces between chassis and covers
Magnetic field Emissions and susceptibility	Use of twisted wires for high voltage and current leads Minimization of power and signal control loops Minimization of magnetic material content
Signal and control conducted Emissions and susceptibility	Use of optical isolation for controls
DC power conducted Emissions and susceptibility	Use of signal lead twisting and shielding Use of EMI filters and common mode choke Effective separation of signal and power wiring

design techniques, established to minimize the deleterious effects of electromagnetic interference.

Corona discharges can occur in vacuum between two sharp points held at sufficiently high voltages. Within a laser communication terminal, this can happen with the APD elements, the pump diode lasers, and the electro-optic Q-switcher or cavity dumper. Proper packaging typically avoids this problem.

5.4.5.8 Outgassing. Outgassing from materials used to fabricate the laser and from the surrounding material that can deposit and damage the optical coatings in the presence of strong beams within the laser cavity could be a major lifetime limiter for the laser. Telescope-mirror contamination with non-volatile residue can result in significant reduction of the Strehl ratio leading to major performance loss. Selecting and controlling the outgassing rate of materials and testing on the ground during the qualification process may minimize these. It should be noted that the vacuum surrounding a spacecraft could in fact be poor, with pressures on the order of 10^{-3} Torr (0.1 Pa). Also, there is the potential for particles and plasmas from outgassing and lack of proper cleaning procedures prior to launch as well as improper electrical grounding and charge build-up.

5.4.6 Flight Qualification of Detectors

In almost any electro-optical system, the performance of the detector is critical to the operation of the system, and often to the viability of the mission. Since optical systems are generally designed around the characteristics and performance of the detector, a reliable understanding of the operation, performance, and limitations of that detector is essential over the lifetime of the

mission, and under the various conditions to which the instrument will be subjected.

In this section, we define “detector” as a transducer in which high-frequency electromagnetic radiation (corresponding to visible, ultraviolet, or infrared light) is converted to an electrical signal. Various detectors operate in a variety of ways. Bolometers vary the current flowing through the device as a result of resistance changes in the detector material associated with their rise in temperature when they absorb energy. Photovoltaic and photoconductive detectors operate at a quantum level, promoting loosely bound charge carriers to the conduction band as a result of the absorption of a single photon. Detectors will be employed in sensor systems to perform various functions (Earth tracking, background measurement, signal detection), which will have differing levels of mission-criticality and sensitivity to degradation of performance.

Ideally, the detector performance and operation environment should be explicitly defined for the person responsible for sensor design and operational performance. This information typically comes from a detailed requirements flow down generated by the system engineer. This requirements flow down ideally should take into consideration the mission requirements, conditions, and constraints; and using reasonable estimates and experience, the engineer should develop an initial system design that allocates various performance requirements to each of the associated subsystems. In practice this is an iterative process, in which the system engineer communicates his initial design to the various subsystem engineers, who then respond as to the difficulty and cost of meeting these requirements under the specified conditions. Clearly, the initial design is a single point in a multidimensional trade space. As the system engineer negotiates with the responsible subsystem engineers, the design should quickly converge to a point that can be considered a local minimum in the cost/difficulty function in this trade space. For example, by using a more sensitive detector, the size of the collecting aperture can be reduced, resulting in what is generally a very welcome reduction in the size and mass of the system.

5.4.6.1 Flight Qualification Procedures. There are many different types of detectors which may be called upon to operate in a flight environment, The suite of flight detectors may include photoconductive detectors, bolometers, P-Type/N-Type (PN) or P-Type/Insulator/N-type (PIN)-type photodiodes, avalanche photodiodes (APDs), quadrant APDs, charged coupled devices (CCDs), active pixel sensors (APSs), or position sensing devices(PSDs), to name but a few. The remarkable sensitivity of modern APDs makes them the primary candidate for the receiver on a deep-space-based optical communication system. As the heart of the uplink receiver, the operational characteristics of these detectors must be thoroughly understood and controlled to obtain optimum performance of the uplink receiver system. APD failure

modes include all of those for normal photovoltaic detectors of the same semiconductor material, but the nonlinear mode of operation and the high potentials at which they operate tend to add additional concerns.

Testing of detectors for purposes of flight qualification should encompass tests that, to the degree possible, mimic the conditions and operational configuration of the part in the anticipated environment [118]. In addition to control of the environment, it is obviously most important to test the characteristics of the devices that the operational system will rely on. For example, though detector responsivity is frequently specified, in some circumstances the responsivity is less important than degradation of rise time or a change in operating voltage. This would be the case in a system that uses the detector primarily to record the timing of an event (such as the position of a communication pulse in a pulse-position-modulation format system, or range measurements in a laser remote-sensing system) rather than the radiometric intensity of the event. Of course, the system must still have the sensitivity to detect the pulse, and responsivity degradation will have some (generally minor) effect on the pulse timing.

Critical parts intended for long-term operation in space environments must pass a complicated and expensive screening flow that verifies that the part obtained will operate as required for the duration of the mission. The flight qualification process typically begins long before the parts are produced: the vendor corporate structure, manufacturing facility, process line, and operations are reviewed and inspected to certify that they adhere to good manufacturing, packaging, and testing processes [119]. Beyond the initial inspection, vendors and process lines must submit to periodic re-inspections to maintain their certification.

The first selection process for detectors begins at the wafer level (Fig. 5-60), where the material characteristics (resistivity, current/voltage (I–V) curves, etc.) are screened. This is intended to identify material that, through experience, tends to produce parts with the best operating characteristics and yield for space applications. Once good wafers have been identified and characterized, the fabrication facility makes use of these selected materials to fabricate detectors, the aggregate of which are referred to as a “lot.” From this point on, documentation on each individual part must be maintained. “Lot traceability” is required to amass the characteristics of the particular lot that, through statistical association, will be used to assess other devices coming from the same lot. It is usually advantageous to have devices from at least two lots, in case subsequent testing identifies a problem with a lot.

Each part must be electrically screened to assure that it meets basic operability. On a detector, this screen should consist of a current-voltage (I–V curve) measurement performed within the environmental (temperature, humidity, etc.) range of the final application. At this point, the entire population of detectors should be broken into groups that will undergo different types and

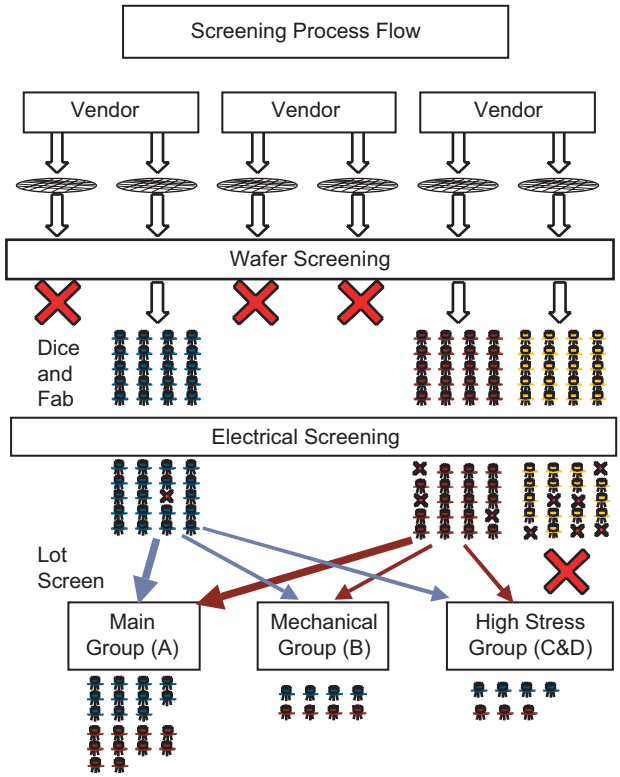

Fig. 5-60. Detector selection process (crosses signify rejected parts).

levels of testing. Each of these groups should contain samples from each of the different material lots used. The size of each of the groups will depend on the typical yield of such devices through the various qualification sequences. This will also determine the confidence level of the final parts chosen as flight units. Generally the largest group (Group A) containing roughly 2/3 of the individual parts will be the group from which the flight samples are drawn. Each of the detectors in this group will be subjected to a series of tests designed to eliminate non-performing or poorly performing parts, and to cause the failure of parts likely to fail early in operation through normally non-destructive tests. The second group of detectors (Group B) will be subjected to more stressing mechanical tests, designed to evaluate the limits of the parts to survive various stressing environments. Parts from this group will be subjected to conditions that can be expected to degrade their integrity and operability, and thus, the parts in this group should not be used for flight candidates. The third group (Group C) will be subjected to more destructive tests; these detectors will definitely not be candidates for flight parts. A fourth group (Group D) is usually included for space flight qualification, and includes parts from each lot that are

to be subjected to radiation testing. These parts can often be parts that have survived the Group C testing, reducing the total number of parts required. Qualification Flow of Main Sample Group (Group A) is shown in Fig. 5-61.

The first detector inspection is a simple visual screen, in which a technician visually checks the characteristics of a device, such as whether parts are properly aligned, if wire bonds are neatly formed, and if the detector materials or coatings are free from blemishes, residual manufacturing debris, etc. A comprehensive list of identifiable defects can be found in MIL-STD-883E 2008–2009. An experienced technician can identify such defects within seconds, making this a relatively high-throughput test with the ability to save a significant amount of time, effort, and cost in subsequent tests through early detection of defects and elimination of bad parts. Immediate feedback from the visual inspection will also assist the manufacturer in identifying the characteristics of parts coming from particular manufacturing equipment, processes, or personnel, who will quickly improve the overall manufacturing yield.

The parts that pass the visual inspection should be subjected to the first level of environmental tests, which would typically include an initial stabilization bake, the first round of low-level thermal cycling, and constant acceleration tests. These procedures are designed to cause the early failure or "infant mortality" of substandard parts. It may not be readily apparent after these procedures that a part has failed. This is commonly determined by the

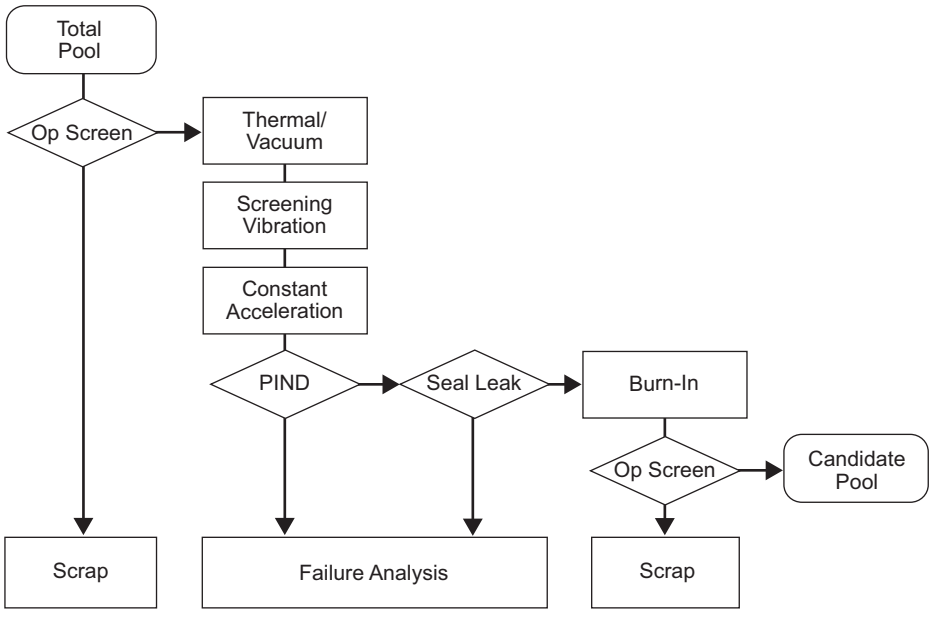

Fig. 5-61. Qualification flow of main sample group. PIND stands for particle impact noise detection.

particle impact noise detection (PIND) test and the fine and gross leak test. In the former, a microphonic transducer is attached to the detector, which is then subjected to vibration with acceleration of 10–20 g at 40–250 Hz. The transducer can then detect the impact of material that has been weakened or dislodged by the previous procedures, even though that material may not be visible through the detector window, or may appear to be attached. For top-level qualification for spacecraft parts, the lots or sub-lots are subjected to up to five PIND test runs. If the accumulated failures exceed 25 percent of the lot, the entire lot is rejected. Furthermore, if each particular PIND run continues to have failures after the failed devices were removed from the previous test, it indicates a continuous low-rate failure potential, and the entire lot is rejected. Only after a lot PIND test is run with failures of less than 1 percent can the lot be accepted.

The fine and gross leak test (MIL-STD-750D 1071) is used to verify the seal of the housing unit, which may have broken during the heating cycles, acceleration procedure, or PIND test. This test subjects the parts to pressure differences, during which gas flow from the sealed part is detected, or flow of gas or liquid into the part is observed. Various types of materials, including radioactive tracers, fluorocarbons, and dyes are used to detect leakage, depending on the type of part, volume of the enclosure, type of seal and detector characteristics.

Detectors that pass to this point are then nominally characterized electrically, principally through a measurement of the I-V curve, and detector responsivity under nominal operating conditions. An example of I-V curves for a photovoltaic detector is shown in Fig. 5-62. The top curve represents the un-illuminated detector; at low levels of forward bias current flows freely, whereas there is a limit to the amount of reverse-bias current that can be driven in the nominal operating voltage range. As the detector is illuminated, absorption of photons in the vicinity of the junction generates charge carriers that are swept away by the junction bias.

Damage to the detector will frequently show up at this stage of the testing, either through an open circuit, in which case little or no current will flow, regardless of the voltage, or a short circuit, in which excess current will flow, bypassing the detector junction. Short circuits are easily identifiable by observation of a change in the I-V curve as shown in Fig. 5-63.

Other types of damage or defects will present as a change to the detector responsivity. These tests can either by performed by making another I-V measurement under illumination conditions, or by simply operating the detector at a fixed set of nominal operational conditions (proper bias, temperature, and illumination). Significant variations (typically 2 dB or 37-percent variation from baseline) in detector response from the initial measured response should disqualify a detector from consideration.

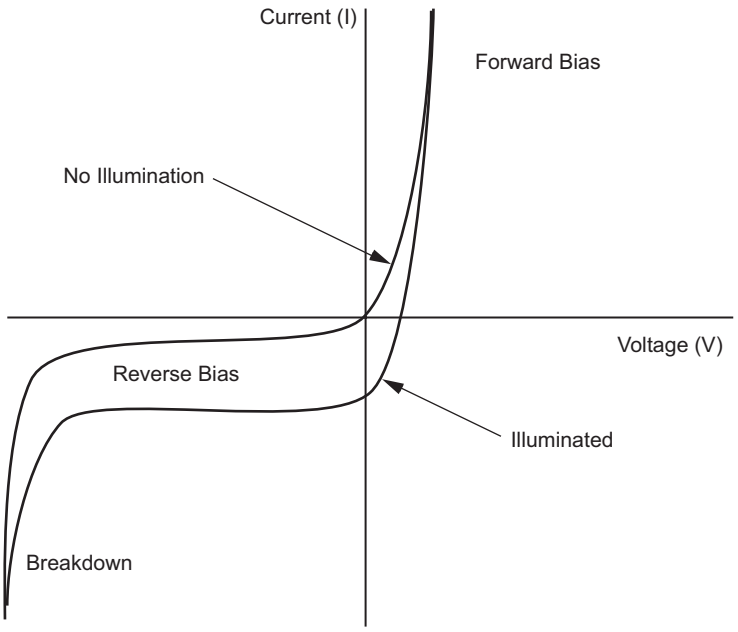

Fig. 5-62. An example of I-V curves for a photovoltaic detector.

The next procedure for the lot parts is generally a high-temperature burn-in, designed to induce the failure of time-dependent defects in materials and construction. The burn-in is generally performed under bias conditions for a period of at least 48 hours, and the part must be subjected to the suite of electrical tests within 24 hours of the burn-in procedure to prevent annealing from correcting any burn-in degradation. After the electrical tests, a second burn-in is performed, and electrical performance is characterized once again.

At the end of this testing, the fraction of detectors within the lot that continue to meet the specifications is calculated. This is referred to as the percent defective allowable (PDA) calculation. If the fraction of the lot that has failed exceeds a particular value (determined ultimately by the reliability and lifetime requirements) the entire lot is rejected. Otherwise, the detectors are subjected to a final suite of testing, designed to verify quality of the stock and to characterize the remaining electrical parameters. Failure of any part at this point simply eliminates it from further consideration, though the data is not used to disqualify the lot. Junction capacitance is measured, as well as spectral response (at the ultimate operational wavelength, if known). A final leak test is performed to verify hermeticity of the housing seal. The parts are then inspected, both through X-ray inspection (to identify internal mechanical defects) and an external visual inspection. The parts that pass these remaining tests are considered useful parts for stock, from which flight parts can be drawn.

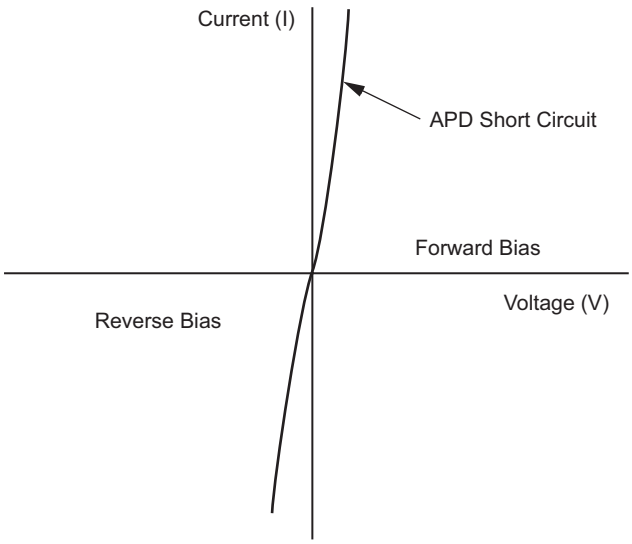

Fig. 5-63. Damage to the detector as evidenced by change in the I-V curve.

A flow diagram for the Mechanical Testing Group (Group B) is shown in Fig. 5-64. The following tests are performed on one of the smaller sample groups (Group B) culled out previously, and they generally consist of more rigorous, stressful mechanical tests unsuitable for parts that may eventually fly in space. Failure of these tests does not necessarily result in the automatic failure of the flight lot, but they are intended to generate information on the ultimate limits of the mechanical stresses to which the parts can reasonably be subjected and to identify unknown failure modes of parts.

This group is itself subdivided, with the majority of the parts going to the thermal-mechanical tests. Electrical testing (I-V curves, responsivity) is performed on these detectors at various intervals to track the device performance, similar to the testing used in the main qualification group. After characterizing the detectors, they are further subdivided, with most of the parts going to intermittent-operation lifetime testing. These tests consist of repeatedly turning the device on, and once the part has reached a stable temperature, switching the device off again. This test is intended to cause failures that would normally result from the electrical and thermal transients associated with normal operation. The remainders of the parts are subjected to thermal cycling, and then to thermal shock testing. This latter test subjects the parts to very rapid temperature changes, usually by immersion in liquids (typically water or perfluorocarbons) at various temperatures. The use of liquids speeds the thermal transfer, stressing the part beyond its maximum expected thermal change rate. This is designed to cause the failure of parts that may fail through mechanical stresses induced from large thermal expansion coefficients, or

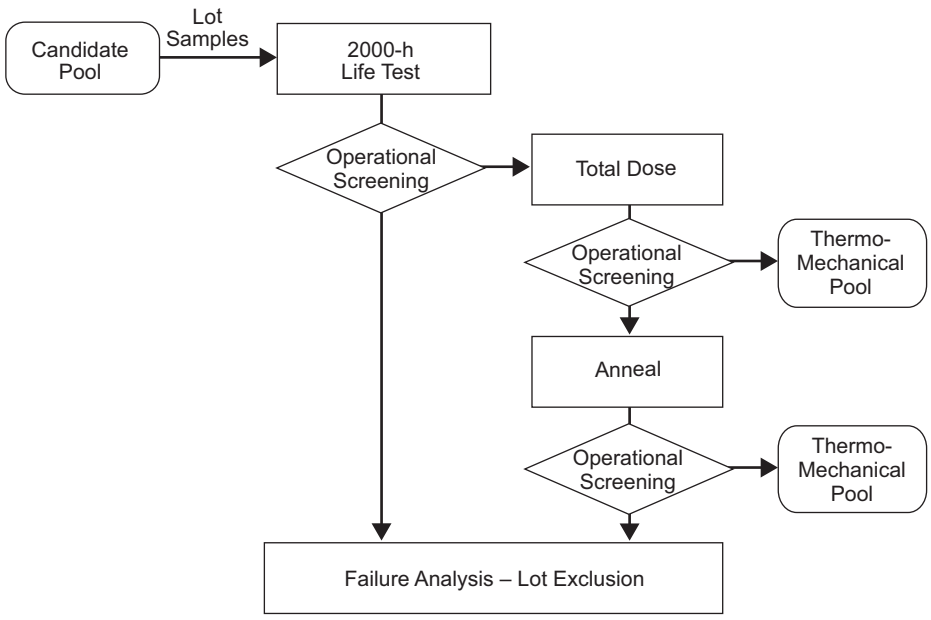

Fig. 5-64. Flow diagram of the mechanical testing group.

mismatches in thermal expansion coefficients. Electrical testing is used to determine failures that are not obvious to the testing personnel.

Some parts that pass the thermal cycling and thermal shock tests may then be subjected to destructive testing. The housing is removed, and a visual inspection is performed, principally to determine the previously undetected deleterious effects of thermal shock testing. Wire bonds are subjected to standard bond-pull testing, and integrity of the mounting of the detector is verified with a die shear test. Because of the destructive nature of these tests, they are clearly not available for final electrical characterization.

The remaining parts in this group (which may consist of rejects from previous tests) are subjected to a final set of mechanical tests. This set includes the measurement of the physical dimensions of the various parts, especially the sensitive surface area of the detector, the solderability of the part, and the solvent resistivity of the part. Solderability is intended to verify the integrity of the part after a typical soldering operation is performed, during which the temperature of soldering leads is quickly elevated to a high level, and subsequently dropped quickly at the end of soldering.

Figure 5-65 shows a flow diagram for the High-Stress Test Groups (Groups C and D). The remaining parts from the initial lot division are separated into high-stress test Groups C and D. These groups consist of detectors that are used to verify the performance degradation of detectors subjected to excessive mechanical shocks and ionizing radiation. The tests in

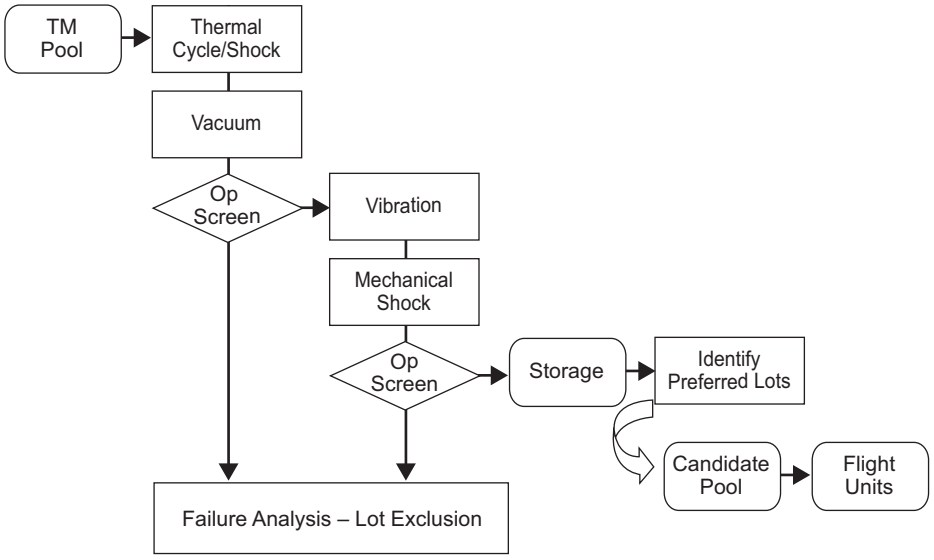

Fig. 5-65. Flow diagram for the high-stress test groups.

these groups again begin with electrical characterization, to establish a baseline against which detector degradation will be measured. Some of these detectors are subjected to high-stress mechanical tests, including the shock test, vibration testing, and constant acceleration testing. The first of these is designed to verify the integrity of the part that may be subjected to rather rough handling during integration and subsequent installation in the launch vehicle. Vibration testing is performed to establish the integrity of the part subjected to vibrations exceeding the amplitude, frequency, and duration expected to be experienced during launch. The amplitudes and frequencies are dependent on the type of launch vehicle to be used, and the subsequent effects of the structural-mechanical housing and support assembly. Because of the effects of damping and/or amplification of resonances in the surrounding support assembly, the expected vibration amplitude may be quite different from that of the spacecraft itself. Modeling and/or testing of the mechanical enclosure in order to derive the test requirements for this test should verify these levels. Finally, the parts should be subjected to a constant acceleration test, in which the ability of the part to withstand the acceleration of launch is verified. After the test detectors are subjected to these three sets of conditions, performance is once again verified by electrical testing.

5.4.6.2 Detector Radiation Testing. Space-based optical communications systems are expected to perform reliably in space for a certain required time period. Once in space, the detectors are typically subject to ionizing radiation that can degrade detector performance. The degradation mechanisms are still a

matter of intense research, but it is known that both responsivity and noise in certain opto-electronic detectors can be adversely affected by both the total accumulated ionizing radiation dose to which the detector is subjected, as well as the rate at which these doses are delivered [106].

The true radiation environment to which the detector is subjected is very difficult to calculate, and must take into account the varying spectrum of ionizing particles to which the detector will be subjected and the shielding of the detector resulting from the placement of various materials in and around the spacecraft. One might naively expect to test to an upper bound by merely using the conditions of the space environment, without the effects of shielding. Whereas this often will present a worst case, shielding can also slow down faster particles and thereby increase the probability that they will be absorbed in the photosensitive material.

A thorough analysis begins with the orbit (or alternately the deep-space trajectory) of a spacecraft and the anticipated energetic spectra of protons, electrons, neutrons, alpha particles, etc. Energetic protons are often the major consideration because of their tendency to be trapped in the Earth's magnetic field and the relatively high energies that they are capable of depositing into materials.

For interplanetary spacecraft, the type of radiation encountered during the long trip may dominate the radiation profile, or the radiation encountered at the final point of study may dominate. For example, during interplanetary flight, there may be relatively high probabilities of solar flares that can emit enormous volumes of highly energetic material into the interplanetary medium. Missions to Jupiter are also typically subject to high radiation doses because the planet's strong magnetic field traps extreme densities and energies of ionizing particles.

Example: As an example, consider the radiation testing required for flight qualification of a silicon avalanche photodiode (APD). The high operating voltage and high sensitivity of the device make it particularly difficult to qualify. Furthermore, the requirements for maintaining bias during radiation testing and subsequent optical characterization make it a particularly good case study.

Initially, the radiation effects engineer levies a requirement for the part, which takes into account the planned orbit of the spacecraft and models the attenuation effects of shielding, including spacecraft structure, materials, and instrument placement. For the particular case of interest, the requirement of 10 krad (Si) was levied for a total accumulating dose in the environment, and 51 mega-electron volt (MeV) protons were specified as the radiation type. This total dose level drove nominal testing to 20 krad (Si) for engineering margin. Furthermore, because it was hoped that the unit could be used on future Mars missions with longer operating lifetimes and slightly higher total accumulated doses, the decision was made to extend testing to a cumulative 40 krad (Si).

The method of qualifying the flight parts is to test similar parts, subjecting them to similar environments to those expected by the flight part. In this case, three Si APDs were subjected to a direct 51-MeV proton beam from a cyclotron. Prior to irradiation, each APD was optically characterized in a portable chamber of the design shown in Fig. 5-66. A Nd:YAG laser of the same wavelength as the flight laser (1064 nm) was used as a light source, and it was directed into an integrating sphere for polarization, randomization, and generation of a uniform extended radiance source. A short distance from the output port of the integrating sphere, two APDs were affixed side-by-side, each separated from the centerline of the integrating sphere output by small, equal distances.

At one APD port, a reference APD was used to verify output continuity from the integrating sphere. At the second APD port, the test APD was subjected to an identical optical input. Baseline current-voltage measurements were made on both APDs, both with and without laser illumination. Subsequently, radiation dosing was applied to one of the two APDs, and new I-V curves were obtained at cumulative levels of 5 krad, 10 krad, 20 krad, and 40 krad. Because the APD was expected to be biased throughout the mission, a bias voltage was maintained on the detector constantly throughout testing. The nominal bias voltage during irradiation was 275 V, at the lower end of the I-V curve voltage measurements. The upper voltage was typically the point at which avalanche breakdown was observed. The detector was not allowed to remain at breakdown for more than a few seconds at any time.

In this particular application, the APD was to measure the time of flight of a laser pulse, so the detector's temporal response was also an issue to be tested. To measure this, a separate chamber was designed in which the pulse from a passively Q-switched microchip laser at 1064 nm could be observed with the APD. A fast oscilloscope was used to measure the pulse rise time and fall time at different total irradiation dose levels.

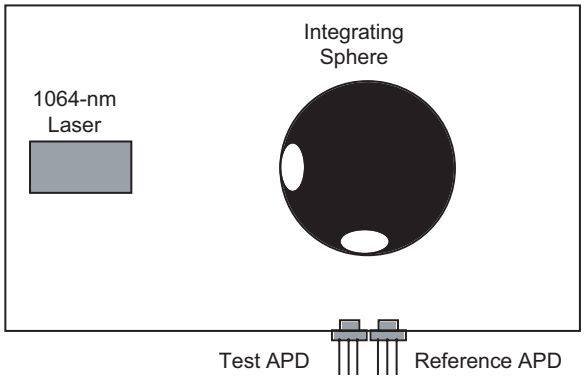

Fig. 5-66. APD optical characterization chamber.

Summary: Flight qualification of detectors is still very much an art, and draws heavily upon the experience and judgment of the cognizant engineer in selection of parts, selection of tests to be performed, and risk-tradeoffs in assigning test levels, test sequences, and numbers of parts to be subjected to tests. While the application of rigorous statistical methods can be used to derive confidence levels and assign numbers of detectors to be subjected to various tests, the relative success of the "art" of flight qualification, and especially at reduction in cost and schedule, prove the value of this more subjective method.

5.4.7 Flight Qualification of Laser Systems

Among the various types of lasers available, it is fortunate that space-based optical communication sources are based on semiconductor diode lasers, either as the seed or pump source. This is not coincidental since the terrestrial communication infrastructure requires similar performance and has invested significantly to ensure ruggedization for long-term reliability. Due to their compact size and power efficiency, diode lasers lend themselves well to communication applications. Other types of lasers such as gas-based systems are being investigated for space applications and bring unique challenges for space qualification [120]. Carbon-dioxide gas lasers have also been investigated for communication sources but will not be considered here for space application.

To develop a comprehensive space-qualification procedure for the laser system, a detailed knowledge of lasers is required with particular attention given to their potential sources of failure. One is referred to the many excellent texts on the principles and applications of lasers [20]. For a given space flight project, the qualification process has to be taken into account in the early stages of mission design along with the performance requirements. Failing to address the environmental requirements and their impact on the device design can lead to lengthy delays and budget overruns as workarounds are implemented late in the mission development cycle to mitigate problems evident during testing.

A process or guideline for qualifying laser systems is outlined in this section. The same rationale given in the above section for detectors can also be applied here. Several past missions have successfully deployed laser systems, some even for communications purposes. However, the qualification process has been somewhat arbitrary based on the individual mission requirements and budgets. As a background, where it is known, the qualification process is described for a selection of the past laser systems flown on different missions. Following that, the design and fabrication of semiconductor lasers is discussed in light of the stringent demands of the space environment. Given their ubiquity in communication sources, recommendations for a fully space qualified design are then given. These design options align with what is currently performed for high reliability in ground telecommunication fiber-optic systems. Prior to

addressing the actual testing flow, it is also helpful to understand the potential points of failure for laser systems. Understanding the various degradation mechanisms for the active diode and packaging along with the fiber interface allow one to tailor the tests, and this leads into the testing flow. The flow-down of tests has been customized from several programs as discussed in the final section.

5.4.7.1 Past Laser Systems Flown in Space. Lasers have been used extensively as sources for a variety of spaceborne instruments [121,122]. However, their qualification has been more arbitrary due to the unique technology involved. A partial list of lasers flown in space or being qualified for flight, along with a brief description of characteristics for each are given in Table 5-21.

The qualification of the above devices has varied from project to project. What is remarkable is the high degree of successful laser generation in the above missions, lending confidence in the qualification and reliability test procedures developed for each case. Most of the solid-state lasers have been custom built and tested as an assembled system through a series of vibration, thermal cycling, and vacuum tests. The diode-based systems (including the pump laser diodes of the Nd: YAG lasers) have relied on commercial devices upscreened through a further series of tests. Due to the varying mission and spacecraft requirements, it is not feasible to give a generic qualification procedure that covers all laser configurations from past missions. Also, the solid-state lasers can be thought of as optical systems with the inclusion of an active-gain media. Qualification then would be built into the design similar to complex optical systems, and the assembly and test would follow standard procedures for any flight system. The only remaining aspect unique to all the above lasers is the diode laser—either as the pumping source or as the complete transmitter. Hence we will focus on the past qualification procedure for diode lasers in this section. Even with that constraint, there is still no common plan available. As a point of reference, the qualification procedure for a representative number of systems above is discussed.

The TES (Tropospheric Emission Spectrometer) project is a technology demonstration for an interferometer test-bed. The laser is used as a stable frequency source and consists of a non-planar ring oscillator Nd: YAG crystal pumped by an 808-nm multimode diode laser. The reliability of the pump diodes was the key risk so 17 devices were placed in an accelerated 2500-hour life test. The failures were analyzed and traced to specific lots that were avoided for the final flight device. Other qualification tests on the diodes included an extended wafer burn-in, wire-bond pull, and die sheer tests. The complete laser system was then subject to vibration and thermal vacuum tests. The TES is flying on the Aura spacecraft, which was launched in July 2004.

Table 5-21. A partial list of lasers already flown in space.

Laser	Application	Mission/ Instrument	Qualification/ Developer	Key Parameters
Diode	Spectroscopy	Cassini/PIRLS	Commercial JPL	Mid-IR
Diode	Spectroscopy	Mars Polar Lander/DS-2	Commercial	1 μJ, 20 ns, 20 kHz, 890 nm
Diode	Spectroscopy	Mars Pathfinder	Commercial/ JPL	
Diode	Range finder	Rendezvous & Capture	Commercial	Multi-mode, CW
Nd: YAG	Altimetry	MOLA	McDonnell-Douglas	40 mJ, 10 Hz
Nd: YAG	Altimetry	Shuttle Laser Altimeter	MOLA spares	
Nd: YAG	Altimetry	Vegetation Canopy Laser	GSFC	10 mJ, 290 Hz, 5 ns
Nd: YAG	Altimetry	NEAR	McDonnell-Douglas	15 mJ, 12 ns, 8 Hz
Nd: YAG	Altimetry	Calipso	Fibertek	115 mJ, 27 Hz, 24 ns
Nd: YAG	Altimetry	ICESat/GLAS	GSFC	40 Hz
Nd: YAG	Altimetry	Clementine	LLNL	180 mJ, 1 Hz, 10 ns
Nd: YAG	Interferometry	TES	JPL/Lightwave Electronics	Single-longitudinal mode
Diode	Fiber optic	SRTM-Phase Calibrator	Commercial JPL	
Diode	Fiber optic	ISS Network Modules	Commercial	
Diode	Free-space communications	LCE in GEO orbit	Commercial/ NASDA	1 Mbps modulation
Diode	Free-space communications	STRV-II	Commercial (SDL)	1 Gbps modulation
Diode	Free-space communications	SILEX	Commercial (SDL)	50 Mbps modulation

DS-2 = Deep Space-2, GSFC = Goddard Space Flight Center, ICESat/GLAS = Ice Cloud Land Evaluation Satellite/Geoscience Laser Altimeter System, ISS = International Space Station, LCE = Laser Communications Equipment, LLNL = Lawrence Livermore National Laboratory, MOLA = Mars Orbiting Laser Altimeter, NEAR = Near Earth Asteroid Rendezvous, PIRLS = Probe IR Laser Spectrometer, SDL = Vendor, now JDS Uniphase, SILEX = Semiconductor Laser Experiment, SRTM = Shuttle Radar Topography Mission, STRV-II = Space Technology Research Vehicle II, TES = Tropospheric Emission Spectrometer

The diode laser pump bars in the Mars Orbiting Laser Altimeter (MOLA) laser were subjected to numerous electro-optic and screening tests throughout the fabrication process. The wafers were selected based on wavelength as a function of temperature for select devices to ensure a correct match to the Nd: YAG absorption band. After screening the bars visually for cracks, anomalies in metallization, stripe and coatings, the devices were processed from the selected wafers and tested electrically for threshold current, slope efficiency, linewidth, emission uniformity, power at high current and optically for pulse energy, boresight alignment, far-field, spot size, beam divergence, and pulse stability. The devices then underwent a burn-in for 44 hours and were retested with a further 22 hours of burn-in. The acceptance test for the devices was a maximum 10-percent degradation in threshold current, slope efficiency, and emission uniformity after the final burn-in. The MOLA laser transmitter successfully functioned for more than two billion pulses.

The qualification tests of the 10-W arrayed devices consisted of three-axis vibration tests (one sweep axis or one min/axis) with sine excitation corresponding to on-orbit operating conditions and random excitation corresponding to non-operating launch conditions. Optical tests were performed after each axis as well as optical power monitored during the operational test. A thermal vacuum test was then performed to ensure the devices operated correctly under vacuum, in particular the beam divergence was noted and the operating set points determined. The devices were not operated over the temperature extremes, four hours at $T_{\min.\max}$, but just their survivability was determined with three cycles. The only other tests were EMC and EMI tests to ensure the devices were not susceptible to power-line effects.

SILEX (Semiconductor Laser EXperiment) was deployed on a LEO Spot 4 and on a GEO Artemis satellite. The single-mode 850-nm diodes with output power of 100 mW were amplitude modulated around 1–40 Mbps. Commercial packages were baselined with a small sample pre-tested under vacuum with removable windows. A common lot of commercial devices was built and screened with some additional process monitoring. Preliminary environmental testing included MIL-STD-883 for the required shock, vibration, and temperature cycling. Reliability was based on life testing under vacuum up to 2000 hours at room temperature and other samples from three different epitaxial wafers operated at full power up to 3000 hours at 50 deg C [121]. No net degradation was noted. Although initially SILEX operated from a MEO, due to launch problems with the Artemis platform, it has now operated successfully with a GEO to LEO communication link.

In contrast to the above high reliability and thus significant cost programs, the Marshall Space Flight Center (MSFC) Autonomous Rendezvous and Capture experiment used multi-mode laser diodes from a commercial vendor as an illumination source. The devices were fiber coupled, and the vendor selection was based on the diode-to-fiber coupling scheme. A cylindrical lens

epoxied to the diode was deemed more reliable than a spherical ball lens under vibration. Apart from the fiber coupling, there was no individual pre-select of the devices. Several devices were vibration tested. and eight devices have successfully survived two Space Shuttle launches with no degradation. The packages were sealed with epoxy, and thus, they are not hermetic as the epoxy can bleed. Although this was cause for concern, no problem was encountered. The devices were vacuum and radiation tested to LEO type conditions with no problems. Care was taken to ensure the chamber was back filled with nitrogen during vacuum testing. The devices operated successfully on multiple Space Shuttle missions.

5.4.7.2 Design of Semiconductor Lasers for High Reliability Applications. In diode-based laser transmitter systems, the semiconductor diode can be either a low-power seed oscillator or a high-power pump diode used to pump a fiber amplifier or solid-state laser. A space-qualified design would require each step in the manufacture and packaging of the device to be compatible with the spacecraft environmental requirements. Although this is possible to undertake, there is not the commercial market to warrant large-scale production of such devices. However, there exist significant markets for low-cost devices that have a given lifetime in terrestrial application with the ability to replace the devices when the lifetime is exceeded. The difference in this case is primarily in the packaging and mounting of such a device, although rad tolerant does imply some alternate fabrication procedures may be advisable. The diode is grown by Molecular Beam Epitaxy (MBE) or Metal-Organic Chemical Vapor Deposition (MOCVD) layer by layer using, for example, alternating layers of GaAs and AlGaAs with varying Al concentration. There are various techniques for enhancing the reliability of the bare diode, and these techniques have been employed in the commercial devices. For instance, if a wavelength of 808 nm is required, then using a structure without Al in the active layers seems to prolong the device lifetime. Since Al oxidation is one degradation mechanism, avoiding Al in the region of the high intensity optical mode makes sense. Other designs have kept Al in the growth but have used passivated coatings on the facets of the device where the oxide growth would form. Hence, known mitigation strategies have been employed in the commercial devices to increase the lifetime. Once these devices are grown, cleaved, and metallized for bonding, they can be mounted to a submount to allow for heat transfer during operation. Commercial devices are typically not constrained by the large thermal ranges present in space environments and so a soft, or low melting point, indium solder is used to mount the bare diode to a copper or high thermally conductive mount. Due to this low melting point of around 150 deg C, the bond is susceptible to plastic shearing at temperatures approaching the melting point.

In space-based systems that are limited in their cooling budget due to available spacecraft DC power limitations, temperatures approaching this

100 deg C are not unforeseen. Indium is also known to creep from the submount joint up to the active laser region and cause catastrophic optical damage. To avoid these effects a hard solder such as gold/tin (Au/Sn) can be used that bonds the bare diode to a lattice-matched substrate. This process is significantly more complex since the device is now stressed, which can lead to stress birefringence in the optical mode of the semiconductor laser. Terrestrial fiber-based communication systems have used this technique in low power devices where the diode is mounted with the active region away from the mount. However, hard solder mounting of high-power devices at the wavelengths required for pumping solid-state lasers is not readily available.

The remainder of the pump diode package may include optics or fiber (to transmit the pump laser light) that are typically epoxied in place. Although the commercial packages can be hermetically sealed, the epoxies may not meet the out-gassing requirement for operation at elevated temperatures in a vacuum. Replacing the epoxies requires the packages to be reworked, which may not be an available option from companies that strive to meet high volume commercial markets.

Finally, none of the components, including the diode, in the commercial device are designed for high-radiation environments. Fortunately, this can be mitigated by shielding and will not significantly impact the small pump laser diodes packages. GaAs-based devices have shown a low susceptibility to radiation damage under moderate test conditions.

To design a pump laser diode to survive space qualification would then require hard soldering the semiconductor diode with the active side down to a lattice matched high thermally conductive submount, preferably in an hermetic package with no or low outgas epoxies and with sufficient mechanical robustness to ensure long lifetime. The commercial equivalent part can be upscreened by focusing on tests appropriate to the known degradation causes in the fabrication and packaging process, namely the mount and optical or fiber alignment.

5.4.7.3 Degradation Mechanisms. Laser systems for communication sources can be broken down into four main sections:

1) Semiconductor diode for optical pumping or oscillation
2) Fiber or solid state crystal for amplification
3) Optical components for the cavity and coupling to optical fiber
4) Electronics for driving the pump lasers or high-speed electronics to deliver the modulation

Here, we will focus on the degradation mechanisms that are unique to the laser, such as the semiconductor diode lasers and the solid-state gain media (whether in the form of fiber or as a bulk crystal).

Potential laser diode degradation mechanisms are:

- Mechanical: Die shear, wire bond fail, fiber pull—these mechanisms apply to the mechanical mounting of the die to the submount, the electrical connection to the metallized die via multiple wire bonds and the mounting of the optical fiber to the output of the diode laser.
- Metal electrode and solder stability: Soft or hard—a soft solder for the submount to the laser package can diffuse under moderate temperatures and pressures whereas a hard solder may produce instabilities in the mounting process that can stress the diode laser.
- Device dislocations and defects: these relate to non-uniformities in the material composition of the diode laser that can produce high current densities.
- Facet damage: oxidation or catastrophic optical damage (COD) can occur if the facet is not protected.
- Bandgap shrinking: nonlinear current densities near the facet can lead to distortion of the semiconductor bandgap, producing facet heating effects.
- Optical mode quality: in broad-area diodes, non-uniformities in the spatial optical modes can produce filaments that lead to local hot spots in the diode-laser gain region.
- Radiation damage: semiconductor materials are susceptible to displacement damage of ionizing radiation.

Fiber degradation mechanisms apply to passive fiber, where the fiber is just used to route the light, as well as active fiber, where the fiber is doped and acts as a gain media. Photo-darkening is the predominant degradation mechanism and arises from color centers formed from high-energy particles or gamma radiation. Basically, light is attenuated independent of wavelength, but the effect is reversible with high optical intensity able to bleach out the losses. This annealing effect is more effective while the laser is operating rather than when the fiber is cycled on and off. Radiation-induced damage has been extensively investigated in optical fibers to determine the optimum fiber composition that minimizes the induced damage [123]. Other mechanisms, such as stress fracturing of the fiber and outgassing of the jacket materials, have to be accounted for during qualification but will not be presented.

5.4.7.4 Qualification Process for Lasers. A general space-qualification or reliability-assurance procedure is now presented. As indicated earlier in the section on qualification of electronics and opto-electronics, 5.4.3.5, the NASA Electronic Parts and Packaging Program (NEPP) has formulated guidelines for the space qualification of opto-electronic and photonics devices. Here, we provide an overview of a qualification methodology from the fabrication process through product acceptance along with failure modes and test

descriptions. Figure 5-67 illustrates the qualification flow from the NEPP guidelines. However, it assumes the fabrication process can be customized for the mission requirements. Typically, for economic reasons this is not possible.

Reliability methodologies for fiber-optic components have also been detailed as applied to terrestrial telecommunications applications. The important distinction is that in a qualification program, the tests are well defined, and once the test criteria are met the devices pass. In a reliability program, failures are required to quantify the device reliability. The Telcordia documents (5.4.3.4, [104]) really satisfy the qualification aspect, and they have become the industry standard in the acceptance and testing of opto-electronic devices. For active components the Telcordia general reliability assurance requirements are detailed in GR-468-CORE, the fiber amplifier requirements are in GR-1312-CORE, and the passive optical component requirements are in GR-1221-CORE. Combining the NEPP guidelines with the Telcordia reliability assurance performance criteria and test procedures along with the above actually flown laser systems and their qualification processes allows us to develop a good space qualification plan for any diode-based laser system.

The first point to note is that, where possible, extensive use should be made of components developed and tested using Tecordia procedures. This addresses the device packaging principally. If such devices are not available, and assuming the devices have been commercially manufactured, the following summarizes a baseline approach.

Once the performance requirements have been determined, the suitability of the material composition with respect to radiation effects is tested. There may be design options to choose from that are more radiation tolerant. At the same time, an accelerated life test is performed on several samples to ensure that the

Lot Acceptance Test for Die
Die Mounting and Wire Bonding
Nondestructive Bond Pull Test
Pre-Cap Visual Inspection
Serialization and Marking
IR Scan
Seal
Temperature Cycle Test
Vibration
Particle Impact Noise Detection
Temperature/Electrical
DC Measurement
Burn-In
Hermetic Seal Test
Radiographic Inspection
Final Electrical
External Visual

Fig. 5-67. Qualification flow from NEPP guidelines.

design is compatible with the desired reliability. The life test should be at or above the performance level during nominal operation, but accelerated with higher thermal loads to reduce the testing time. Appropriate reliability models are used to translate the testing time to anticipated lifetime at lower temperatures. An example of such a model is the standard Arrhenius model where the lifetime is given by the mean time to failure from the exponential relationship:

$$T = T_o \exp - \frac{E_a}{kT}$$

Here E_a is the activation energy unique for each material system, and kT represents the thermal constant.

A destructive parts analysis (DPA) is also performed to characterize the integrity of the construction of the package. The tests listed in Fig. 5-68 are usually done on a sample basis so that accumulative effects are avoided. The test conditions are listed in MIL STD 883. If the device is fiber coupled, the test should be performed initially so that the device can be operated afterwards to check the degree of misalignment. The fine and gross leak tests, along with the residual gas analysis, are only applicable if the device is claimed to be hermetic. The results are documented. If any failures occur, either the part is excluded or waivers must be obtained from the project if the failure is deemed unrelated to those conditions expected during the mission.

Following the DPA, several representative device samples are chosen to undergo a battery of qualification tests as in Fig. 5-69. Again, there should be separate samples for each test to avoid any cumulative effects of the testing. A larger sample size is usually desired, such as 11 typically used to undergo Telcordia certification for laser modules. However, if the costs for testing and devices are prohibitive, then a sample size of 2–3 per test is sufficient. These devices should be randomly chosen from the same lot if possible to ensure that the results are representative of a particular batch process. If the flight devices come from many or unknown lots, then the same criteria should be used for the qualification testing.

The tests are derived from MIL-STD-883 and tailored to the opto-electronic design, such as those used in GR-CORE-468 for Telcordia certification. PIND or particle impact noise test is a short mechanical shock followed by an acoustic vibration to check for loose parts in a package. The thermal cycle test should cycle the temperature beyond the range that the device will experience in space and with an appropriate number of cycles to gain confidence that no cumulative degradation has occurred. Different thermal rates and number of cycles may be needed with a baseline of 50 cycles and a rate of 2 deg C/min. The vibration and constant acceleration tests should be performed separately on each axis. A sine test is sufficient for vibration testing the part since the

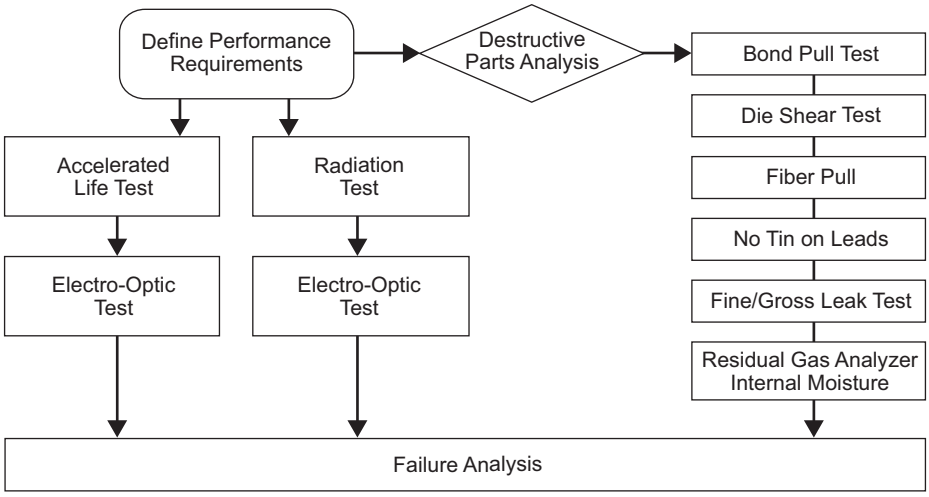

Fig. 5-68. Pre-screening destructive parts analysis.

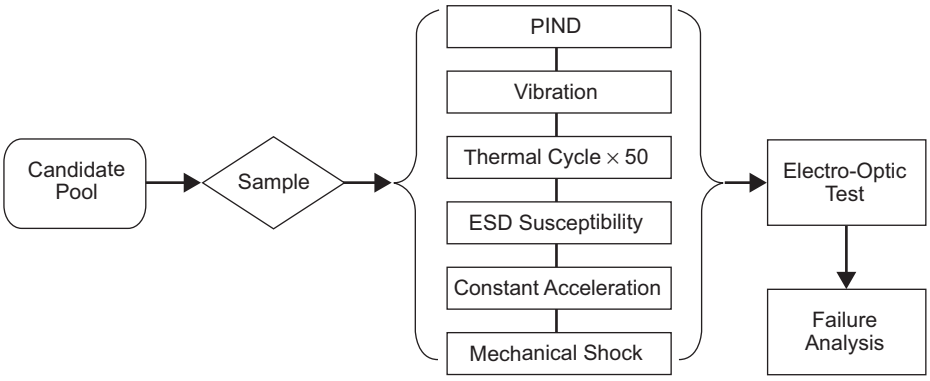

Fig. 5-69. A qualification flow chart example.

assembly usually undergoes a random vibration test at the next level. The electrostatic discharge (ESD) susceptibility test is fairly self-explanatory. All the tests are performed with the devices non-operational for qualification. However, it is important that the device be characterized after each test to measure the pertinent parameter critical to the device. For semiconductor laser diodes, these are typically the output power, wavelength, and perhaps mode quality in certain applications. If any failures are evident from testing, a complete failure analysis should be performed. Based on these findings, recommendations may be made to modify the environmental or performance requirements, reduce the lifetime, go to an alternate design, or continue with a higher level of risk.

The final testing flow shown in Fig. 5-70 provides the samples from which the flight units will be chosen. The candidate pool is the same from which the qualification samples were tested. Serialization basically gives the lot traceability of each device in case any anomalies are evident in the testing. The X-ray or C-SAM (C-mode scanning acoustic microscope) test should only be used if it is known that they will not degrade the device. These tests are used to check for voids and cracks in solder or bonds, to probe the chip attachment process, and to check the overall package integrity. A mini-accelerated burn in of the devices then occurs to mitigate any infant mortality that may be present. Although at elevated temperatures, the time scale needed is only several hours. Finally, a reduced set of thermal cycles, 8–10, is performed with the similar conditions as those used in the qualification testing. Following the 100-percent screening of the candidate pool, a flight device can be chosen along with backups as needed for engineering models, etc. Some results from an example space qualification of pump laser diodes are given in [124].

In summary, we have presented the approach to the qualification of lasers, in particular semiconductor lasers pertinent to a deep space optical communications system. This approach assembles the work of many projects in flying laser systems in space along with the experience of the

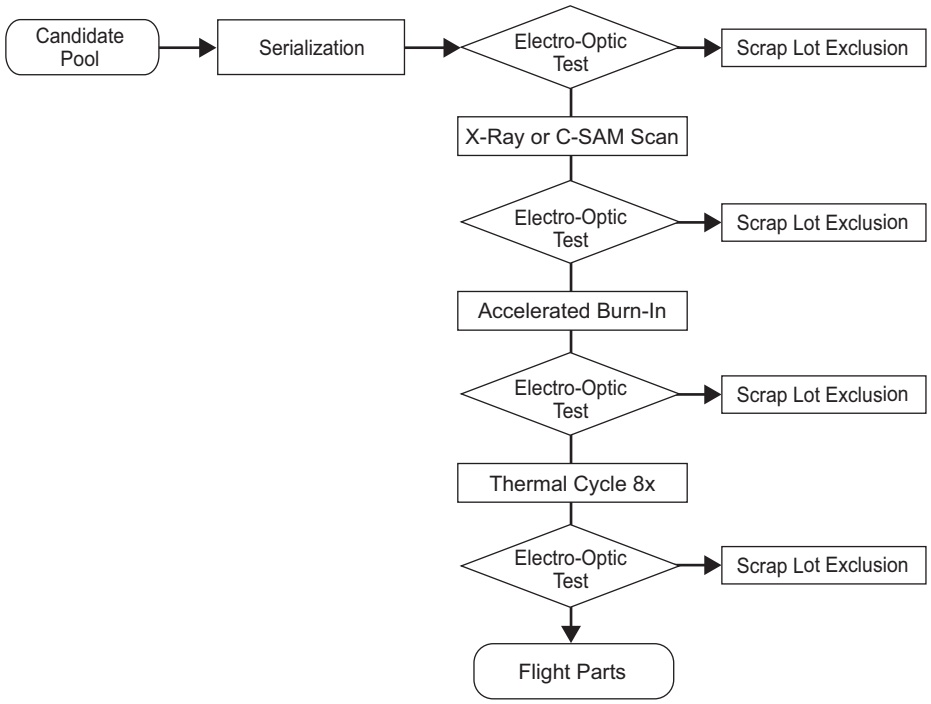

Fig. 5-70. Screening flow for flight units.

telecommunications industry in ensuring long-term reliability of lasers in terrestrial fiber-optic systems. Each project will have its own flavor, driven not only by the budget, but also by the class of mission as well. The qualification approach can thus be tailored accordingly. By highlighting the issues involved, it is hoped that a more robust qualification process can be followed, leading to a more reliable demonstration of the laser subsystem on any space borne applications.

5.4.8 Flight Qualification of Optics

Critical optical elements in an optical communication system are the front transmit and receive aperture (typically reflective), the aft optics (reflective or refractive), those in acquisition, the ATP subsystem, and the communication transmitter and receiver components. Many of these components have successfully flown in space following flight qualification through a rigorous testing procedure. The ATP subsystem's optics are built around a sensitive high-speed camera. Similar cameras are used in a variety of space flight imaging systems and will not be elaborated here.

Typical optical-system degradation mechanisms are known to be photo-darkening of the refractive optics with excessive radiation and misalignment due to lack of mechanical integrity in the mounting.

Qualification issues and cost drivers can be identified early in the mission design phase. For example, cost drivers might dictate use of selected commercial units wherever possible. The design of each unit within the optical system typically includes reliability engineering for vibration, shock, thermal/vacuum, EMC/EMI, outgassing, radiation, and safety [125–127]. Development of test plans and the actual performance of the environmental tests then follows.

To increase system reliability, the optical system development process may include development of different versions of the system: a Brassboard model, an Engineering model, and a Proto-flight model—each with an increasing degree of reliability. Definitions of various models vary from organization to organization. Roughly, a brassboard model includes flight qualifiable parts, without the need for use of qualified parts. The engineering model is a form, fit, and function system and uses partially qualified parts. The proto-flight model is the exact form, fit, and function and utilizes fully qualified parts only. The system as a whole then undergoes reliability testing.

References

[1] N. A. Page and H. Hemmati, "Preliminary Optomechanical Design for the X2000 Transceiver," *Proceedings of the SPIE,* vol. 3615, pp. 206–211, 1999.

[2] C. C. Chen and J. R. Lesh, "Overview of the Optical Communications Demonstrator," *Proceedings of the SPIE*, vol. 2123, pp. 85–94, 1994.

[3] N. A. Page, "Design of the Optical Communications Demonstrator Instrument Optical System," *Proceedings of the SPIE*, vol. 2123, pp. 498–504, 1994.

[4] H. Hemmati and J. R. Lesh "Laser Communication Terminals for the X2000 Series of Planetary Missions," *Proceedings of the SPIE*, vol. 3266, *Free-Space Laser Communication Technologies X*, G. Stephen Mecherle, editor, pp. 171–177, May 1998.

[5] P. R. Spyak and W. L Wolfe, "Scatter from Particulate-Contaminated Mirrors. Part 1: Theory and Experiment for Polystyrene Spheres and lambda = 0.328 μm," *Optical Engineering*, vol. 31, pp. 1746–1756, 1992.

[6] P. R. Spyak and W. L Wolfe, "Scatter from Particulate-Contaminated Minors. Part 2: Theory and Experiment for Dust and lambda = 0.8328 μm," *Optical Engineering*, vol. 31, pp. 1757–1763, 1992.

[7] P. R. Spyak and W. L. Wolfe, "Scatter from Particulate-Contaminated Mirrors. Part 3: Theory and Experiment for Dust and lambda = 10.6 μm," *Optical Engineering*, vol. 31, pp. 1764–1774, 1992.

[8] P. R. Spyak and W. L. Wolfe, "Scatter from Particulate-Contaminated Mirrors. Part 4: Properties of *S*catter from Dust for Visible to Far-Infrared Wavelengths," *Optical Engineering*, vol. 31, pp. 1775–1784, 1992.

[9] T. Weigel, "Stray Light Test Methods for Space Optical Components," *Proceedings of the SPIE*, vol. 2210, pp. 691–699, 1994.

[10] *Airborne Particulate Cleanliness Classes in Clean Rooms and Clean Zones*, available from General Services Administration (GSA) Regulation #FS-209E.

[11] *Product Cleanliness Levels and Contamination in Control Program*, MIL-STD 1246B, Sept. 4, 1987.

[12] H. Hemmati and N. Page, "Approaches for Efficient Coupling of Lasers to Telescopes with Secondary Mirror and Baffle Obscuration," *Proceedings of the SPIE*, vol. 4635, pp. 288–294, 2002.

[13] W. N. Peters and A. M Ledger, "Techniques for Matching Laser TEM00 Mode to Obstructed Circular Aperture," *Applied Optics*, vol. 9, pp. 1435–1442, 1970.

[14] B. J. Klein and J. J. Degnan, "Optical antenna gain—Transmitting antenna," *Applied Optics*, vol. 13, pp. 2134–2141, 1974.

[15] D. Vukobratovich, "Ultra-Lightweight Optics for Laser Communications," *Proceedings of the SPIE*, vol. 1218, pp. 178–192, 1990.

[16] R. Czichy, "Optical Design and Technologies for Space Instrumentation," *Proceedings of the SPIE*, vol. 2210, pp. 420–433, 1994.

[17] A. D. Pillsbury and J. A. Taylor, "Optomechanical Design of a Space-Based Diode Laser Transmitter Assembly," *Proceedings of the SPIE*, vol. 1044, *Optomechanical Design of Laser Transmitters and Receivers*, pp. 112–120, 1989.

[18] R. S. Bondurant, S. B. Alexander, V. W. S. Chan, A. A. Colao, J. E. Kaufmann, E. Lee, A. N. Madiwale, P. F. Martin, A. D. Pillsbury, E. A. Swanson, "An Opto-Mechanical Subsystem for Space-Based Coherent Optical Communications," *Proceedings of the SPIE*, vol. 996, *High Data Rate Atmospheric and Space Communications*, pp. 92–100, 1988.

[19] E. A. Swanson and R. S. Bondurant, "Using Fiber Optics to Simplify Free-Space Optical Communication Systems," *Proceedings of the SPIE*, vol. 1218, pp. 70–82, 1990.

[20] A. E. Seigman, *Lasers*, Chapter 26, "Laser Q Switching," University Science Books, Mill Valley, California, 1986.

[21] H. Hemmati and D. J. Copeland, "Laser Transmitter Assembly for Optical Communication Demonstrator," *Proceedings of the SPIE*, vol. 2123, pp. 283–291, 1994.

[22] R. B. Chesler, M. A. Karr, and J. E. Geusie, "An Experimental and Theoretical Study of High Repetition Rate Q-Switched Nd:YAG Lasers," *IEEE Journal of Quantum Electronics*, vol. 58, pp. 1899–1914, 1970.

[23] W. M. Grossman, M. Gifford, and R. W. Wallace, "Short-Pulse Q-Switched 1.3 and 1-micron Diode-Pumped Lasers," *Optics Letters*, vol. 15, pp. 622–624, 1990.

[24] A. Biswas, H. Hemmati, and J. R. Lesh, "High Data-Rate Laser Transmitters for Free-Space Laser Communications," *Proceedings of the SPIE*, vol. 3615, pp. 269–277, 1999.

[25] R. B. Chesler and S. Maydan, "Calculation of Nd:YAG Cavity Dumping," *Journal of Applied Physics*, vol. 43, pp. 1028–1030, 1971.

[26] L. Marshall, A. D. Hays, A. Katz, J. J. Kasinski, and R. L. Burnham, "High Power Pulsed and CW Diode-Pumped Mode-Locked Nd:YAG Laser," *OSA Proceedings on Advanced Solid-State Laser Conference*, vol. 10, Hilton Head, South Carolina, Optical Society of America, Washington, District of Columbia, pp. 240–246, March 18–20, 1991.

[27] M. Digonnet and C. J. Gaeta, "Theoretical Analysis of Optical Fiber Laser Amplifiers and Oscillators," *Applied Optics*, vol. 24, pp. 333–342, 1985.

[28] A. S. Kurkov, V. I. Karpov, A. Yu Laptev, O. I. Medvedkov, E. M. Dianov, A. N. Gur'yanov, S. A. Vasil'ev, V. M. Paramonov, V. N. Protopopov, A. A. Umnikov, N. I. Vechkanov, V. G. Artyushenko, and J. Frahm, "Highly Efficient Cladding-Pumped Fibre Laser Based on an Ytterbium-Doped Optical Fibre and a Fibre Bragg Grating," *Quantum Electronics*, vol. 29, no. 6, pp. 516–517, 1999.

[29] L. Goldberg, J. P. Koplow, and D. A. V. Kliner, "Highly Efficient 4 W Yb-Doped Fiber Amplifier Pumped by a Broad-Stripe Laser Diode," *Optics Lett*ers, vol. 24, pp. 673–680, 1999.

[30] C. C. Renaud, R. J. Selvas–Aguilar, J. Nilson, P. W. Turner, and A. B. Grudnin, "Compact High Energy Q-Switched Cladding Pumped Fiber Laser with a Tuning Range over 40 nm," *IEEE Photonics Technology Lett*ers, vol. 11, pp. 976–978, 1999.

[31] IPG Photonics Inc., web site, accessed July 11, 2005. (http://www.ipgphotonics.com/).

[32] P. A. Champert, S. V. Popov, and J. R. Taylor, "3.5 W Frequency-Doubled Fiber-Based Laser Sources at 772 nm," *Applied Physics Letter*s, vol. 78, pp. 2420–2421, April 13, 2001.

[33] P. A. Champert, S. V. Popov, M. A. Soladyankia, and J. R. Taylor, "Multiwatt Average Power Continua Generation in Holey Fibers Pumped by Kilowatt Peak Power Seeded Ytterbium Fiber Amplifier," *Applied Physics Letters*, vol. 81, pp. 2157–2159, September 16, 2002.

[34] Catalog of Mitsubishi Cable America, Inc., Ann Arbor, Michigan, 2003, web site accessed July 20, 2005. http://www.mcausa.com).

[35] W. Koechner, *Solid State Laser Engineering*, Springer Verlag, New York, 1994.

[36] W. K. Marshall, K. Cowles, and H. Hemmati; "Performance of Efficient Q-Switched Diode-Laser-Pumped Nd:YAG and Ho:YLF Lasers for Space Applications," *The Telecommunications and Data Acquisition Progress Report 42-95*, July–September, pp.168–173, November 1988. http://ipnpr.jpl.nasa.gov/progress_report/

[37] L. B. Soldano and E. C. M. Pennings, "Optical Multi-mode Interference Devices Based on Self-Imaging: Principles and Applications," *Journal of Lightwave Technology*, vol. 13, pp. 615–627, 1995.

[38] H. Nakano, S. Tsuji, S. Sasaki, K. Uomi, and K. Yamashita, "10 Gb/s, 4-Channel Wavelength Division Multiplexing Fiber Transmission Using Semiconductor Optical Amplifier Modules," *IEEE/OSA Journal of Lightwave Electronics*, vol. 11, no. 4, pp. 612–617, April 1993.

[39] C. C. Chen, D. Robinson, and H. Hemmati, "A 100 Mbps Resonant Cavity Phase Modulator for Coherent Optical Communications," *Proceedings of the SPIE*, vol. 1635, pp. 135–143, 1992.

[40] H. Hemmati, C. Esproles, and R. T. Menzies, "Frequency-Stabilized Diode-Pumped Tm, Ho:YLF Local Oscillator with ±4 GHz of Tuning Range," *Proceedings of the SPIE*, vol. 3380, pp. 75–79, 1998.

[41] J. A. Taylor, A. Pillsbury, M. F. Richardson, and D. Welford, "Diode Laser Transmitter for Space-Based Heterodyne Communication," *Proceedings of the SPIE*, vol. 996, pp. 77–83, 1988.

[42] K. Nielson (Hughes Aircraft), "Active Energy Control for Diode-Pumped Laser Systems Using Pulse-Width Modulation," Patent #5291505, 1994.

[43] H. Hemmati and J. R. Lesh, "A 3.5 W Output, Diode Pumped, Q-Switched 532 nm Laser," *Proceedings of the SPIE*, vol. 2123, pp. 264–269, 1994.

[44] H. Bruesselbach, D. S. Sumida, R. Reeder, and R. W. Byren, "Low-Heat, High-Power Scaling Using InGaAs Diode Pumped Yb: YAG Lasers," *IEEE Journal of Quantum Electronics*, vol. 3, pp. 105–116, 1997.

[45] V. V. Bezotosnyi, K .K. Kumykov, and N. V. Markov, "Ultimate Output Parameters of Laser Diode Bars and Arrays," *Quantum Electronics*, vol. 27, pp. 481–486, 1997.

[46] H. Hemmati, M. Wright, A. Biswas, and C. Esproles, "High Efficiency Pulsed Laser Transmitters for Deep-Space Communications," *Proceedings of the SPIE*, vol. 3932, pp. 188–195, 2000.

[47] D. R. Hjelme and A. R. Mickelson, "Theory of Timing Jitter in Actively Mode-Locked Lasers," *IEEE Journal of Quantum Electronics*, vol. 28, pp. 1594–1606, 1992.

[48] K. Shaik and H. Hemmati, "Wavelength Selection Criteria for Laser Communications," *Proceedings of the SPIE*, vol. 2381, pp. 342–357, 1995.

[49] *Baseline Design Document for Europa-Orbiter Mission: X2000 Optical Communication Subsystem*, JPL D-30264 (internal document), Jet Propulsion Laboratory, Pasadena, California, August 26, 1998.

[50] A. Biswas and S. Piazzolla, "Deep-Space Optical Communications Downlink Budget from Mars: System Parameters," *The Interplanetary Network Progress Report 42-154, April–June 2003*, Jet Propulsion Laboratory, Pasadena, California, pp. 1–38, August 15, 2003. http://ipnpr.jpl.nasa.gov/progress_report/

[51] D. M. Boroson, "Interplanetary Deep-Space Optical Communications Systems and Techniques," in *Special Symposium on High-Capacity Free-Space Laser Communications, 16th Annual Meeting of the IEEE Laser & Electro-Optics Society*, Tucson, Arizona, vol. 1, pp. 85–86, October 27–28, 2003.

[52] H. Hemmati and J. Hilland, *Mars Lasercomm Terminal Accommodation*, JPL D-32921 (internal document), Jet Propulsion Laboratory, Pasadena, California, July 2003.

[53] C.-C. Chen, "Effect of Earth Albedo Variation on the Performance of a Spatial Acquisition Subsystem Aboard a Planetary Spacecraft," *The Telecommunications and Data Acquisition Progress Report 42-95*, July–September 1988, Jet Propulsion Laboratory, Pasadena, California, pp. 202–211, November 15, 1988. http://ipnpr.jpl.nasa.gov/progress_report/

[54] J. W. Alexander, S. Lee, and C.-C. Chen, "Pointing and Tracking Concepts for Deep-Space Missions," *Proceedings of the SPIE*, vol. 3615, *Free-Space Laser Communication Technologies* XI, pp. 230–249, 1999.

[55] JPL mission and spacecraft library website, Jet Propulsion Laboratory, Pasadena, California, site accessed June 24, 2005. http://leonardo.jpl.nasa.gov/msl.

[56] JPL Optical Comm Group Acquisition Tracking Link Analysis Software website, Jet Propulsion Laboratory, Pasadena, California, site accessed June 23, 2005. http://ultratung.jpl.nasa.gov/group6/atlas/atlas.htm

[57] *Accelerometers, DSES Redmond: QA3000 Q-Flex® Accelerometer*, Honeywell web site accessed August 16, 2005. www.inertialsensor.com/qa3000.shtml

[58] J. J. Pearson, D. C. Hines, S. Golosman, and C. Kuglin, "Video-Rate Image Correlation Processor," *Proceedings of the SPIE*, vol. 119, *Application of Digital Image Processing, IOCC*, pp. 197–205, 1977.

[59] C. Kuglin and D. C. Hines, "The Phase Correlation Image Alignment Method," The Phase Correlation Image Alignment Method," *Proceedings of the International Conference on Cybernetics and Society*, pp. 163–165, September 1975.

[60] E. Castro and C. Morandi, "Registration of Translated and Rotated Images Using Finite Fourier Transform," *IEEE Transactions on Pattern Analysis and Machine Intelligence*, vol. PAMI-9, pp. 700–703, September 1987.

[61] T. Y. Yan, "Extended-Source Spatial Acquisition Process Based on Maximum- Likelihood Criterion for Planetary Optical Communications," *Proceedings of the SPIE*, vol. 1635, *Free-Space Laser Communication Technologies* IV, pp. 273–285, 1992.

[62] C.-C Chen, E. Hui, and G. Okamoto, "Confidence Range Estimate of Extended Source Imagery Acquisition Algorithms via Computer Simulations," *Proceedings of the SPIE*, vol. 1635, *Free-Space Laser Communication Technologies* IV, pp. 300–308, 1992.

[63] B. E Marino, Haiping Tsou, Tsun Yee Yan, "Earth Beacon Acquisition and Tracking Under Various Illumination Conditions," *Proceedings of the SPIE*, vol. 4272, *Free-Space Laser Communication Technologies* XIII, pp. 190–199, 2001.

[64] B. E Marino, H. Tsou, T. Y. Yan, "Use of Cross-Validation and Monte Carlo Simulation for Estimating the Parameters of Beaconless Free-Space Optical Pointing and Tracking," *Proceedings of the SPIE*, vol. 4635, *Free-Space Laser Communication Technologies XIV*, pp. 84–94, 2002.

[65] S. Lee, G. G. Ortiz, and J. W. Alexander, "High Accuracy and High Bandwidth Pointing Knowledge Using a Star Tracker-Based Acquisition, Tracking, and Pointing System," *The Interplanetary Network Progress Report 42–161*, Jet Propulsion Laboratory, Pasadena, California, pp. 1–18, May 15, 2005.

[66] S. Lee, G. G. Ortiz, W. T. Roberts, and J. W. Alexander, "Feasibility Study on Acquisition, Tracking, and Pointing Using Earth Thermal Images for Deep-Space Ka-Band and Optical Communications," *Interplanetary Network Progress Report 42-155, July–September 2003*, Jet Propulsion Laboratory, Pasadena, California, pp. 1–18, November 15, 2003. http://ipnpr.jpl.nasa.gov/progress_report/

[67] Mars Odyssey web site, Jet Propulsion Laboratory, Pasadena, California, accessed August 10, 2005.
http://mars.jpl.nasa.gov/odyssey/gallery/calibration

[68] W. L. Wolfe and G. J. Zissis, *The Infrared Handbook*, The Infrared Information Analysis Center (IRIA), Environmental Research Institute of Michigan, Ann Arbor, Michigan, pp. 3-52–3-55, 1993.

[69] D. Russell, H. Ansari, and C.-C. Chen, "Lasercom Acquisition and Tracking Control Using a CCD-based Tracker," *Proceedings of the SPIE*, vol. 2123, *Free-Space Laser Communication Technologies VI*, G. Stephen Mecherle, editor, pp. 294–303, 1994.

[70] R. B. Deadrick and W. F. Deckelman, "Laser Crosslink Subsystem—An Overview," *Proceedings of the SPIE*, vol. 1635, *Free Space Laser Communication Technologies IV*, pp. 225–235, 1992.

[71] *A Study to Define the Impact of Laser Communication Systems on Their Host Spacecraft, Hughes Aircraft Co., Final Report*, NASA-CR-175272, National Aeronautics and Space Administration, Washington, District of Columbia, April 1984.

[72] C. Chen and James Lesh, "Overview of the Optical Communications Demonstrator," *Proceedings of the SPIE*, vol. 2123, *Free-Space Laser Communication Technologies VI*, G. S. Mecherle, editor, pp. 85–95, 1994.

[73] M. Jeganathan, A. Portillo, C. Racho, S. Lee, D. Erickson, J. DePew, S. Monacos, and A. Biswas, "Lessons Learnt from the Optical Communications Demonstrator (OCD)," *Proceedings of the SPIE*, vol. 3615, *Free Space Laser Communication Technologies XI*, G. S. Mecherle, editor, pp. 23–30, 1999.

[74] A. Biswas, M. W. Wright, B. Sanii, N. A. Page, "45 km Horizontal Path Optical Link Demonstrations," *Proceedings of the SPIE*, vol. 4272, *Free-Space Laser Communication Technologies XIII*, G. S. Mecherle, editor, pp. 60–71, 2001.

[75] G. G. Ortiz, S. Lee, S. Monacos, M. Wright, and A. Biswas, "Design and Development of a Robust ATP Subsystem for the Altair UAV-to-Ground Lasercomm 2.5 Gbps Demonstration," *Proceedings of the SPIE*, vol. 4975, *Free-Space Laser Communication Technologies XV*, G. S. Mecherle, editor, pp. 103–114, July 2003.

[76] A. Biswas, N. Page, J. Neal, D. Zhu, M. Wright, G. G. Ortiz, W. H. Farr, H. Hemmati, "Airborne Optical Communications Demonstrator Design and Preflight Test Results," *Proceedings of the SPIE*, vol. 5712, *Free-Space Laser Communication Technologies XVII*, G. S. Mecherle, editor, pp. 205–216, 2005.

[77] S. Lee, "Pointing Accuracy Improvement Using Model-Based Noise Reduction Method," *Proceedings of the SPIE*, vol. 4635, *Free-Space Laser Communication Technologies XIV*, G. Stephen Mecherle, editor, pp. 65–71, 2002.

[78] C. Chen, J. W. Alexander, H. Hemmati, S. Monacos, T. Y. Yan, S. Lee, J. R. Lesh, and S. Zingales, "System Requirements for a Deep Space Optical Transceiver," *SPIE Proceedings*, vol. 3615, *Free Space Laser Communication Technologies XI*, G. Stephen Mecherle, editor, pp. 142–152, 1999.

[79] J. W. Alexander, S. Lee, and C.-C. Chen, "Pointing and Tracking Concepts for Deep-Space Missions," *Proceedings of the SPIE*, vol. 3615, *Free Space Laser Communication Technologies XI*, G. Stephen Mecherle, editor, pp. 230–249, 1999.

[80] R. E. Cummings, V. Gruev, and M. A. Ghani, "VLSI Implementation of Motion Centroid Localization for Autonomous Navigation," *Advances in Neural Information Processing Systems*, vol. 10, pp. 685–691, 1998.

[81] S. Kraemer, R. Downes, R. Katsanis, M. Crenshaw, M. McGrath, and R. Robinson, "STIS Target Acquisition," *HST Calibration Workshop*, Space Telescope Science Institute, Baltimore, Maryland, pp. 39–46, 1998.

[82] J. A. Cox, "Point-Source Location Using Hexagonal Detector Arrays," *Optical Engineering*, vol. 26, no. 1, pp. 69–74, 1987.

[83] J. A. Cox, "Advantages of Hexagonal Detectors and Variable Focus for Point-Source Sensors," *Optical Engineering*, vol. 28, no. 11, pp. 1145–1150, 1989.

[84] K. M. Iftekharuddin and M. A. Karim, "Acquisition by Staring Focal Plane Arrays: Pixel Geometry Effects," *Optical Engineering*, vol. 32, no. 11, pp. 2649–2656, 1993.

[85] I. E. Abdou, "Effect of Signal Truncation on Centroid Location Error Estimation," *Optical Engineering*, vol. 35, no. 4, 1221–1222, 1996.

[86] S. P. Monacos, R. K. Lam, A. A. Portillo, D. Q. Zhu, and G. G. Ortiz, "Design of an Event-Drive, Random-Access, Windowing CCD-Based Camera," *The Interplanetary Network Progress Report* 42–155, *July–September 2003*, Jet Propulsion Laboratory, Pasadena, California, pp. 1–24, November 15, 2003. http://ipnpr.jpl.nasa.gov/progress_report/

[87] *3-V 10-Bit 27 MSPS Area CCD Sensor Signal Processor, TLV987*, Texas Instruments, Dallas, Texas, September 1999.

[88] S. P. Monacos, A. A. Portillo, W. Liu, J. W. Alexander, and G. G. Ortiz, "A High Frame CCD Camera with Region-of-Interest Capability," *2001 IEEE Aerospace Conference Proceedings*, vol. 3, Big Sky, Montana, pp. 1513–1522, March 10–17, 2001.

[89] A. Talukder, J.-M Morookian, S. Monacos, R. Lam, and C. Labaw, A. Bond, "Fast Non-Invasive Eyetracking and Eye-Gaze Determination for Biomedical and Remote Monitoring Applications," *Proceedings of the SPIE*, vol. 5437, *Optical Pattern Recognition XV*, D. P. Casasent, T.-H. Chao, editors**,** pp. 179–190, April 2004.

[90] *680x500 Pixel CCD Image Sensor TC237*, Texas Instruments, Dallas, Texas, June 1996.

[91] G. G. Ortiz, A. Portillo, S. Lee, and J. Ceniceros, "Functional Demonstration of Accelerometer-Assisted Beacon Tracking," *Proceedings of the SPIE*, vol. 4272, *Free-Space Laser Communication Technologies XIII*, G. S. Mecherle, editor, pp. 112–117, 2001.

[92] S. Lee, G. G. Ortiz, W. Liu, and V. Garkanian, "Increasing Tracking Bandwidth for Deep-Space Optical Communications Using Linear Accelerometers," *The Interplanetary Network Progress Report* 42–155, *July–September 2003*, Jet Propulsion Laboratory, Pasadena, California, pp. 1–17, November 15, 2003. http://ipnpr.jpl.nasa.gov/progress_report/

[93] T. Tolker-Nielsen and G. Oppenhauser, "In-Orbit Result of an Operational Optical Intersatellite Link between ARTEMIS and SPOT4, SILEX," *Proceedings of the SPIE*, vol. 4635, *Free-Space Laser Communication Technologies XIV*, pp. 1–15, 2002.

[94] M. Kayton and W. R. Fried, *Avionics Navigation Systems*, John Wiley & Sons Inc., New York, New York, 1997.

[95] *The Hubble Space Telescope: Optical Assembly*, web site of Goddard Space Flight Center, Greenbelt, Maryland, site accessed, August 20, 2005. http://hubble.nasa.gov/technology/optics.php

[96] M. C. Algrain and J. Quin, "Accelerometer Based Line-of-Sight Stabilization Approach for Pointing and Tracking Systems," *Second IEEE Conference on Control Applications*, Vancouver, British Columbia, Canada, pp. 159–163, September 1993.

[97] H.-H. Chen, S.-C. Lee, and D. D. DeBra, "Gyroscope Free Strapdown Inertial Measurement Unit by Six Linear Accelerometers," *Journal of Guidance, Control, and Dynamics*, vol. 17, pp. 286–290, 1994.

[98] J. G. T. Ribeiro, J. T. P. Castro, and J. L. F. Freire, "Problems in Analogue Double Integration to Determine Displacements from Acceleration Data," *Proceedings of the 15th International Modal Analysis Conference*, Orlando, Florida, pp. 930–934, 1997.

[99] J. G. T. Ribeiro, J. L. F. Freire, and J. T. P. Castro, "Some Comments on Digital Integration to Measure Displacements Using Accelerometers," *Proceedings of the 17th International Modal Analysis Conference*, Orlando, Florida, pp. 554–559, 1999.

[100] J. M. Ceniceros, C. D. Jeppesen, and G. G. Ortiz, "Vibration Platform Testbed for Deep Space Acquisition, Tracking and Pointing," *Proceedings of the SPIE*, vol. 4272, *Free-Space Laser Communication Technologies XIII*, G. S. Mecherle, editor, pp. 209–218, 2001.

[101] M. Wittig, L. Van Holtz, D. El L. Tunbridge, and H. C. Vermeulen, "In-Orbit Measurements of Microaccelerations of ESA's Communications Satellite OLYMPUS," *Proceedings of the SPIE*, vol. 1218, *Free-Space Laser Communication Technologies II*, pp. 205–214, 1990.

[102] G. Ledebuhr, J. Kordas, I. Lewis, M. Richardson, G. Cameron, W. White, D. Dobie, W. Strubar, T. Tassinari, D. Sawyer, M. Shannon, L. Pleasance, A. Lieber, P. Trost, D. Doll, and M. Grote, "HiRes Camera and LIDAR Ranging System for the Clementine Mission," *Proceedings of the SPIE*, vol. 2472, pp. 62–81, 1995.

[103] *Semiconductor Devices, General Specification for*, MIL STD MIL-PRF-19500, Department of Defense, Columbus, Ohio, internet address checked February 8, 2005. www.dscc.dla.mil

[104] Telcordia Technologies, Inc., Piscataway, New Jersey, web site accessed July 20, 2005. www.telcordia.com

[105] NASA Electronic Parts and Packaging Program, www.nepp.nasa.gov, internet address checked February 8, 2005.

[106] C. Barnes, "The effects of radiation on Opto-Electronic Devices," *Proceedings of the SPIE*, vol. 721, pp. 18–34, 1986.

[107] G. C. Messenger and M. S. Ash, *The Effects of Radiation on Electronic System*s, Van Nostrand, New York, 1992.

[108] M. E. Fritz, "Photonics Space Experiment on-Orbit Results," *Proceedings of the SPIE*, vol. 2811, pp. 106–115, 1996.

[109] H. Lischka, H. Henschel, H. Kohn, O. Lennartz, W. Schmidt, "Radiation Effects in Light Emitting Diodes, Laser Diodes, Photodiodes and Optocouplers," *Proceedings of RADECS 93: Second European Conference on Radiation and its Effects on Components and Systems*, Fraunhofer INT, Euskirchen, Germany, pp. 226–231, 1993.

[110] A. H. Johnson, "Proton Displacement Damage in Light Emitting and Laser Doses," presented at *RADECS 2000* (Louvain-la-Neuve, Belgium), Fraunhofer INT, Euskirchen, Germany, September 2000.

[111] G. M. Williams, M. A. Putnam, and E. J. Fiebele, "Space Radiation Effects on Erbium-Doped Fibers," *Proceedings of the SPIE*, vol. 2811, pp. 30–37, 1996.

[112] H. Henschel, O. Koehn, and H. Schmidt, "Radiation-Induced Loss of Optical Fibers at 1300-nm and 1500-nm Wavelength," *Proceedings of the SPIE*, vol. 2811, pp. 68–76, 1996.

[113] H. Lischka, H. Henschel, O. Köhn, W. Lennartz, "Gamma and Neutron Irradiation of Optoelectronic Devices," *Proceedings of Radiation and Its Effects on Components and Systems, 1993, RADECS 93: Third European Conference on Radiation and its Effects on Components and Systems*, Fraunhofer INT, Euskirchen, Germany, pp. 560–563, 1995.

[114] J. Bogaerts, B. Dierickx, G. Meynants, and D. Uwaerts, "Total Dose and Displacement Damage Effects in a Radiation-Hardened CMOS APS," *IEEE Transactions on Electronic Devices*, vol. 50, pp. 84–90, January 2003.

[115] G. P. Summers, E. A. Burke, M. A. Xapsos, C. J. Dale, P. W. Marshall, and E. L. Petersen, "Displacement Damage in GaAs Structures," *IEEE Transactions on Nuclear Science*, vol. 35, no. 6, pp. 1221–1226, December 1988.

[116] B. H. Rose and C. E. Barnes, "Proton Damage Effects on Light Emitting Diodes," *Journal of Applied Physics*, vol. 53, pp. 1772–1780, 1982.

[117] H. Rose, M. S. Hopkins, and R.A. Fields, "Characterization and Control of Gamma and Proton Radiation Effects on the Performance of Nd: YAG and Nd: YLF Lasers," *IEEE Journal of Quantum Electronics*, vol. 31, pp. 1593–1602, 1995.

[118] Sira Electro-Optics Limited, South Hill Chislehurst, England, internet address checked February 8, 2005.
http://reat.space.qinetiq.com/Reat/reat_dev/REAT_245tn2_draft.pdf

[119] G. L. Jacobs *Evaluation of Fiber Optic Emitters and Detectors*, Document 08-012**,** Goddard Space Flight Center, Greenbelt, Maryland, May 16, 1986.

[120] C. R. Webster, S. P. Sander, R. Beer, R. D. May, R. A. Knollenberg, D. M. Hunter, and J. Ballard, "Tunable Diode Laser IR Spectrometer for in-situ Measurements of the Gas Phase Composition and Particle Size Distribution of Titan's Atmosphere," *Applied Optics*, vol. 29, pp. 907–917, 1990.

[121] R. Craig, B. Li, and B. Chan, "Laser Qualification for the SILEX Program," *Proceedings of the SPIE*, vol. 2123, pp. 238–242, 1994.

[122] A. S. El-Dinary, T. D. Cole, M. T. Boies, R. A. Reitner, and D. Rodriguez, "Testing and Space Qualification of the NEAR Laser Rangefinder," *Proceedings of the SPIE*, vol. 2748, pp. 140–150, 1996.

[123] D. R. Maack, "Reliability Methodology for Fiber Optic Components," *Optics and Photonics News*, vol. 13, no. 5, pp. 34–39, May 2002.

[124] M. W. Wright, D. Franzen, H. Hemmati, H. Becker, M. Sandor, "Qualification and Reliability Testing of Commercial High-Power Fiber-Coupled Semiconductor Lasers for Space Applications," *Optical Engineering*, vol. 44, no. 5, Paper 054204, 2005.

[125] R. H. Czichy, "Optical Design and Technologies for Space Instrumentation," *Proceedings of the SPIE*, vol. 2210, pp. 420–433, 1994.

[126] D.-R. Schmitt, "Degradation Effects of Optical Components in the Low Orbit," *Proceedings of the SPIE*, vol. 2210, pp. 449–465, 1994.

[127] M. I. Anapol, "Silicon Carbide Lightweight Telescopes for Advanced Space Application," *Proceedings of the SPIE*, vol. 2210, pp. 373–382, 1994.